

NASA Contractor Report 195285

1N-07

300

p. 111

# Prediction of Unsteady Flows in Turbomachinery Using the Linearized Euler Equations on Deforming Grids

William S. Clark and Kenneth C. Hall  
*Duke University*  
*Durham, North Carolina*

March 1994

Prepared for  
Lewis Research Center  
Under Grant NAG3-1192



National Aeronautics and  
Space Administration

(NASA-CR-195285) PREDICTION OF  
UNDSTEADY FLOWS IN TURBOMACHINERY  
USING THE LINEARIZED EULER  
EQUATIONS ON DEFORMING GRIDS Final  
Report (Duke Univ.) 111 p

N94-27654

Unclass

G3/07 0000300

**PREDICTION OF UNSTEADY FLOWS IN  
TURBOMACHINERY USING THE LINEARIZED  
EULER EQUATIONS ON DEFORMING GRIDS**

A Final Technical Report on Research Conducted Under  
NASA Grant NAG3-1192 by

William S. Clark  
Graduate Research Assistant

and

Kenneth C. Hall  
Assistant Professor and Principal Investigator

Department of Mechanical Engineering and Materials Science  
School of Engineering  
Duke University, Durham, NC 27708

Submitted to:

NASA Lewis Research Center  
April, 1993

## Abstract

A linearized Euler solver for calculating unsteady flows in turbomachinery blade rows due to both incident gusts and blade motion is presented. The model accounts for blade loading, blade geometry, shock motion, and wake motion. Assuming that the unsteadiness in the flow is small relative to the nonlinear mean solution, the unsteady Euler equations can be linearized about the mean flow. This yields a set of linear variable coefficient equations that describe the small amplitude harmonic motion of the fluid. These linear equations are then discretized on a computational grid and solved using standard numerical techniques. For transonic flows, however, one must use a linear discretization which is a conservative linearization of the nonlinear discretized Euler equations to ensure that shock impulse loads are accurately captured. Other important features of this analysis include a continuously deforming grid which eliminates extrapolation errors and hence, increases accuracy, and a new numerically exact, nonreflecting far-field boundary condition treatment based on an eigenanalysis of the discretized equations. Computational results are presented which demonstrate the computational accuracy and efficiency of the method and demonstrate the effectiveness of the deforming grid, far-field nonreflecting boundary conditions, and shock capturing techniques. A comparison of the present unsteady flow predictions to other numerical, semi-analytical, and experimental methods shows excellent agreement. In addition, the linearized Euler method presented requires one to two orders-of-magnitude less computational time than traditional time-marching techniques making the present method a viable design tool for aeroelastic analyses.

# Contents

<b>1</b>	<b>Introduction</b>	<b>6</b>
1.1	Historical Development . . . . .	6
1.2	Overview of Strategy Employed . . . . .	9
1.3	Outline . . . . .	11
<b>2</b>	<b>Governing Equations</b>	<b>12</b>
2.1	The Nonlinear Euler Equations . . . . .	12
2.1.1	Continuity Equation . . . . .	13
2.1.2	Momentum Equation . . . . .	13
2.1.3	Energy Equation . . . . .	14
2.1.4	Summary . . . . .	14
2.2	Linearization Of The Euler Equations . . . . .	14
2.2.1	Computational Coordinate System . . . . .	15
2.2.2	Flow Decomposition . . . . .	15
2.3	Linearized Euler Equations In Computational Domain . . . . .	17
2.4	Near-Field Boundary Conditions . . . . .	21
2.4.1	Solid Surface . . . . .	21
2.4.2	Periodicity . . . . .	23
2.5	Summary . . . . .	23
<b>3</b>	<b>Basic Numerical Integration Scheme</b>	<b>25</b>
3.1	Unsteady Grid Generation . . . . .	25
3.2	Basic Lax-Wendroff Integration Scheme (One-Dimensional Model) . .	27
3.3	Basic Lax-Wendroff Integration Scheme (Two-Dimensional Euler Equations) . . . . .	30
3.4	Smoothing . . . . .	33
3.5	Properties of Ni's Scheme . . . . .	34
3.5.1	Accuracy and Consistency . . . . .	34
3.5.2	Stability . . . . .	36
3.5.3	Conservation . . . . .	40
3.6	Multiple-Grid Accelerator . . . . .	41
3.7	Summary . . . . .	44

<b>4</b>	<b>Far-Field Boundary Conditions</b>	<b>45</b>
4.1	Introduction . . . . .	45
4.2	Characteristics Of The Linearized Equations . . . . .	46
4.2.1	One-Dimensional Characteristics . . . . .	46
4.2.2	Two-Dimensional Characteristics . . . . .	48
4.2.3	Exact Numerical Characteristics . . . . .	50
4.3	Application of Far-Field Boundary Conditions . . . . .	55
4.3.1	One-Dimensional Nonreflecting Boundary Conditions . . . . .	55
4.3.2	Two-Dimensional Nonreflecting Boundary Conditions . . . . .	56
4.3.3	Numerically Exact Nonreflecting Boundary Conditions . . . . .	57
4.4	Summary . . . . .	57
<b>5</b>	<b>Results</b>	<b>59</b>
5.1	Flat Plate . . . . .	59
5.2	Tenth Standard Configuration . . . . .	62
5.3	First Standard Configuration . . . . .	69
5.4	Summary . . . . .	72
<b>6</b>	<b>Transonic Theory</b>	<b>76</b>
6.1	Introduction . . . . .	76
6.2	Theory . . . . .	77
6.2.1	Flow Field Description . . . . .	77
6.2.2	Numerical Modelling of the Shock Impulse . . . . .	78
6.2.3	Method I and Method II Linearizations . . . . .	81
6.2.4	Test for Linearized Conservation . . . . .	86
6.3	Results . . . . .	86
6.3.1	Transonic Channel Flow . . . . .	86
6.3.2	Unsteady Compressor and Fan Flows . . . . .	92
6.4	Summary . . . . .	100
<b>7</b>	<b>Conclusions And Future Considerations</b>	<b>101</b>
7.1	Conclusions . . . . .	101
7.2	Future Considerations . . . . .	102

# List of Figures

1.1	Geometry of a rectilinear cascade . . . . .	9
2.1	Typical control volume . . . . .	13
2.2	Left: Unsteady grid in computational coordinate system $(\xi, \eta)$ . Right: Unsteady grid in physical coordinate system $(x, y)$ for the case of a cascade of airfoils pitching about their midchords with an interblade phase angle, $\sigma$ , of $90^\circ$ . Flow calculations are performed using a single blade passage. Multiple passages are shown for clarity. . . . .	16
2.3	Classification of boundary types in computational domain . . . . .	21
2.4	Illustration of position vectors for flow tangency boundary condition . . . . .	22
2.5	Illustration of the periodic boundary condition . . . . .	24
3.1	Typical computational cell for one-dimensional Ni scheme . . . . .	28
3.2	Nomenclature used in the description of the computational cells . . . . .	31
3.3	Von-Neumann stability analysis, one-dimensional model equation: $k = 0.0, \lambda = 0.6, 0.8, 1.0, 1.2$ . . . . .	38
3.4	Von-Neumann stability analysis, one-dimensional model equation: $k = 1.0, \lambda = 0.6, 0.8, 1.0, 1.2$ . . . . .	38
3.5	Eigenvalue analysis of one-dimensional model equation: $k = 0.0, \lambda = 0.6, 0.8, 1.0, 1.2$ (periodic boundaries) . . . . .	40
3.6	Eigenvalue analysis of one-dimensional model equation: $k = 1.0, \lambda = 0.6, 0.8, 1.0, 1.2$ (periodic boundaries) . . . . .	41
3.7	Eigenvalue analysis of one-dimensional model equation: $k = 0.025, 0.05, 0.1, \lambda = 0.8$ (nonreflecting boundaries) . . . . .	42
3.8	Perspective view of multiple grid acceleration levels . . . . .	43
4.1	Eigenvalues of upstream far-field modes of discretized equations . . . . .	53
4.2	Analytically computed eigenvalues of far-field modes . . . . .	54
5.1	Unsteady pressure difference for flat plate cascade subjected to an incident vortical gust: $k = 2.221, \sigma = -180^\circ$ . . . . .	61
5.2	Unsteady pressure difference for flat plate cascade undergoing an unsteady plunging motion: $k = 2.221, \sigma = -180^\circ$ . . . . .	61
5.3	Unsteady pressure difference for flat plate cascade subjected to an incident vortical gust: $k = 3.332, \sigma = 270^\circ$ . . . . .	62
5.4	Steady coefficient of pressure distribution, Tenth Standard Configuration: $M_\infty = 0.7, G = 1.0, \Theta_\infty = 45^\circ, \Omega_\infty = 55^\circ$ . . . . .	63

5.5	(top) Real unsteady pressure distribution for cascade of Tenth Standard Configuration airfoils subjected to an inlet vortical gust; (bottom) Imaginary unsteady pressure distribution for cascade of Tenth Standard Configuration airfoils subjected to an inlet vortical gust: $k = 1.287$ , $\sigma = -90^\circ$ . . . . .	65
5.6	(top) Real unsteady pressure distribution for cascade of Tenth Standard Configuration airfoils undergoing an unsteady plunging motion; (bottom) Imaginary unsteady pressure distribution for cascade of Tenth Standard Configuration airfoils undergoing an unsteady plunging motion: $k = 1.287$ , $\sigma = -90^\circ$ . . . . .	66
5.7	(top) Real unsteady pressure distribution for cascade of Tenth Standard Configuration airfoils undergoing an unsteady plunging motion; (bottom) Imaginary unsteady pressure distribution for cascade of Tenth Standard Configuration airfoils undergoing an unsteady plunging motion: $k = 2.573$ , $\sigma = -180^\circ$ . . . . .	67
5.8	Unsteady pressure contours for cascade of Tenth Standard Configuration airfoils undergoing an unsteady plunging motion: $k = 2.573$ , $\sigma = -180^\circ$ . . . . .	68
5.9	(top) Real unsteady pressure distribution for cascade of Tenth Standard Configuration airfoils undergoing an unsteady plunging motion; (bottom) Imaginary unsteady pressure distribution for cascade of Tenth Standard Configuration airfoils undergoing an unsteady plunging motion: $k = 2.573$ , $\sigma = -180^\circ$ . . . . .	70
5.10	Convergence histories for cascade of Tenth Standard Configuration airfoils undergoing an unsteady plunging motion: $k = 2.573$ , $\sigma = -180^\circ$ . . . . .	71
5.11	Imaginary part of unsteady pitching moment for cascade of Tenth Standard Configuration airfoils undergoing an unsteady pitching motion: $k = 0.5$ . . . . .	72
5.12	Steady coefficient of pressure distribution, First Standard Configuration: $M_\infty = 0.17$ , $G = 0.75$ , $\Theta_\infty = 55^\circ$ , $\Omega_\infty = 66^\circ$ . . . . .	73
5.13	(top) Real unsteady pressure distribution for cascade of First Standard Configuration airfoils undergoing an unsteady pitching motion; (bottom) Imaginary unsteady pressure distribution for cascade of First Standard Configuration airfoils undergoing an unsteady pitching motion: (case 8) $k = 0.244$ , $\sigma = -90^\circ$ . . . . .	74
6.1	Top to bottom: (a) Trajectory of shock in a channel or on airfoil surface; (b) Mean and unsteady flow distribution; (c) Perturbation flow showing shock impulse; (d) same as (c) with impulse modelled by shock capturing. Note the area under the impulse is the same in (c) and (d).	82
6.2	Steady transonic flow in a diverging channel . . . . .	87
6.3	Top: Perturbation pressure in a diverging channel due to a steady perturbation in back pressure. Bottom: Enhancement of the shock impulse region. . . . .	89

6.4	Top: Unsteady pressure in a diverging channel due to an unsteady perturbation in back pressure, $\omega = 1.0$ . Bottom: Enhancement of the shock impulse region. . . . .	90
6.5	Coefficient of pressure distribution, Tenth Standard Configuration: $M_\infty = 0.8, G = 1.0, \Theta = 45^\circ, \Omega_\infty = 58^\circ$ . . . . .	93
6.6	Real and imaginary unsteady surface pressure, Tenth Standard Configuration, plunging: $\omega = 1.287, \sigma = -90^\circ$ . . . . .	94
6.7	Convergence histories of unsteady solution for different methods. All cases use multigrid acceleration. . . . .	95
6.8	Steady pressure contours, modified circular arc airfoil: $M_\infty = 1.2, G = 1.0, \Theta = 55^\circ, \Omega_\infty = 60^\circ$ . . . . .	96
6.9	Isentropic Mach number distribution, modified circular arc airfoil: $M_\infty = 1.2, G = 1.0, \Theta = 55^\circ, \Omega_\infty = 60^\circ$ . . . . .	97
6.10	Imaginary part of moment coefficient for a range of interblade phase angles, modified circular arc airfoil, pitching about midchord, $\omega = 0.5$ . . . . .	98
6.11	Real and imaginary unsteady surface pressure, modified circular arc airfoil, pitching about midchord: $\omega = 0.5, \sigma = 120^\circ$ . . . . .	99

# Chapter 1

## Introduction

In order to understand unsteady aerodynamic phenomena in turbomachinery, aeroelasticians require accurate and efficient models of the unsteady flow fields that result from blade motion and incident gusts. This is a formidable task since the flow is time-dependent, three-dimensional, compressible, and in general viscous. The objective of this research is to develop a computational algorithm, based on the linearized Euler equations, that will accurately and efficiently predict unsteady subsonic and transonic flows in cascades. Specifically, the goal of the present research is to develop an algorithm which requires about the same amount of computer time to solve a single unsteady flow problem as is required to solve the equivalent steady flow problem, and which computes the unsteady flow field about as accurately as its steady flow counterpart.

In the present study, particular emphasis is placed on the modeling of the resultant forces associated with unsteady shock motions encountered in transonic flows. It is important to model accurately these shock loads since the unsteady blade loading associated with the moving shock often accounts for about half of the total unsteady load.

Another concern is the effective handling of the far-field computational boundaries. Because the computational domain must be finite in extent, so-called far-field boundary conditions must be imposed on the far-field boundaries. If not properly formulated, however, these boundary conditions can reflect unsteady disturbances back into the computational domain, corrupting the solution. This can lead to incorrect predictions of the unsteady surface loading and hence incorrect conclusions as to the stability or response of the airfoil. In this report, a new exact far-field boundary condition formulation is presented. The method has the advantage that it is generic, and can be applied to a wide range of flow models (potential equation, Euler equations, Navier-Stokes equations) and can be extended to fully three dimensional analyses.

### 1.1 Historical Development

The techniques which have been developed over the last 30 years to analyze unsteady flows in cascades can be classified into one of the following categories: analytical and

semi-analytical methods or field methods. Using analytical approaches, the governing equations are solved exactly or through the use of point singularities. The complexity of the analytical problem requires simplifying assumptions which make the problem tractable. These assumptions, e.g., thin airfoils, no camber and light loading, severely limit the applicability of these methods since these assumptions are violated by most fan, compressor and turbine blades.

One of the first classical analyses of unsteady flows in turbomachinery was developed by Whitehead [52], who considered two-dimensional, incompressible flow through a cascade of flat plate airfoils. Since the steady flow was assumed to be uniform, there could be no accounting for the steady loading on the blade. Whitehead later extended his model to include the effects of steady loading and showed that steady loading plays an important role in bending flutter [53]. Later, Atassi and Akai [3] developed an inviscid incompressible flow model which included the effects of camber, thickness, and steady blade loading. With this model they studied steady and unsteady incompressible flows through a cascade of thick, cambered airfoils. Their results, like Whitehead's, showed the importance of steady blade loading on the unsteady flow in the cascade.

The effects of compressibility were next investigated by Whitehead [54] and Smith [43]. With compressibility, the added complexity of acoustic modes and acoustic resonance is introduced. Smith found that for unloaded cascades, the theory was successful in predicting the cut-off behavior as well as the amplitude of the acoustic waves. For steadily loaded cascades, however, the amplitudes of the acoustic waves were not predicted well.

Several researchers [1,20,47] have investigated cascades of vibrating flat plates in supersonic flow which is axially subsonic. The results obtained using these models indicate that bending flutter will not occur at the reduced frequencies and Mach numbers at which real compressors actually exhibit bending flutter. Bendiksen [7] later used a perturbation analysis to include effects due to steady loading, thickness, camber and shock motion and demonstrated the important role of shock motion in flutter prediction.

Although the assumptions invoked by these analytical and semi-analytical methods limit analyses to low cambered and lightly loaded airfoils, significant insight was gained through the use of these elegant, albeit simplified, models. Specifically, to model accurately the flow in a cascade, the effects of steady blade loading are critical. This means an effective model must contain the effects of camber and thickness, as well as any discontinuities the flow field may permit, i.e. shocks. The evolution of computer capabilities, coupled with the cost and difficulty in experimentally evaluating the unsteady aerodynamic performance of turbomachinery blade rows, has provided an impetus for the development of increasingly more sophisticated field models which capture more of the underlying physics of the problem such as arbitrary blade geometries and complicated shock structures. These models, classified as field methods, can be further separated into two groups, time marching and linearized methods (sometimes called time linearized).

The most direct approach taken has been to develop time-accurate time-marching Euler [14,18,28,31] and Navier-Stokes [5,17,40,41] solvers capable of analyzing the

unsteady flows found in turbomachinery. This approach has merit in that the numerical implementation is relatively straightforward and complicated two- and three-dimensional nonlinear flows can be analyzed. There is a cost associated with this approach, however. Because of the large number of grid points and the requirement that the analyses be both accurate and stable, the maximum allowable time step used in the calculations must be small making these calculations prohibitively expensive for routine design use.

In a linearized analysis, the flow is assumed to be composed of a nonlinear mean (or steady) flow plus an unsteady, harmonically varying small perturbation flow. Since the resulting unsteady flow field can be described by linear, variable coefficient, differential equations in which the explicit time dependence has been removed (that is the equations are solved in the frequency domain), the solution of the equations requires significantly less computational effort than that of the full nonlinear unsteady flow equations. Verdon et al. [47,48,49] and Whitehead and Grant [56] pioneered the development of linearized potential solvers as applied to the subsonic blade motion problem (the flutter or aerodynamic damping problem). Later, Hall and Verdon [26] and Caruthers and Dalton [11] extended this technique to handle incident vortical and entropic gusts using the flow decomposition technique of Atassi and Grzedzinski [4]. However, because of the inherent assumption that the steady flow be irrotational and isentropic, potential analyses are applicable only in the subsonic and low transonic flow regimes. In addition, three-dimensional flows with inlet swirl, typical of those found in turbomachinery applications, cannot be modeled using potential techniques.

To overcome some of the limitations of the potential methods, investigators have begun to develop linearized Euler techniques. Ni and Sisto [39] proposed a technique whereby the linearized harmonic Euler equations were solved using traditional time-marching techniques by introducing a pseudo-time dependence. In this work, the flow was assumed to be isentropic and the results were limited to flat plate cascades. Hall and Crawley [24] later developed a direct method of solving the linearized Euler equations for realistic compressor designs, as well as for transonic channel flows. For transonic flows, they used shock fitting to model the motion of the shock. Although shock fitting does provide sharp, clearly defined shocks and shock motions, it is cumbersome and complex and therefore less desirable than shock capturing. In a recent paper, Lindquist and Giles [35] outlined the conditions under which shock capturing correctly models shock motion in a linearized Euler analysis. The linearized Euler technique has shown the potential for dramatically reducing the computational cost required to solve unsteady subsonic [22,25] and transonic [23] flow problems in both two and three dimensions while still modeling the dominant physics of the unsteady flow problem. However, the method is still somewhat immature, and a number of modeling and computational issues require further research to make the method a viable technique.

## 1.2 Overview of Strategy Employed

A linear cascade is an array of blades similar to a blade row in a turbomachine, except that it is usually two-dimensional, as shown by Fig. 1.1. Calculations from two-dimensional cascades can be directly useful for rotating machines, provided that the hub- to-tip ratio is nearly unity, though corrections are often made for radial effects. The variables which define the cascade geometry are the blade shape, solidity (the ratio of chord-to-gap) and stagger angle (see Fig. 1.1). In the absence of unsteady excitation, the blades are identical in shape, equally spaced and their chord lines are oriented at the same stagger angle relative to the axial flow direction.

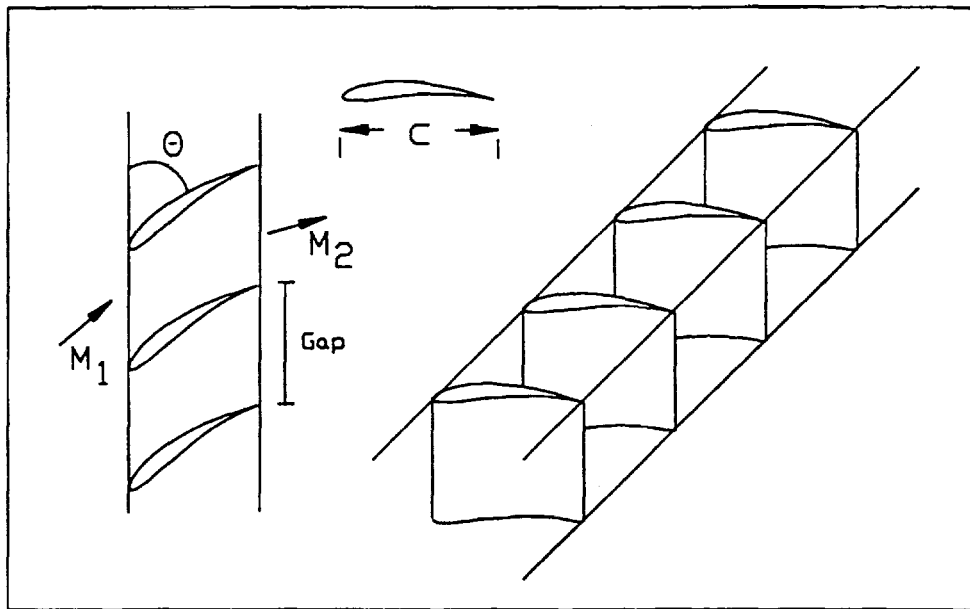


Figure 1.1: Geometry of a rectilinear cascade

Although viscous forces produce the wakes which are a prime source of forced response in turbomachinery, inviscid effects dominate the resulting wake interaction with a downstream blade row, subject to the limiting assumptions that the flow remains attached and that the boundary layers are thin. In the present analysis, therefore, the fluid flow through a single cascade of airfoils is modeled as two-dimensional, adiabatic, and inviscid. Subject to these constraints, the governing equations of the fluid motion are the two-dimensional Euler equations. These equations are nonlinear and unsteady and thus generally difficult to solve efficiently.

To simplify the solution process, the present method makes use of the fact that for small disturbances, such as are typically found in turbomachine applications, the unsteady perturbation flow is small compared with the mean flow and can reasonably be linearized about the mean flow. The resulting equations are linear, variable coefficient, differential equations. By introducing a pseudo time dependence into these equations, the equations may be solved by time marching them to steady state. Since

the equations need not be marched time accurately, acceleration techniques such as multiple-grid acceleration and local time stepping may be employed. As previously indicated, along with efficiency, accuracy of the solution is important.

The present analysis uses two procedures developed to improve the accuracy of the method. First is the implementation of a continuously deforming grid. While several nonlinear time-marching Euler codes have been developed that use moving or deforming computational grids [6,8,42,46], most previous linearized potential and Euler solvers have used computational grids fixed in space for solution of the linearized equations [24,48,49,50]. To calculate the flutter stability of an airfoil, one assumes the blades vibrate with a fixed amplitude, frequency, and interblade phase angle. The linearized equations are then solved to determine the unsteady pressure on the airfoil surface. However, since the blades move through the stationary grid, the boundary conditions that apply at the instantaneous location of the airfoil must be extrapolated back to the mean location of the airfoil where the boundary conditions are actually applied. Similarly, once the unsteady flow solution has been found on the fixed grid, terms involving the mean flow pressure gradient must be added to the unsteady pressure at the mean blade location to obtain the unsteady pressure at the instantaneous position of the blade. These gradient terms are difficult to evaluate accurately in practice, especially near the leading and trailing edges of fan and compressor blades. The resulting errors introduced at the airfoil boundary make the computed solution of the unsteady aerodynamic loads on moving airfoils inaccurate and sensitive to small errors in the computed steady flow field.

To overcome some of the difficulties associated with fixed grid potential calculations, Whitehead and Grant [56] introduced a linearized potential transformation that can be viewed as a rigid-body motion of the grid. Because the grid in effect moves with the airfoil, the scheme does not require extrapolation terms at the airfoil boundaries. While this approach allows rigid-body motions of airfoils to be analyzed, flexible mode shapes, which are common in turbomachinery aeroelasticity, cannot be analyzed. Recently, Hall [21] developed a linearized potential analysis that uses a deforming grid and is capable of analyzing both rigid-body and elastic airfoil motions.

The present research presents a deforming grid linearized Euler solver that is suitable for the aerodynamic damping calculation of turbomachinery blades. It is demonstrated that the use of a deforming grid results in significantly more accurate predictions of the unsteady flow field and aerodynamic loads. Because the grid deforms elastically, the method can analyze both rigid-body and flexible blade motions. Furthermore, as implemented in the present method, the additional computational analysis required to use the deforming grid need only be calculated once before the start of the basic numerical integration scheme, hence the moving grid adds virtually no computational expense.

The second gain in accuracy results from the implementation of numerically exact nonreflecting far-field boundary conditions. Accurate unsteady flow computations demand nonreflecting boundaries to prevent any spurious reflections from corrupting the solution. Previous investigators [19,24,49,56] have derived the exact analytical behavior of linearized potential and Euler equations in the far-field and then matched these results to the numerical solutions computed in the near field. The present work

presents an alternative approach, whereby, the numerically exact, far-field behavior is found from an eigenanalysis of the discretized equations. The resulting eigenmodes are then used to construct the numerically exact, nonreflecting boundary conditions.

## 1.3 Outline

In Chapter 2, the governing nonlinear Euler equations are presented. The small disturbance assumption is introduced resulting in the linearized Euler equations which model the small disturbance unsteady flow field. Also introduced is a deforming computational grid which conforms to the motion of the vibrating airfoils. Finally, the analytical problem is closed with the introduction of the near-field boundary conditions.

In Chapter 3, the basic (i.e., subsonic) numerical integration scheme is developed. The properties of the scheme, including accuracy, consistency and stability, are examined using a model equation. Also discussed are grid generation techniques, and acceleration techniques such as multiple grid acceleration and local time stepping.

In Chapter 4, a new numerically exact far-field boundary condition formulation is presented. To put this new technique into perspective, more traditional analytical boundary condition treatments are first reviewed. The new exact formulation, which makes use of the eigenmodes of the discretized small disturbance equations, is then presented.

Chapter 5 presents numerical predictions of unsteady flows computed using the present method for several cascade configurations operating in the subsonic regime. Solutions obtained are compared to several approaches including analytical and semi-analytical methods, computational methods, and experimental data. Both the accuracy and efficiency of the present method are examined.

Chapter 6 introduces the theory and resulting modifications to the previously developed algorithm needed to model transonic flows using shock capturing. The idea of a conservative linearization is developed and the effects of nonconservation on the unsteady solution are explored. Test cases are then presented which depend on these modifications and the results are compared to nonlinear computational data.

Finally, Chapter 7 concludes the report with observations about the usefulness of the present method as a design tool. In addition, conclusions from the present analysis and recommendations for future work in this area are presented.

# Chapter 2

## Governing Equations

This chapter begins with the development of the integral form of the Euler equations valid for a deforming control volume. Next, the Euler equations are linearized to obtain a description of the small disturbance unsteady flows in cascades. First, a deforming computational grid which conforms to the motion of vibrating airfoils is defined. Then the Euler equations are linearized in a frame of reference attached to the moving grid. Subsequently, the preceding results are coupled together to obtain the linearized Euler equations valid on a continuously deforming grid. Finally, the analytic problem is completed by specifying appropriate near-field boundary conditions.

### 2.1 The Nonlinear Euler Equations

The general technique for obtaining the equations governing fluid motion is to consider a small, deformable control volume (Fig. 2.1) through which the fluid moves, and to require that mass, momentum and energy be conserved. This produces four equations which, when combined with an equation of state, provide sufficient information for the determination of the four conservation variables:  $\rho$ ,  $\rho u$ ,  $\rho v$ ,  $e$ , where  $\rho$  is the density,  $e$  is the internal energy, and  $u$  and  $v$  are the  $x$ - and  $y$ -components of the fluid velocity.

The present analysis makes the following assumptions. The flow is inviscid, implying that shear stresses are absent and hence the tangential velocity of the fluid at a solid surface boundary does not necessarily vanish as it must for a viscous fluid. A consequence of this simplification is that only surface forces which act perpendicular to the control surface (i.e., pressure) are present. In addition, it is assumed that there are no body forces present. Hence gravitational, electrostatic, and magnetic effects are neglected. Finally, the flow is assumed to be adiabatic and the fluid is assumed to be thermally perfect. The consequence of the first assumption is that no heat is transferred to or from the surroundings. The second assumption implies the gas obeys the ideal gas law. With these simplifying assumptions, one can construct the governing equations of the fluid motion for a deforming control volume.

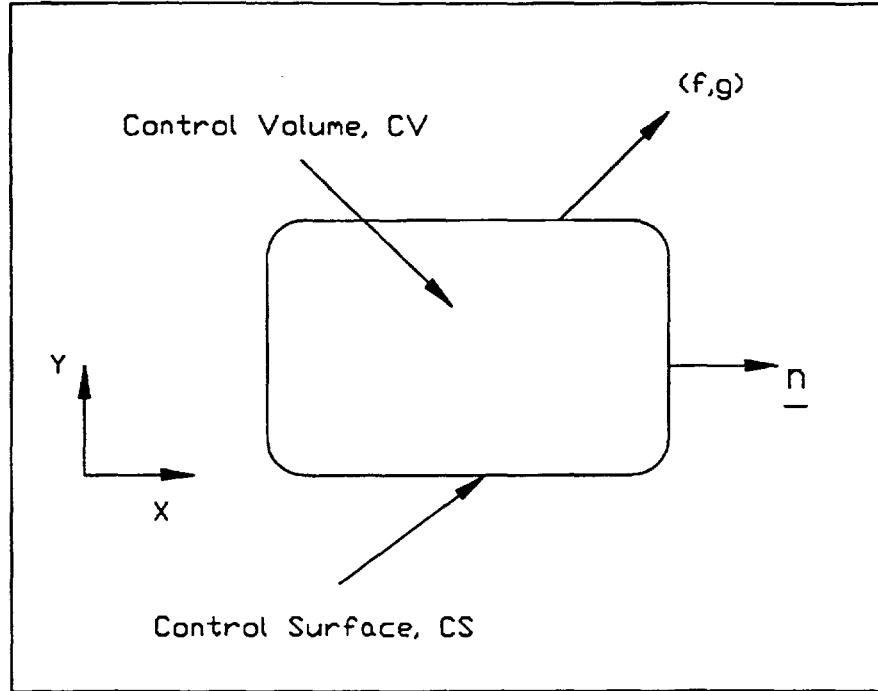


Figure 2.1: Typical control volume

### 2.1.1 Continuity Equation

The conservation of mass requires that the time rate of change of mass within the control volume be equal to the mass flux crossing the control surface. In integral form,

$$\frac{d}{dt} \iint_{cv} \rho \, dx dy + \oint_{cs} \left( \rho u - \rho \frac{\partial f}{\partial t} \right) dy - \oint_{cs} \left( \rho v - \rho \frac{\partial g}{\partial t} \right) dx = 0 \quad (2.1)$$

where  $f$  and  $g$  correspond to the displacement of the control volume in the  $x$ - and  $y$ -directions.

### 2.1.2 Momentum Equation

Newton's second law of motion states that the time rate of change of linear momentum of a given set of fluid particles is equal to the sum of the forces acting on the fluid. Using Reynolds' transport equation, the conservation of linear momentum is given by

$$\frac{d}{dt} \iint_{cv} \rho u \, dx dy + \oint_{cs} \left( \rho u^2 + p - \rho u \frac{\partial f}{\partial t} \right) dy - \oint_{cs} \left( \rho uv - \rho u \frac{\partial g}{\partial t} \right) dx = 0 \quad (2.2)$$

$$\frac{d}{dt} \iint_{cv} \rho v \, dx dy + \oint_{cs} \left( \rho uv - \rho v \frac{\partial f}{\partial t} \right) dy - \oint_{cs} \left( \rho v^2 + p - \rho v \frac{\partial g}{\partial t} \right) dx = 0 \quad (2.3)$$

where  $p$  is the static pressure.

### 2.1.3 Energy Equation

The first law of thermodynamics states (neglecting potential energy) that the time rate of change of internal energy plus kinetic energy of a system is equal to the rate of heat transfer into the system less the rate of work done by the system. Coupled with the assumption that the fluid is an ideal gas, and again using Reynolds' transport equation, the conservation of energy is given by

$$\frac{d}{dt} \iint_{cv} e \, dx dy + \oint_{cs} \left( \rho u h_o - e \frac{\partial f}{\partial t} \right) dy - \oint_{cs} \left( \rho v h_o - e \frac{\partial g}{\partial t} \right) dx = 0 \quad (2.4)$$

where  $h_o$  is the total enthalpy given by

$$h_o = \frac{e + p}{\rho} = \frac{\gamma}{\gamma - 1} \frac{p}{\rho} + \frac{1}{2} (u^2 + v^2) \quad (2.5)$$

### 2.1.4 Summary

Using the results we have just obtained, we can now state in vector and conservation form the governing equations of the fluid. For a Cartesian coordinate system the Euler equations can be written as

$$\frac{d}{dt} \iint_{cv} \mathbf{U} \, dx dy + \oint_{cs} \left( \mathbf{F} - \mathbf{U} \frac{\partial f}{\partial t} \right) dy - \oint_{cs} \left( \mathbf{G} - \mathbf{U} \frac{\partial g}{\partial t} \right) dx = 0 \quad (2.6)$$

where  $\mathbf{U}$  is the vector of conservation variables and  $\mathbf{F}$  and  $\mathbf{G}$  represent the flux vectors described below.

$$\mathbf{U} = \begin{bmatrix} \rho \\ \rho u \\ \rho v \\ e \end{bmatrix}, \quad \mathbf{F} = \begin{bmatrix} \rho u \\ \rho u^2 + p \\ \rho uv \\ \rho u h_o \end{bmatrix}, \quad \mathbf{G} = \begin{bmatrix} \rho v \\ \rho uv \\ \rho v^2 + p \\ \rho v h_o \end{bmatrix} \quad (2.7)$$

It can be shown that the Euler equations in differential form are given by

$$\frac{\partial \mathbf{U}}{\partial t} + \frac{\partial \mathbf{F}}{\partial x} + \frac{\partial \mathbf{G}}{\partial y} = 0 \quad (2.8)$$

## 2.2 Linearization Of The Euler Equations

Having developed the governing equations, in this section the nonlinear unsteady flow is decomposed into a nonlinear mean (steady) flow and a linear, harmonically varying perturbation flow. As previously stated, this analysis is performed on a continuously deforming grid to improve the accuracy of the method. When the formal development is presented, the ensuing linearized Euler equations will contain inhomogeneous terms which arise from the grid deformation. Hence, the system of equations to be discretized are linear, variable coefficient, inhomogeneous partial differential equations.

### 2.2.1 Computational Coordinate System

Most previous linearized analyses have used computational grids which are fixed in space. For flutter calculations this implies that the cascade of airfoils vibrate through the stationary grid. To apply the appropriate upwash boundary condition at the airfoil surface, an extrapolation from the mean position of the airfoil to the instantaneous airfoil position must be performed. This procedure produces additional extrapolation terms in the airfoil upwash boundary condition; these extrapolation terms are quite large and difficult to evaluate accurately, especially in the regions near the leading and trailing edges. In this investigation, we avoid this difficulty by using a deformable grid which conforms to the motion of the airfoils. Since the airfoil motion is restricted to small amplitude, harmonic motion, the grid motion is similarly constrained. When implemented, no troublesome extrapolation terms are required in the application of the upwash boundary condition.

The physical coordinates  $(x, y, t)$  are related to the computational coordinates  $(\xi, \eta, \tau)$  by the following transformation.

$$x(\xi, \eta, \tau) = \xi + f(\xi, \eta)e^{j\omega\tau} \quad (2.9)$$

$$y(\xi, \eta, \tau) = \eta + g(\xi, \eta)e^{j\omega\tau} \quad (2.10)$$

$$t(\xi, \eta, \tau) = \tau \quad (2.11)$$

The functions  $f$  and  $g$  are chosen so that the motion of the grid on the boundaries conforms to the motion of the airfoils and are in general complex to include phase differences between adjacent airfoils. In the interior of the computational domain, it is desirable that  $f$  and  $g$  be continuous and smooth functions to minimize the truncation error of the numerical integration procedure. Thus, a natural choice is to let the values of  $f$  and  $g$  be determined by the solution of Laplace's equation with appropriate boundary conditions.

A typical example of unsteady grid motion can be seen in Fig. 2.2. These figures depict the computational and physical grids for the Tenth Standard Configuration airfoils undergoing a pitching motion with an interblade phase angle,  $\sigma$ , of  $90^\circ$ . In the computational coordinate system, the airfoils and the grid appear to be stationary; in the physical domain, the airfoils and grid continuously deform.

### 2.2.2 Flow Decomposition

Now that the grid motion has been defined, a similar expansion of the flow variables using the same assumption of small harmonic perturbations is proposed, i.e.,

$$\hat{U}(\xi, \eta, \tau) = \bar{U}(\xi, \eta) + u'(\xi, \eta)e^{j\omega\tau} \quad (2.12)$$

Here,  $\bar{U}$  is the vector of conservation variables representing the zeroth order or mean flow field, and  $u'$  is the vector of small perturbation harmonic amplitudes of the conservation variables representing the first order or unsteady flow field. It is now apparent that there are two sources on unsteadiness. These are: the unsteadiness associated with the small perturbation of conservation variables and the unsteadiness

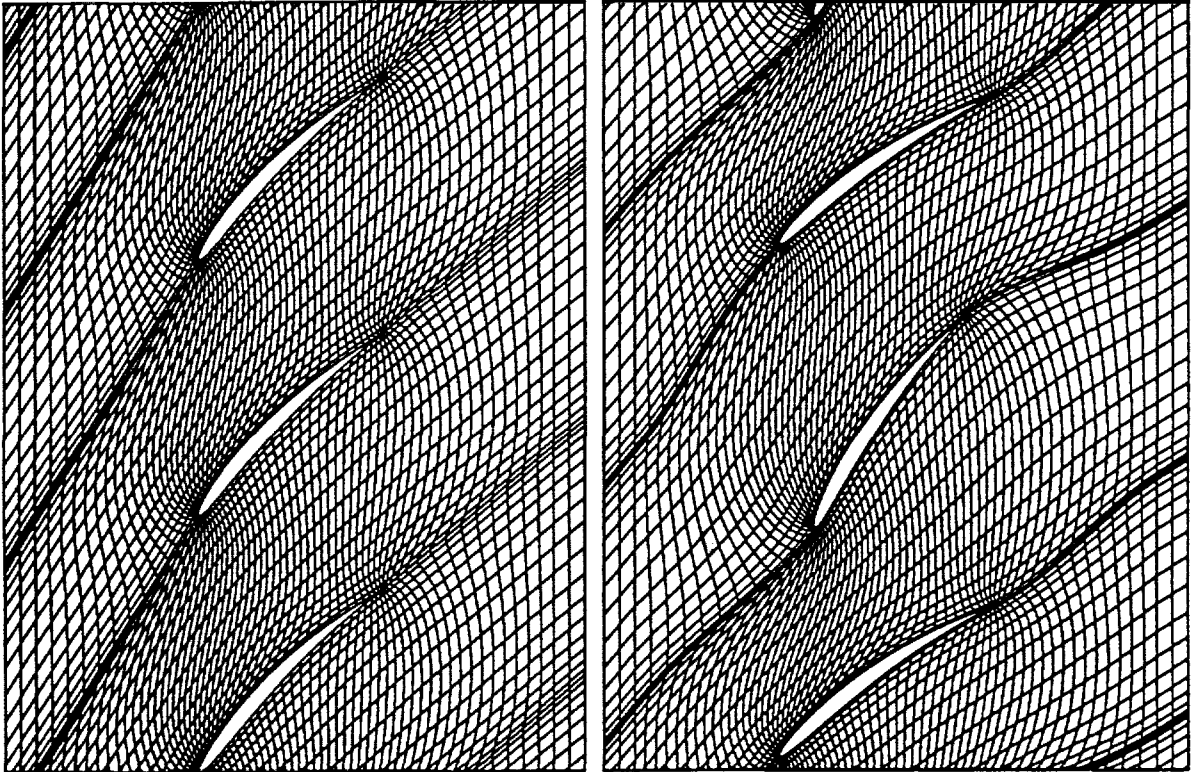


Figure 2.2: Left: Unsteady grid in computational coordinate system  $(\xi, \eta)$ . Right: Unsteady grid in physical coordinate system  $(x, y)$  for the case of a cascade of airfoils pitching about their midchords with an interblade phase angle,  $\sigma$ , of  $90^\circ$ . Flow calculations are performed using a single blade passage. Multiple passages are shown for clarity.

associated with the motion of the steady flow as seen by an observer attached to a frame of reference in the deforming computational grid.

In a similar manner the flux vectors and the individual components of the state vector can be expanded in a perturbation series as follows:

$$\hat{\mathbf{F}}(\xi, \eta, \tau) = \overline{\mathbf{F}}(\overline{\mathbf{U}}) + \frac{\partial \overline{\mathbf{F}}}{\partial \overline{\mathbf{U}}} \mathbf{u}' e^{j\omega\tau} \quad (2.13)$$

$$\hat{\mathbf{G}}(\xi, \eta, \tau) = \overline{\mathbf{G}}(\overline{\mathbf{U}}) + \frac{\partial \overline{\mathbf{G}}}{\partial \overline{\mathbf{U}}} \mathbf{u}' e^{j\omega\tau} \quad (2.14)$$

$$\begin{aligned} \hat{\rho}(\xi, \eta, \tau) &= \overline{\rho}(\xi, \eta) + \rho'(\xi, \eta) e^{j\omega\tau} \\ \hat{\rho}\hat{u}(\xi, \eta, \tau) &= \overline{\rho u}(\xi, \eta) + \rho u'(\xi, \eta) e^{j\omega\tau} \\ \hat{\rho}\hat{v}(\xi, \eta, \tau) &= \overline{\rho v}(\xi, \eta) + \rho v'(\xi, \eta) e^{j\omega\tau} \\ \hat{e}(\xi, \eta, \tau) &= \overline{e}(\xi, \eta) + e'(\xi, \eta) e^{j\omega\tau} \end{aligned} \quad (2.15)$$

where  $\partial \overline{\mathbf{F}}/\partial \overline{\mathbf{U}}$  and  $\partial \overline{\mathbf{G}}/\partial \overline{\mathbf{U}}$  are the Jacobians, which can be written as

$$\frac{\partial \overline{\mathbf{F}}}{\partial \overline{\mathbf{U}}} = \begin{bmatrix} 0 & 1 & 0 & 0 \\ \frac{\gamma-3}{2}\overline{U}^2 + \frac{\gamma-1}{2}\overline{V}^2 & -(\gamma-3)\overline{U} & -(\gamma-1)\overline{V} & \gamma-1 \\ -\overline{UV} & \overline{V} & \overline{U} & 0 \\ \overline{U}(\frac{\gamma-1}{2}V_T^2 - h_o) & h_o - (\gamma-1)\overline{U}^2 & -(\gamma-1)\overline{UV} & \gamma\overline{U} \end{bmatrix} \quad (2.16)$$

and

$$\frac{\partial \overline{\mathbf{G}}}{\partial \overline{\mathbf{U}}} = \begin{bmatrix} 0 & 0 & 1 & 0 \\ -\overline{UV} & \overline{V} & \overline{U} & 0 \\ \frac{\gamma-3}{2}\overline{V}^2 + \frac{\gamma-1}{2}\overline{U}^2 & -(\gamma-1)\overline{U} & -(\gamma-3)\overline{V} & \gamma-1 \\ \overline{V}(\frac{\gamma-1}{2}V_T^2 - h_o) & -(\gamma-1)\overline{UV} & h_o - (\gamma-1)\overline{V}^2 & \gamma\overline{V} \end{bmatrix} \quad (2.17)$$

where  $V_T^2 = \overline{U}^2 + \overline{V}^2$ .

## 2.3 Linearized Euler Equations In Computational Domain

Recall (Eq. 2.6) that the vector form of the governing equations for a deforming control volume is given by

$$\frac{d}{dt} \iint_{cv} \hat{\mathbf{U}} dx dy + \oint_{cs} \left( \hat{\mathbf{F}} - \hat{\mathbf{U}} \frac{\partial f}{\partial t} \right) dy - \oint_{cs} \left( \hat{\mathbf{G}} - \hat{\mathbf{U}} \frac{\partial g}{\partial t} \right) dx = 0$$

Substitution of the perturbation assumptions into the conservation equations described by Eq. 2.6 yields

$$\begin{aligned}
& \frac{d}{d\tau} \iint_{cv} (\bar{U} + \mathbf{U}' e^{j\omega\tau}) (d\xi + df e^{j\omega\tau}) (d\eta + dg e^{j\omega\tau}) \\
& + \oint_{cs} \left( \bar{F} + \frac{\partial \bar{F}}{\partial \bar{U}} \mathbf{u}' e^{j\omega\tau} - j\omega f \bar{U} e^{j\omega\tau} \right) (d\eta + dg e^{j\omega\tau}) \\
& - \oint_{cs} \left( \bar{G} + \frac{\partial \bar{G}}{\partial \bar{U}} \mathbf{u}' e^{j\omega\tau} - j\omega g \bar{U} e^{j\omega\tau} \right) (d\xi + df e^{j\omega\tau}) = 0 \quad (2.18)
\end{aligned}$$

Grouping terms of zeroth and first order results in the mean flow and small disturbance equations respectively. The mean flow Euler equations represented in integral form are

$$\oint_{cs} \bar{F} d\eta - \oint_{cs} \bar{G} d\xi = 0 \quad (2.19)$$

Equation 2.19 is the familiar integral representation of the two-dimensional Euler equations.

Similarly, the resultant linearized Euler equations in integral form are

$$\begin{aligned}
& \iint_{cv} j\omega \mathbf{u}' d\xi d\eta + \iint_{cv} j\omega \bar{U} d\xi dg + \iint_{cv} j\omega \bar{U} d\eta df \\
& + \oint_{cs} \left( \bar{F} dg + \frac{\partial \bar{F}}{\partial \bar{U}} \mathbf{u}' d\eta - j\omega f \bar{U} d\eta \right) \\
& - \oint_{cs} \left( \bar{G} df + \frac{\partial \bar{G}}{\partial \bar{U}} \mathbf{u}' d\xi - j\omega g \bar{U} d\xi \right) = 0 \quad (2.20)
\end{aligned}$$

Written in this manner, each first order term from Eq. 2.18 has an obvious corresponding term in Eq. 2.20. For example, the first row of Eq. 2.20 represents the first order perturbation of the first row of Eq. 2.18. In the first row of Eq. 2.20, the first term represents the unsteadiness in the first term of Eq. 2.18 due to the perturbation  $\mathbf{u}'$  while the second and third terms in Eq. 2.20 represent the unsteadiness due to the grid motion. Rewriting Eq. 2.20 so that the homogeneous terms and inhomogeneous terms are separated gives

$$\begin{aligned}
& j\omega \iint_{cv} \mathbf{u}' d\xi d\eta + \oint_{cs} \left( \frac{\partial \bar{F}}{\partial \bar{U}} \mathbf{u}' d\eta - \frac{\partial \bar{G}}{\partial \bar{U}} \mathbf{u}' d\xi \right) = \\
& \quad - j\omega \iint_{cv} \bar{U} (d\xi dg + df d\eta) \\
& + j\omega \oint_{cs} (f \bar{U} d\eta - g \bar{U} d\xi) - \oint_{cs} (\bar{F} dg - \bar{G} df) \quad (2.21)
\end{aligned}$$

where the homogeneous terms (homogeneous in  $u'$ ) appear on the left and the inhomogeneous terms appear on the right.

It is apparent that the mean flow as described by Eq. 2.19 is independent of the unsteady perturbation flow. The perturbation flow, on the other hand, depends upon the steady flow in two ways. Recall that the linearized Euler equations are linear, inhomogeneous, variable coefficient differential equations. The variable coefficients (essentially the Jacobians) are functions of the mean flow field. Second, the inhomogeneous portion of Eq. 2.21 (the right-hand side) is a function of only the steady flow field and the prescribed grid motion (for the gust response problem, the inhomogeneous term is identically zero since the computational grid is nondeforming). Hence, the right hand side of Eq. 2.21 need only be calculated once at the beginning of the iteration procedure. For this reason, the use of a deforming grid adds very little to the total computational time of the algorithm. In addition, the Jacobians need only be calculated once and then can be stored for later use significantly reducing the number of required floating point operations per iteration.

For numerical integration of Eq. 2.21, it is convenient to make the mean flow variables,  $\bar{U}$ , and the perturbation variables,  $u'$ , artificially time dependent. As suggested by Ni and Sisto [30], let

$$\hat{U}(\xi, \eta, \tau) = \bar{U}(\xi, \eta, \tau) + u'(\xi, \eta, \tau)e^{j\omega\tau} \quad (2.22)$$

Substitution of this assumption into the nonlinear Euler equations, Eq. 2.6, and again collecting terms of equal order gives

$$\frac{d}{d\tau} \iint_{cv} \bar{U} d\xi d\eta + \oint_{cs} \bar{F} d\eta - \oint_{cs} \bar{G} d\xi = 0 \quad (2.23)$$

and

$$\begin{aligned} & \frac{d}{d\tau} \iint_{cv} u' d\xi d\eta + j\omega \iint_{cv} u' d\xi d\eta + \oint_{cs} \left( \frac{\partial \bar{F}}{\partial \bar{U}} u' d\eta - \frac{\partial \bar{G}}{\partial \bar{U}} u' d\xi \right) = \\ & - j\omega \iint_{cv} \bar{U} (d\xi dg + df d\eta) + j\omega \oint_{cs} (f \bar{U} d\eta - g \bar{U} d\xi) - \oint_{cs} (\bar{F} dg - \bar{G} df) \end{aligned} \quad (2.24)$$

Now both the nonlinear mean flow equations and the linearized Euler equations contain explicit time derivative terms making the equations hyperbolic in time. This allows solution of the equations using conventional time-marching algorithms. The equations are marched in time until the conservation variables reach their steady state values. Hence, the time derivative terms in Eqs. 2.23 and 2.24 are driven to zero and the original steady nonlinear and linearized unsteady Euler equations are recovered. Furthermore, since only the steady state values of the mean and perturbation flow conservation variables are desired, there is no need to time march the equations time accurately; multiple-grid and local time stepping acceleration techniques are used greatly reducing the computational time required to solve an unsteady flow problem.

To obtain the corresponding differential form of the mean and linearized conservation statements (2.23 and 2.24), we must relate the spatial and temporal derivatives

in the physical coordinate system to those in the computational coordinate system. This relationship is given by

$$\begin{pmatrix} \frac{\partial}{\partial x} \\ \frac{\partial}{\partial y} \\ \frac{\partial}{\partial t} \end{pmatrix} = \begin{bmatrix} \frac{\partial \xi}{\partial x} & \frac{\partial \eta}{\partial x} & \frac{\partial \tau}{\partial x} \\ \frac{\partial \xi}{\partial y} & \frac{\partial \eta}{\partial y} & \frac{\partial \tau}{\partial y} \\ \frac{\partial \xi}{\partial t} & \frac{\partial \eta}{\partial t} & \frac{\partial \tau}{\partial t} \end{bmatrix} \begin{pmatrix} \frac{\partial}{\partial \xi} \\ \frac{\partial}{\partial \eta} \\ \frac{\partial}{\partial \tau} \end{pmatrix} = [J] \begin{pmatrix} \frac{\partial}{\partial \xi} \\ \frac{\partial}{\partial \eta} \\ \frac{\partial}{\partial \tau} \end{pmatrix} \quad (2.25)$$

where  $[J]$  is the Jacobian matrix associated with the coordinate transformation. A similar transformation matrix can be obtained for the inverse problem, and will be denoted  $[J]^{-1}$  as shown below

$$\begin{pmatrix} \frac{\partial}{\partial \xi} \\ \frac{\partial}{\partial \eta} \\ \frac{\partial}{\partial \tau} \end{pmatrix} = \begin{bmatrix} \frac{\partial x}{\partial \xi} & \frac{\partial y}{\partial \xi} & \frac{\partial t}{\partial \xi} \\ \frac{\partial x}{\partial \eta} & \frac{\partial y}{\partial \eta} & \frac{\partial t}{\partial \eta} \\ \frac{\partial x}{\partial \tau} & \frac{\partial y}{\partial \tau} & \frac{\partial t}{\partial \tau} \end{bmatrix} \begin{pmatrix} \frac{\partial}{\partial x} \\ \frac{\partial}{\partial y} \\ \frac{\partial}{\partial t} \end{pmatrix} = [J]^{-1} \begin{pmatrix} \frac{\partial}{\partial x} \\ \frac{\partial}{\partial y} \\ \frac{\partial}{\partial t} \end{pmatrix} \quad (2.26)$$

Substituting the small motion assumption of Eqs. 2.9 through 2.11 into the  $[J]^{-1}$  matrix and inverting, the  $[J]$  matrix is found to be given by

$$[J] = \begin{bmatrix} 1 - f_\xi & -g_\xi & 0 \\ -f_\eta & 1 - g_\eta & 0 \\ -f_\tau & -g_\tau & 1 \end{bmatrix} \quad (2.27)$$

where only zeroth and first order terms have been retained.

The derivatives in the physical coordinates can now be represented in terms of the grid coordinates as follows:

$$\frac{\partial}{\partial x} = \frac{\partial}{\partial \xi} - \left( f_\xi \frac{\partial}{\partial \xi} + g_\xi \frac{\partial}{\partial \eta} \right) \quad (2.28)$$

$$\frac{\partial}{\partial y} = \frac{\partial}{\partial \eta} - \left( f_\eta \frac{\partial}{\partial \xi} + g_\eta \frac{\partial}{\partial \eta} \right) \quad (2.29)$$

$$\frac{\partial}{\partial t} = \frac{\partial}{\partial \tau} - \left( f_\tau \frac{\partial}{\partial \xi} + g_\tau \frac{\partial}{\partial \eta} \right) \quad (2.30)$$

Thus, in vector form, the differential representation of the linearized Euler equations in the computational domain is given by

$$j\omega \mathbf{u}' + \frac{\partial}{\partial \xi} \frac{\partial \overline{\mathbf{F}}}{\partial \overline{\mathbf{U}}} \mathbf{u}' + \frac{\partial}{\partial \eta} \frac{\partial \overline{\mathbf{G}}}{\partial \overline{\mathbf{U}}} \mathbf{u}' = \left( f \frac{\partial}{\partial \xi} + g \frac{\partial}{\partial \eta} \right) \overline{\mathbf{U}} + \left( \frac{\partial f}{\partial \xi} \frac{\partial}{\partial \xi} + \frac{\partial g}{\partial \xi} \frac{\partial}{\partial \eta} \right) \overline{\mathbf{F}} + \left( \frac{\partial f}{\partial \eta} \frac{\partial}{\partial \xi} + \frac{\partial g}{\partial \eta} \frac{\partial}{\partial \eta} \right) \overline{\mathbf{G}} \quad (2.31)$$

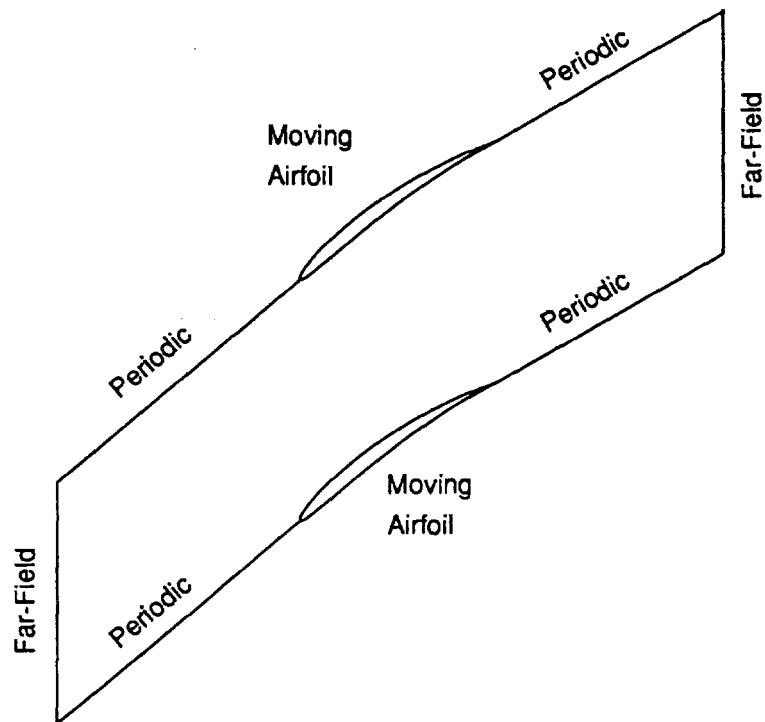


Figure 2.3: Classification of boundary types in computational domain

## 2.4 Near-Field Boundary Conditions

To complete the specification of the unsteady flow problem, boundary conditions must be specified around the entire computational domain as shown in Fig. 2.3. There are essentially three types of unsteady boundary conditions. The solid surface, or no through flow condition dictates that there be no flux of mass through solid surfaces. Periodic boundary conditions are applied upstream and downstream of the cascade to reduce the computational domain to a single blade passage. Finally, far-field boundary conditions are necessary to prevent spurious reflections of outgoing waves at the upstream and downstream computational boundaries (the development of the far-field boundary conditions is deferred until Chapter 4).

### 2.4.1 Solid Surface

The solid surface boundary condition is necessary to ensure that no flow passes through the surface of the airfoil. The development of this boundary condition will begin with the full unsteady nonlinear representation of this statement which is given by

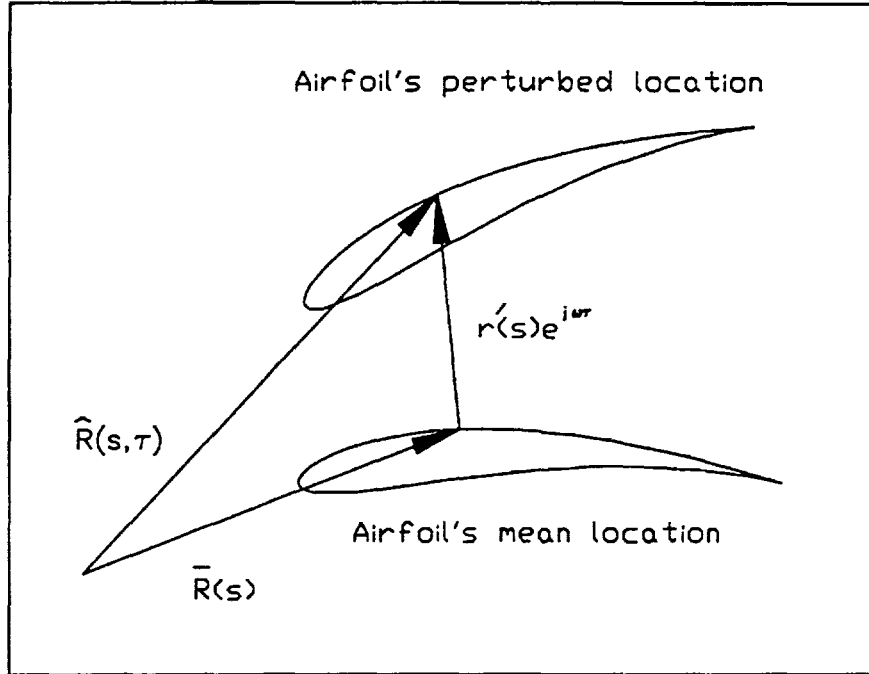


Figure 2.4: Illustration of position vectors for flow tangency boundary condition

$$\hat{\mathbf{V}}(\xi, \eta, \tau) \cdot \hat{\mathbf{n}}(s, \tau) - \frac{\partial \hat{\mathbf{R}}(s, \tau)}{\partial \tau} \cdot \hat{\mathbf{n}}(s, \tau) \quad (2.32)$$

Figure 2.4 illustrates the location of the airfoil surface at its mean and perturbed location.  $\bar{\mathbf{R}}(s, \tau)$  describes the location of the reference airfoil's surface at time  $\tau$ , where  $s$  is the distance along the airfoil surface.

In a manner analogous to that developed in the section pertaining to flow decomposition, the unit normal vector and the airfoil's position vector can be expanded in perturbation series:

$$\hat{\mathbf{R}}(s, \tau) = \bar{\mathbf{R}}(s) + \mathbf{r}'(s)e^{j\omega\tau} \quad (2.33)$$

$$\hat{\mathbf{n}}(s, \tau) = \bar{\mathbf{n}}(s) + \mathbf{n}'(s)e^{j\omega\tau} \quad (2.34)$$

$$\hat{\mathbf{V}}(s, \tau) = \bar{\mathbf{V}}(s) + \mathbf{v}'(s)e^{j\omega\tau} \quad (2.35)$$

Substitution of Eqs. 2.33 through 2.35 into Eq. 2.32 yields

$$(\bar{\mathbf{V}} + \mathbf{v}') \cdot (\bar{\mathbf{n}} + \mathbf{n}') - \frac{\partial (\bar{\mathbf{R}} + \mathbf{r}')}{\partial \tau} \cdot (\bar{\mathbf{n}} + \mathbf{n}') \quad (2.36)$$

where

$$\mathbf{r}' = (f, g) \quad (2.37)$$

Recall that  $f$  and  $g$  are the functions that represent the first order unsteady grid motion. Collecting terms of zeroth and first order describes the steady and unsteady flow tangency conditions respectively,

$$\bar{\mathbf{V}} \cdot \bar{\mathbf{n}} = 0 \quad (2.38)$$

$$\mathbf{v}' \cdot \bar{\mathbf{n}} = -\bar{\mathbf{V}} \cdot \mathbf{n}' + j\omega(f, g) \cdot \bar{\mathbf{n}} \quad (2.39)$$

Equation 2.38 is clearly a statement restricting the steady flow to be tangent to the blade surface. The unsteady counterpart to the flow tangency condition, Eq. 2.39, states that the normal perturbation flow velocity must be equal to the upwash on the surface of the airfoil attributed to its unsteady motion. The first term on the right side of Eq. 2.39 is the upwash associated with a rotation of the blade surface, whereas the second term is the upwash associated with a translation of the blade surface. The benefit of using a deforming grid is now clearly evident. There are no terms in Eq. 2.39 that represent extrapolations of the blade's position to a mean location in order to apply the unsteady boundary condition. Finally, it should be noted that the upwash is only a function of the steady flow and the specified grid motion. Both of these quantities are known prior to the iteration procedure.

### 2.4.2 Periodicity

Because the unsteady flow is governed by linear equations, the response of the cascade to blade motion or a gust may be found by decomposing the disturbance into a sum of travelling wave modes, each having a different frequency,  $\omega$ , and interblade phase angle,  $\sigma$ . By superposition, the total response of the cascade is equivalent to the sum of the response to each of the individual modes. Therefore, without any loss in generality, only one travelling wave mode need be considered at a time. The unsteady periodicity condition upstream and downstream of the cascade is then

$$\mathbf{u}'(\xi, \eta + G) = \mathbf{u}'(\xi, \eta)e^{j\sigma} \quad (2.40)$$

where  $G$  is the blade-to-blade gap (see Fig. 2.5). This periodicity condition allows the computational domain to be reduced to a single blade passage which significantly reduces memory requirements and computational time.

## 2.5 Summary

In this chapter, the linearized Euler equations were developed. Included in this analysis was the effect of a deforming computational grid. Near-field boundary conditions were presented to complete the specification of the unsteady aerodynamic model. In the next chapter, a numerical integration scheme for solving the linearized Euler equations will be presented.

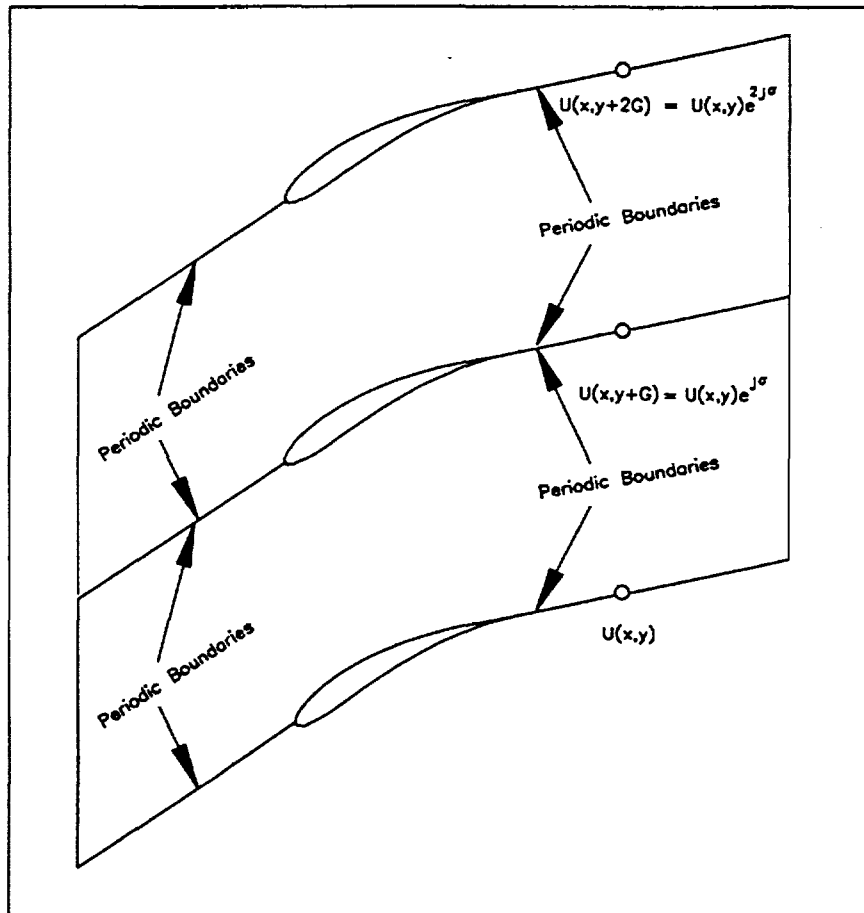


Figure 2.5: Illustration of the periodic boundary condition

# Chapter 3

## Basic Numerical Integration Scheme

Over the last two decades numerous computational methods have been developed to solve the steady Euler equations (e.g., [13,37,39]). One goal of the present research, is to adapt proven steady flow solvers to solve the unsteady linearized Euler equations. An advantage of this approach is the same algorithm can be used in the solution of both the steady, nonlinear Euler equations and the linearized, unsteady Euler equations. Additionally, the Lax-Wendroff algorithm method selected has been proven to be an efficient and effective way of solving the nonlinear Euler equations and is believed to be equally effective when applied to the linearized Euler equations. With this in mind, the main goal of this chapter is to present the basic numerical integration method used in the present analysis. In addition, issues of grid generation and numerical properties of the integration scheme such as stability, consistency, and accuracy are investigated.

### 3.1 Unsteady Grid Generation

The primary focus of the present work is the development of a numerical tool aeroelasticians can use to calculate unsteady flows in turbomachinery applications. Toward that end, the steady Euler and linearized Euler equations will be discretized and solved using a finite volume technique. Before proceeding, however, a computational mesh must be constructed to specify the discrete locations where the solution is to be found. It is well known that the quality of the grid used can significantly affect the results. Therefore, while grid generation is not the primary focus of this research, a brief development of the grid generation techniques used is presented for completeness.

The problem of grid generation has been an area of active research for many years [2,44]. Generally, the greater the resolution the more accurate the results. On the other hand, the greater the resolution, the more computational time and resources are required to solve the problem. This introduces one of the fundamental problems of grid generation: how to balance the resolution required to obtain a reasonable solution with an acceptable amount of computational resources. Another desire is that the grid lines be nearly orthogonal everywhere as most finite difference and finite volume schemes produce large truncation errors when the grid is highly skewed. Although this

may be possible, it comes at the expense of added complexity in the grid generation algorithm. In addition, some skewedness is permissible without significantly affecting the solution. Finally, adjacent cells should be approximately the same size, since rapid changes in the size of the computational cell can introduce error as well as lead to stability problems. These factors and others are taken into consideration when ascertaining the quality of the mesh. It is for these reasons that there is an art associated with grid generation that is outside the scope of the present research.

Since the unsteady grid motion is comprised of a steady (mean) grid plus a harmonically varying small perturbation, it is necessary to compute first a steady grid about which the unsteady grid motion can be linearized. In the generation of the steady grid, a modified version of an elliptic mesh generator developed by Thompson [44] is used. The principle behind this grid generation technique is to prescribe the boundary points in the physical domain and then map the specified computational grid into the irregular physical domain by solving an elliptic PDE with the appropriate boundary conditions.

With the steady grid generated it is now necessary to generate the unsteady grid motion. Recall that the position  $(x, y)$  of a grid point is given by

$$\begin{aligned}x &= \xi + f(\xi, \eta)e^{j\omega\tau} \\y &= \eta + g(\xi, \eta)e^{j\omega\tau}\end{aligned}\tag{3.1}$$

For cases involving blade motion, the complex amplitude of the grid motion  $(f, g)$  must be specified at every grid point in the computational domain. Since the mode shape of the blade vibration is known, the quantities  $f$  and  $g$  are prescribed on the solid surface boundaries to match the prescribed airfoil motion. Upstream and downstream of the airfoil, the values of  $f$  and  $g$  on the boundary are prescribed to “smoothly” vanish as the far field is approached. The requirement that the motion of the grid vanish in the far field is made to simplify the far-field boundary condition development in Section 4.3. Additionally, the grid motion must satisfy a complex periodicity condition similar to that prescribed on the unsteady flow variables.

With the values of  $f$  and  $g$  now prescribed around the entire computational domain, the problem now is to determine the motion in the interior. In principle the distribution could be arbitrary. However, a smooth grid distribution reduces truncation errors in the unsteady flow computation. Therefore, in the present work, the motion of the grid on the interior is described by Laplace’s equation so that

$$\begin{aligned}\nabla^2 f &= 0 \\ \nabla^2 g &= 0\end{aligned}\tag{3.2}$$

subject to the Dirichlet boundary conditions specified above. A finite element scheme is used to discretize the equations on the steady grid. The equations are then solved directly using LU decomposition. Because the motion of the grid is harmonic, the solution of the grid motion need only be determined once before the iterative solution procedure begins. Figure 2.2 shows the computational grid (steady) and physical grid (unsteady deforming) for a typical unsteady flow calculation.

### 3.2 Basic Lax-Wendroff Integration Scheme (One-Dimensional Model)

When deciding which integration scheme to use in the present research, the following factors were considered. First, it is desirable to take advantage of previous experience so as not to duplicate effort. Second, the same algorithm should be used in both the steady and unsteady codes. Third, the scheme should be computationally efficient making use of modern convergence acceleration techniques. Hence, a logical choice for the present research was an adaptation of the Ni scheme [13,37] which is itself a variant of the familiar Lax-Wendroff scheme. The Ni scheme, as traditionally applied to the steady nonlinear Euler equations, is marched in time until a converged solution is obtained. However, since the linearized Euler equations are cast in the frequency domain, they are not explicitly dependant on time. Hence, as suggested by Ni and Sisto, a pseudo time term must be introduced as discussed in section 2.3. The resulting linearized Euler equations in differential form are

$$\frac{\partial u'}{\partial \tau} + j\omega u' + \frac{\partial}{\partial \xi} \frac{\partial \bar{F}}{\partial \bar{U}} u' + \frac{\partial}{\partial \eta} \frac{\partial \bar{G}}{\partial \bar{U}} u' = \mathbf{b} \quad (3.3)$$

where  $\mathbf{b}$  is the right side of Eq. 2.31. Equation 3.3 resembles Eq. 2.31 with the exception that an additional time dependent term now appears on the left side of the equation. This pseudo-time dependent term is driven to zero by time marching the modified linearized Euler equation to steady state, thereby recovering the solution to the original linearized Euler equations (Eq. 2.31).

Ni's Lax-Wendroff scheme can easily be applied to the linearized Euler equations with some minor modifications. To simplify the description of the method, the integration scheme will be presented using the following one-dimensional model equation.

$$\frac{\partial \hat{u}}{\partial t} + \frac{\partial \hat{F}(\hat{u})}{\partial x} = 0 \quad (3.4)$$

If Eq. 3.4 is linearized, the following expression is obtained.

$$j\omega u' + \frac{\partial}{\partial x} \left( \frac{\partial \bar{F}}{\partial \bar{U}} u' \right) = 0 \quad (3.5)$$

Introducing the pseudo time dependence results in the following expression for the perturbation equation,

$$\frac{\partial u'}{\partial t} + j\omega u' + \frac{\partial}{\partial x} \left( \frac{\partial \bar{F}}{\partial \bar{U}} u' \right) = 0 \quad (3.6)$$

This new model equation resembles the linearized Euler equations as written in Eq. 3.4 and it is for this equation that a variation of Ni's scheme will be presented. The variation from the original development arises from the introduction of the  $j\omega u'$  term

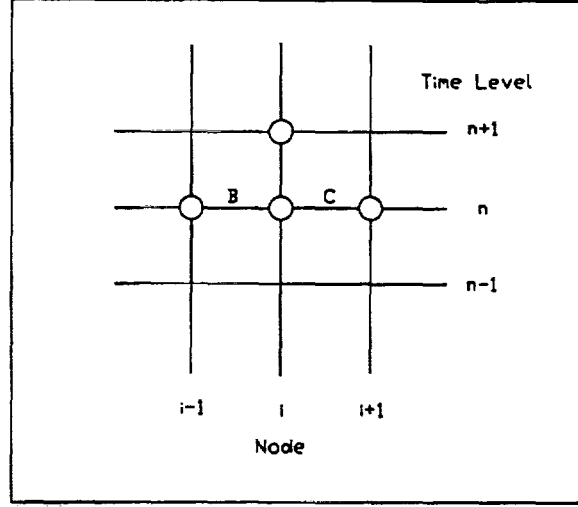


Figure 3.1: Typical computational cell for one-dimensional Ni scheme

which is a result of the linearization process. (In the following development the primes will be omitted for clarity)

To begin, the solution  $u$  is expanded in a Taylor series, resulting in

$$u_i^{n+1} = u_i^n + \left(\frac{\partial u}{\partial t}\right)_i^n \Delta t + \left(\frac{\partial^2 u}{\partial t^2}\right)_i^n \frac{\Delta t^2}{2} + \dots \quad (3.7)$$

$$= u_i^n + \delta u_i \quad (3.8)$$

where the superscript  $n$  refers to the computational time level and the subscript  $i$  refers to the grid location. In Eq. 3.8 is the *correction* in the solution at the  $i^{\text{th}}$  node from one time level to the next. Rewriting Eq. 3.6 gives

$$\frac{\partial u}{\partial t} = - \left[ j\omega u + \frac{\partial}{\partial x} \left( \frac{\partial \bar{F}}{\partial \bar{U}} u \right) \right] \quad (3.9)$$

Differentiating Eq. 3.9 with respect to time and applying the chain rule yields

$$\frac{\partial^2 u}{\partial t^2} = - \left[ j\omega \frac{\partial u}{\partial t} + \frac{\partial}{\partial x} \left( \frac{\partial \bar{F}}{\partial \bar{U}} \frac{\partial u}{\partial t} \right) \right] \quad (3.10)$$

Finally, substituting Eqs. 3.9 and 3.10 into Eq. 3.8 and evaluating at grid index,  $i$ , and time level,  $n$ , with centered finite difference expressions for the spatial derivatives results in the following expression for the change in the state variable from one time level to the next.

$$\delta u_i = - \left[ \frac{j\omega}{2} \left( \frac{(u_{i-1} + u_i)}{2} + \frac{(u_i + u_{i+1})}{2} \right) - \left( \frac{F'_{i-1} - F'_i}{2\Delta x} \right) + \left( \frac{F'_i - F'_{i+1}}{2\Delta x} \right) \right] \Delta t$$

$$\begin{aligned}
& - \left\{ \frac{j\omega}{2} \left( \frac{\partial u}{\partial t} \Big|_{i-1/2}^n + \frac{\partial u}{\partial t} \Big|_{i+1/2}^n \right) \right. \\
& \left. + \left( \frac{\partial \bar{F}}{\partial \bar{U}} \Big|_{i+1/2}^n \frac{\partial u}{\partial t} \Big|_{i+1/2}^n - \frac{\partial \bar{F}}{\partial \bar{U}} \Big|_{i-1/2}^n \frac{\partial u}{\partial t} \Big|_{i-1/2}^n \right) \frac{1}{\Delta x} \right\} \frac{\Delta t^2}{2} \quad (3.11)
\end{aligned}$$

where

$$F'_i = \frac{\partial \bar{F}}{\partial \bar{U}} \Big|_i u_i \quad (3.12)$$

One advantage of Ni's scheme is that it is cell based. To demonstrate, we introduce the following cell based notation:

$$\Delta u_B = \left( F'_{i-1}{}^n - F'_i{}^n \right) \frac{\Delta t}{\Delta x} \quad , \quad \Delta u_C = \left( F'_i{}^n - F'_{i+1}{}^n \right) \frac{\Delta t}{\Delta x} \quad (3.13)$$

$$\Delta F'_B = \left( \frac{\partial \bar{F}}{\partial \bar{U}} \right)_{i-1/2} \Delta u_B \quad , \quad \Delta F'_C = \left( \frac{\partial \bar{F}}{\partial \bar{U}} \right)_{i+1/2} \Delta u_C \quad (3.14)$$

and

$$\begin{aligned}
\bar{u}_B &= \frac{1}{2} (u_{i-1}^n + u_i^n) \\
\bar{u}_C &= \frac{1}{2} (u_i^n + u_{i+1}^n) \quad (3.15)
\end{aligned}$$

Here  $\Delta u_B$  and  $\Delta u_C$  are called the *changes* at cells  $B$  and  $C$  respectively. The subscript  $B$  refers to the control volume lying between grid points  $i-1$  and  $i$  and, the subscript  $C$  refers to the control volume lying between points  $i$  and  $i+1$  as shown in Fig. 3.1. Cast in this manner, this implies the correction to point  $i$  is composed of two parts. The first part,

$$\begin{aligned}
(\delta u_i)_B &= \frac{1}{2} \left[ \Delta u_B + \Delta F'_B \frac{\Delta t}{\Delta x} - j\omega \Delta \bar{u}_B \right] \\
& - \left[ \frac{j\omega \Delta t}{2} \Delta u_B + \frac{\omega^2 \Delta t^2}{2} \bar{u}_B - j\omega \Delta t \bar{u}_B \left( \frac{\partial \bar{F}}{\partial \bar{U}} \right)_B \frac{\Delta t}{\Delta x} \right] \quad (3.16)
\end{aligned}$$

is the correction due to the change,  $\Delta u_B$ , taking place in control volume  $B$ . The second part,

$$\begin{aligned}
(\delta u_i)_C &= \frac{1}{2} \left[ \Delta u_C - \Delta F'_C \frac{\Delta t}{\Delta x} - j\omega \Delta \bar{u}_C \right] \\
& - \left[ \frac{j\omega \Delta t}{2} \Delta u_C + \frac{\omega^2 \Delta t^2}{2} \bar{u}_C + j\omega \Delta t \bar{u}_C \left( \frac{\partial \bar{F}}{\partial \bar{U}} \right)_C \frac{\Delta t}{\Delta x} \right] \quad (3.17)
\end{aligned}$$

is the correction associated with the change,  $\Delta u_C$ , occurring in control volume  $C$ . Note that the expressions for  $(\delta u_i)_B$  and  $(\delta u_i)_C$  are similar with the exception of the sign on two terms. Although these expressions resemble those presented by Ni [37], there are some important differences. Most notably, there are terms which have a

frequency dependence that are the result of the linearization process. These terms will be shown in a subsequent section to play a major role in the stability of the system.

To summarize, a control volume centered integration method is devised that employs the following operations in the determination of the correction to an arbitrary grid point.

- (1) Sweep through all cells computing the change in each cell using

$$\Delta u_C + j\omega \bar{u}_C = \frac{\Delta t}{\Delta x} \left( F'_i{}^n - F'_{i+1}{}^n \right) + j\omega \left( \frac{u_i + u_{i+1}}{2} \right) \Delta t \quad (3.18)$$

- (2) Determine the corrections to point  $i$  and  $i+1$  through the use of the *distribution* formulae

$$\begin{aligned} (\delta u_i)_C &= \frac{1}{2} \left[ \Delta u_C - \Delta F'_C \frac{\Delta t}{\Delta x} - j\omega \Delta \bar{u}_C \right] \\ &- \left[ \frac{j\omega \Delta t}{2} \Delta u_C + \frac{\omega^2 \Delta t^2}{2} \bar{u}_C + j\omega \Delta t \bar{u}_C \left( \frac{\partial \bar{F}}{\partial \bar{U}} \right)_C \frac{\Delta t}{\Delta x} \right] \end{aligned} \quad (3.19)$$

and

$$\begin{aligned} (\delta u_{i+1})_C &= \frac{1}{2} \left[ \Delta u_C + \Delta F'_C \frac{\Delta t}{\Delta x} - j\omega \Delta \bar{u}_C \right] \\ &- \left[ \frac{j\omega \Delta t}{2} \Delta u_C + \frac{\omega^2 \Delta t^2}{2} \bar{u}_C - j\omega \Delta t \bar{u}_C \left( \frac{\partial \bar{F}}{\partial \bar{U}} \right)_C \frac{\Delta t}{\Delta x} \right] \end{aligned} \quad (3.20)$$

- (3) Update the dependent variable by

$$u_i^{n+1} = u_i^n + \delta u_i \quad (3.21)$$

$$\delta u_i = (\delta u_i)_B + (\delta u_i)_C \quad (3.22)$$

where both  $(\delta u_i)_B$  and  $(\delta u_i)_C$  are known from step 2.

- (4) Apply appropriate boundary conditions at the inlet and exit.  
 (5) Continue the iteration procedure until the solution converges.

### 3.3 Basic Lax-Wendroff Integration Scheme (Two-Dimensional Euler Equations)

The basic integration procedure outlined for the one dimensional model equation in the previous section can be extended and applied to the linearized two-dimensional Euler equations on a non-orthogonal, curvilinear grid (see Fig. 3.2 for nomenclature).

As in the development of the integration scheme for the one dimensional model equation, the following five steps are performed during each iteration of the numerical algorithm. For example, at each control volume, say  $C$ , the process is:

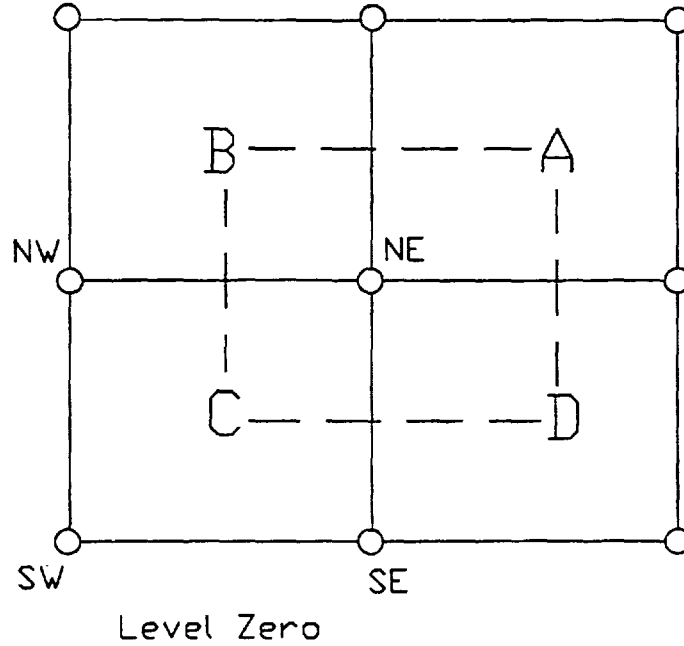


Figure 3.2: Nomenclature used in the description of the computational cells

(1) Sweep through all cells computing the change in each cell using

$$\begin{aligned}
 \Delta u_C + j\omega\Delta t \bar{u}_C = & \frac{\Delta t}{\Delta V} \left\{ \left[ \frac{F'_{sw} + F'_{nw}}{2} (\eta_{nw} - \eta_{sw}) - \frac{G'_{sw} + G'_{nw}}{2} (\xi_{nw} - \xi_{sw}) \right] \right. \\
 & - \left[ \frac{F'_{ne} + F'_{se}}{2} (\eta_{ne} - \eta_{se}) - \frac{G'_{ne} + G'_{se}}{2} (\xi_{ne} - \xi_{se}) \right] \\
 & - \left[ \frac{F'_{sw} + F'_{se}}{2} (\eta_{se} - \eta_{sw}) - \frac{G'_{sw} + G'_{se}}{2} (\xi_{se} - \xi_{sw}) \right] \\
 & \left. + \left[ \frac{F'_{nw} + F'_{ne}}{2} (\eta_{ne} - \eta_{nw}) - \frac{G'_{nw} + G'_{ne}}{2} (\xi_{ne} - \xi_{nw}) \right] \right\} \quad (3.23)
 \end{aligned}$$

where

$$\Delta V = \frac{1}{2} [(\xi_{se} - \xi_{nw})(\eta_{ne} - \eta_{sw}) - (\xi_{ne} - \xi_{sw})(\eta_{se} - \eta_{nw})] \quad (3.24)$$

(2) Determine the corrections to the four corner nodes through the use of the distribution formulae

$$(\delta u_{sw})_C = \frac{1}{4} \left[ \Delta u_C - \Delta f_C - \Delta g_C - \frac{j\omega\Delta t}{2} \Delta u_C \right]$$

$$(\delta u_{nw})_C = \frac{1}{4} \left[ \Delta u_C - \Delta f_C + \Delta g_C - \frac{j\omega\Delta t}{2} \Delta u_C \right]$$

$$(\delta u_{ne})_C = \frac{1}{4} \left[ \Delta u_C + \Delta f_C + \Delta g_C - \frac{j\omega\Delta t}{2} \Delta u_C \right]$$

$$(\delta u_{se})_C = \frac{1}{4} \left[ \Delta u_C + \Delta f_C - \Delta g_C - \frac{j\omega\Delta t}{2} \Delta u_C \right] \quad (3.25)$$

Again, the following notation has been introduced to simplify the expressions

$$\begin{aligned} \Delta f_C &= \frac{\Delta t}{\Delta V} (\Delta F'_C \Delta \eta^l - \Delta G'_C \Delta \xi^l) \\ \Delta g_C &= \frac{\Delta t}{\Delta V} (\Delta G'_C \Delta \xi^m - \Delta F'_C \Delta \eta^m) \end{aligned} \quad (3.26)$$

where

$$\begin{aligned} \Delta \xi^l &= \frac{1}{2} (\xi_{nw} + \xi_{ne} - \xi_{sw} - \xi_{se}) \\ \Delta \eta^l &= \frac{1}{2} (\eta_{nw} + \eta_{ne} - \eta_{sw} - \eta_{se}) \\ \Delta \xi^m &= \frac{1}{2} (\xi_{ne} + \xi_{se} - \xi_{sw} - \xi_{nw}) \\ \Delta \eta^m &= \frac{1}{2} (\eta_{ne} + \eta_{se} - \eta_{sw} - \eta_{nw}) \end{aligned} \quad (3.27)$$

(3) Update the dependent variable by

$$\begin{aligned} u_i^{n+1} &= u_i^n + \delta u_i \\ \delta u_i &= (\delta u_i)_A + (\delta u_i)_B + (\delta u_i)_C + (\delta u_i)_D \end{aligned} \quad (3.28)$$

where  $(\delta u_i)_A$ ,  $(\delta u_i)_B$ ,  $(\delta u_i)_C$ , and  $(\delta u_i)_D$  known from step 2.

(4) Apply appropriate boundary conditions at the inlet and exit.

(5) Continue iteration procedure until the solution converges.

It should be noted that instead of a single equation (as in the model problem) the Euler equations represent four separate equations. As such, the changes and corrections described in the previous development are now vector quantities described below. First, the changes in conservation variables are

$$\Delta \mathbf{u}' = \begin{bmatrix} (\Delta \rho') \\ (\Delta \rho u') \\ (\Delta \rho v') \\ (\Delta e') \end{bmatrix} \quad (3.29)$$

Now,  $\Delta \mathbf{F}'$  and  $\Delta \mathbf{G}'$  can be obtained by the following expressions,

$$\Delta \mathbf{F}' = \left( \frac{\partial \overline{\mathbf{F}}}{\partial \overline{\mathbf{U}}} \right) \Delta \mathbf{u}' = \begin{bmatrix} \overline{U} (\Delta \rho u') + \overline{U} (\overline{\rho} \Delta u') + \Delta p' \\ \overline{V} (\Delta \rho u') + \overline{U} (\overline{\rho} \Delta v') \\ \overline{h}_o (\Delta \rho u') + \overline{U} (\overline{\rho} \Delta h'_o) \end{bmatrix} \quad (3.30)$$

and

$$\Delta \mathbf{G}' = \left( \frac{\partial \overline{\mathbf{G}}}{\partial \overline{\mathbf{U}}} \right) \Delta \mathbf{u}' = \begin{bmatrix} \overline{U} (\Delta \rho v') + \overline{V} (\overline{\rho} \Delta u') \\ \overline{V} (\Delta \rho v') + \overline{V} (\overline{\rho} \Delta v') + \Delta p' \\ \overline{h}_o (\Delta \rho v') + \overline{V} (\overline{\rho} \Delta h'_o) \end{bmatrix} \quad (3.31)$$

where

$$\begin{aligned}
(\bar{\rho}\Delta u') &= (\Delta\rho u') - \bar{U}(\Delta\rho') \\
(\bar{\rho}\Delta v') &= (\Delta\rho v') - \bar{V}(\Delta\rho') \\
(\Delta p') &= (\gamma - 1) \left[ (\Delta e') - \frac{1}{2} (\bar{U}(\Delta\rho u') + \bar{V}(\Delta\rho v') + \bar{U}(\bar{\rho}\Delta u') + \bar{V}(\bar{\rho}\Delta v')) \right] \\
(\bar{\rho}\Delta h'_o) &= (\Delta e') + (\Delta p') - \bar{h}_o(\Delta p')
\end{aligned} \tag{3.32}$$

The final consideration is the time step,  $\Delta t$ . For speed in convergence, the larger the time step the better, however, the time step must not violate the CFL (Courant, Friedrichs, and Lewy) condition. For the scheme to be stable, the numerical scheme cannot propagate the solution faster than the physical wave speeds. This is the so called CFL condition. To this end, the following criteria is used to determine the maximum allowable time step.

$$\Delta t \leq \min \left( \frac{\Delta V}{|\bar{U}\Delta\eta^l - \bar{V}\Delta\xi^l| + a\Delta l} , \frac{\Delta V}{|\bar{U}\Delta\eta^m - \bar{V}\Delta\xi^m| + a\Delta m} \right) \tag{3.33}$$

where

$$\Delta l = \sqrt{(\Delta\xi^l)^2 + (\Delta\eta^l)^2} , \quad \Delta m = \sqrt{(\Delta\xi^m)^2 + (\Delta\eta^m)^2} \tag{3.34}$$

and  $a$  is the speed of sound.

### 3.4 Smoothing

The numerical equations presented can be applied to obtain solutions to inviscid, rotational (and/or irrotational), subsonic, transonic and supersonic flow problems. However, for subsonic flows a small amount of artificial viscosity must be added to suppress the spurious sawtooth solutions permitted by the numerical solution technique. Furthermore, for transonic and supersonic applications the addition of viscous like terms are needed to stabilize and capture shocks. Although it has been determined that some level of smoothing is imperative, care must be taken so as not to add so much as to diminish the accuracy of the numerical algorithm. In the present analysis, two different smoothing terms have been introduced. The first, used in transonic and supersonic flow regimes, is termed *second difference* smoothing. Although this smoothing is first order accurate it only need be applied in the regions near the shock. The second, used in both subsonic and transonic regimes, is termed *fourth difference* smoothing and is effective at reducing the numerical oscillations introduced. As implemented, the solution procedure with only fourth difference smoothing remains second order accurate.

To illustrate how the smoothing is added to the corrections (previously determined), we again consider the one-dimensional model problem. The correction to the  $i$ th node with smoothing is found to be

$$\delta u_i = (\delta u_i)_B + (\delta u_i)_C + \sigma_2(u_{i+1} - 2u_i + u_{i-1})$$

$$+ \sigma_4 (u_{i-2} - 4u_{i-1} + 6u_i - 4u_{i+1} + u_{i+2}) \quad (3.35)$$

where  $\sigma_2$  and  $\sigma_4$  are coefficients of smoothing indicating the level of second difference and fourth difference smoothing added to the correction. Typically the values range from 0.0 to 0.05 for the fourth difference smoothing coefficient,  $\sigma_4$ , and 0.0 to 0.1 for the second difference smoothing coefficient,  $\sigma_2$ . Equation 3.35 would seem to indicate that the fourth difference smoothing has a difference stencil of five grid points (corresponding to 25 grid points for two-dimensional Euler). As implemented, however, the fourth difference operator can be generated by taking the second difference of the second difference operator. As a result, the difference stencil for the one-dimensional model equation remains 3 grid points (corresponding to 9 grid points for two-dimensional Euler) and hence the smoothing operators can be adapted to the cell based distribution formulas previously developed.

### 3.5 Properties of Ni's Scheme

At this point in the analysis, the analytic problem developed in Chapter 2 has been discretized. The dependent variables are now defined at discrete locations or nodes. Spatial derivatives have been approximated using finite volume techniques resulting in a system of algebraic equations. Thus, the original problem involving a continuous domain and partial differential equations has been transformed into a discrete system of algebraic equations. At this time it is important to determine whether the solution obtained by solving the algebraic system is a good approximation to the original system of PDEs. Among the issues considered in the following sections are consistency and stability.

#### 3.5.1 Accuracy and Consistency

Simply stated, the truncation error of a scheme can be defined as the difference between the partial differential equation and the finite difference approximation to it. In other words,

$$Error_{truncation} = PDE - FDE \quad (3.36)$$

The order of the scheme is a measure of the magnitude of the truncation error. Consistency deals with the extent to which the finite-difference equations approximate the partial differential equations. A finite difference representation of a PDE is said to be consistent if it can be shown that the truncation error vanishes as the mesh is refined.

A formal development of these two concepts will now be presented. Again, it is convenient to illustrate these ideas with a less complicated model equation which resembles the linearized Euler equations in form and behavior. The model equation considered is the one-dimensional wave equation, which when linearized and reintroducing a pseudo time dependence takes the following form

$$u_t + j\omega u + cu_x = 0 \quad (3.37)$$

where the subscripts  $t$  and  $x$  represent differentiation with respect to time and the  $x$ -direction respectively. Note that Eq. 3.37 is identical to Eq. 3.6 when  $c$  is equivalent to the Jacobian ( $\partial F/\partial U$ ). With this in mind, the finite difference expression for this model equation is then

$$\begin{aligned} u_i^{n+1} = & u_i^n - j\alpha \left( \frac{u_{i-1}^n + 2u_i^n + u_{i+1}^n}{4} \right) + \frac{\lambda}{2} \left[ (j\alpha - 1) (u_{i+1}^n - u_{i-1}^n) \right] \\ & + \frac{\lambda^2}{2} (u_{i+1}^n - 2u_i^n + u_{i-1}^n) - \frac{\alpha^2}{2} \left( \frac{u_{i-1}^n + 2u_i^n + u_{i+1}^n}{4} \right) \end{aligned} \quad (3.38)$$

where the following simplifying notation has been introduced

$$\begin{aligned} \alpha &= \omega \Delta t \\ \lambda &= c \frac{\Delta t}{\Delta x} \end{aligned} \quad (3.39)$$

where  $\alpha$  is a reduced frequency based on the time step, and  $\lambda$  is the so-called CFL number. Equation 3.38 is the final finite difference expression for the model equation. Using this equation and Taylor expanding about  $u_i^n$ , (for clarity the subscripts  $i$  and  $n$  are dropped) the following *modified* equation is obtained.

$$\begin{aligned} u_t + j\omega u + cu_x = & u \left[ -j \frac{\omega^2 \lambda^2 \Delta x^2}{6c^2} - \frac{\omega^4 \lambda^3 \Delta x^3}{24c^3} \right] \\ & + u_x \left[ -\frac{\omega^2 \lambda^2 \Delta x^2}{2c} + j \frac{\omega^3 \lambda^3 \Delta x^3}{6c^2} \right] \\ & + u_{xx} \left[ j\omega \left( \frac{\lambda^2 \Delta x^2}{2} - \frac{\Delta x^2}{4} \right) + \frac{\omega^2}{c} \left( \frac{\lambda^3 \Delta x^3}{4} - \frac{\lambda \Delta x^3}{8} \right) \right] \\ & + u_{xxx} \left[ \frac{c \Delta x^2}{6} (\lambda - 1) + j \frac{\omega \Delta x^3}{6} (\lambda - \lambda^3) \right] \\ & + u_{xxxx} \left[ \frac{c \Delta x^3}{24} (\lambda - \lambda^3) - j \frac{\omega \Delta x^4}{48} - \frac{\omega^2 \lambda \Delta x^5}{96c} \right] \end{aligned} \quad (3.40)$$

The modified equation is the partial differential equation which is actually solved when a finite difference method is applied to a PDE. It is important to emphasize that the equation obtained after substitution of the Taylor-series expansion must be used to eliminate the higher-order time derivatives rather than the original PDE. This is due to the fact that a solution of the original PDE does not in general satisfy the difference equation.

Upon examination of Eq. 3.40 it is obvious that the left hand side of the equation is the original model PDE. The right hand side of the equation is known as the truncation error. It is important to note that as the grid is refined the error terms on the right hand side go to zero like  $\Delta x^2$ . As implemented, the scheme is therefore second order accurate in both space and time and hence is consistent. Although this alone is not surprising from previous analyses on the Lax-Wendroff scheme, what is unique about this analysis is that the inclusion of the complex source term ( $j\omega u$ ) which changes the character of the truncation error. Any term with an  $\omega$  dependence

would traditionally not appear in a time domain analysis. As will be shown, these terms not only affect the character of the solution, but have an important influence on the stability of the system.

### 3.5.2 Stability

Lax's equivalence theorem states that given a properly posed initial value problem and a consistent finite-difference approximation to it, stability is the necessary condition for convergence [2]. Convergence means that the solution to the finite-difference equation approaches the true solution to the PDE having the same initial and boundary conditions as the grid is refined. A stable numerical scheme is one for which errors from any source (round-off, truncation, etc.) do not grow as the calculation proceeds from one time step to the next.

To illustrate these ideas, we consider again the difference expression for the one-dimensional model equation (the frequency domain version of the wave equation) given by Eq. 3.38. Two separate stability analyses are performed. The first analysis employs a classic Von-Neumann stability analysis. In this approach the domain is assumed to be infinite, hence no special consideration of the boundaries is taken into account. It will be shown that the modified Ni's scheme, as applied to the model equation, is unconditionally unstable as determined for an infinite computational domain. Next, an analysis is presented which determines the stability of the modified Ni scheme on a finite domain. It will be shown that the finiteness of the computational domain has a stabilizing effect on the system and thus allows for converged solutions to the finite difference equation.

#### Von-Neumann Stability Analysis

Using the previously defined notation, Eq. 3.38 can be written as,

$$\begin{aligned}
 u_i^{n+1} &= u_{i-1}^n \left[ -j\frac{\alpha}{2} \left( \frac{1}{2} + \lambda \right) + \frac{\lambda}{2} (1 + \lambda) - \frac{\alpha^2}{8} \right] \\
 &+ u_i^n \left[ 1 - j\frac{\alpha}{2} - \lambda^2 - \frac{\alpha^2}{4} \right] \\
 &+ u_{i+1}^n \left[ -j\frac{\alpha}{2} \left( \frac{1}{2} - \lambda \right) - \frac{\lambda}{2} (1 + \lambda) - \frac{\alpha^2}{8} \right]
 \end{aligned} \tag{3.41}$$

To perform a Von-Neumann stability analysis, the solution of Eq. 3.41 is assumed to take the form

$$u_i^n = \bar{u}^n e^{jk_m i \Delta x} \tag{3.42}$$

where

$$\begin{aligned}
 u_i^{n+1} &= \bar{u}^{n+1} e^{jk_m i \Delta x} \\
 u_{i-1}^n &= \bar{u}^n e^{jk_m (i-1) \Delta x} \\
 u_{i+1}^n &= \bar{u}^n e^{jk_m (i+1) \Delta x}
 \end{aligned} \tag{3.43}$$

Substitution of Eqs. 3.42 and 3.43 into Eq. 3.41 gives

$$\begin{aligned} \frac{\bar{u}^{n+1}}{\bar{u}^n} = G &= e^{-jk_m \Delta x} \left[ -j \frac{\alpha}{2} \left( \frac{1}{2} + \lambda \right) + \frac{\lambda}{2} (1 + \lambda) - \frac{\alpha^2}{8} \right] \\ &+ \left[ 1 - j \frac{\alpha}{2} - \lambda^2 - \frac{\alpha^2}{4} \right] \\ &+ e^{+jk_m \Delta x} \left[ -j \frac{\alpha}{2} \left( \frac{1}{2} - \lambda \right) - \frac{\lambda}{2} (1 + \lambda) - \frac{\alpha^2}{8} \right] \end{aligned} \quad (3.44)$$

For stability, the magnitude of the amplification factor,  $|G|$ , must be less than or equal to one for all wave numbers,  $k_m$ , at the desired frequency,  $\omega$ . Based on this criteria it would indicate that some restrictions might be placed on  $\Delta t$  and  $\Delta x$  or more generally the *Courant number*,  $\lambda$ , (also known as the CFL number) for the system to be stable.

$$\lambda = c \frac{\Delta t}{\Delta x} \quad (3.45)$$

Figure 3.3 shows that the stability limits of the one-dimensional wave equation in the time domain ( $\omega = 0$ ). As expected, the results show that CFL numbers greater than unity cause instabilities to occur. This agrees with classical analyses of the time domain wave equation [2]. Figure 3.4 demonstrates the effect the  $j\omega u$  source term has on the system's stability. In this example, the reduced frequency,  $k = \alpha/\lambda$ , is 1.0. It is evident that  $|G|$  is greater than one for some wave numbers regardless of the Courant number indicating unconditional instability. However, the influence of the boundary conditions has not been included in this analysis. In a Von-Neumann stability analysis, the implicit assumption is that the computational domain is infinite (or that the computational domain is periodic). In the next section the effects of the boundaries on the system's stability will be investigated.

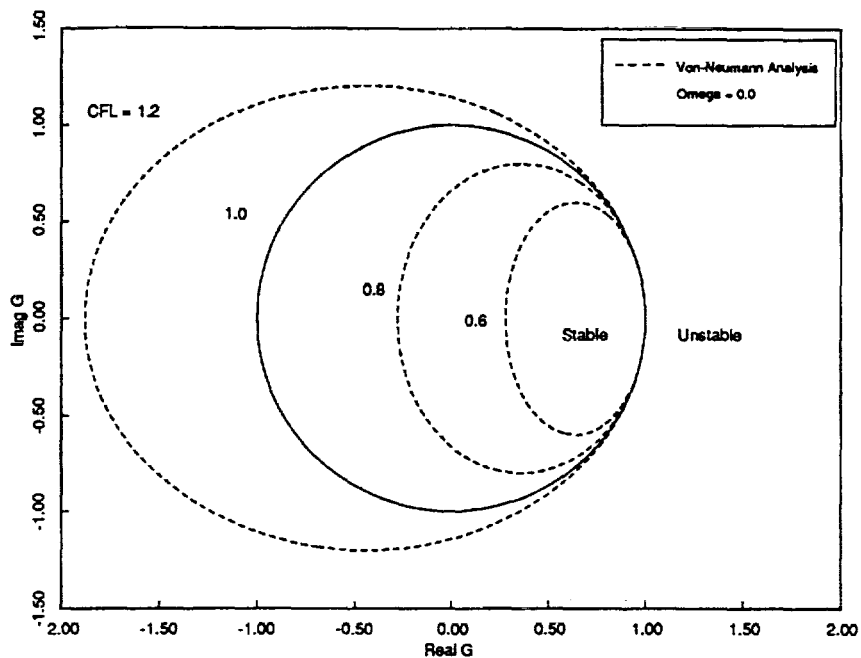


Figure 3.3: Von-Neumann stability analysis, one-dimensional model equation:  $k = 0.0$ ,  $\lambda = 0.6, 0.8, 1.0, 1.2$ .

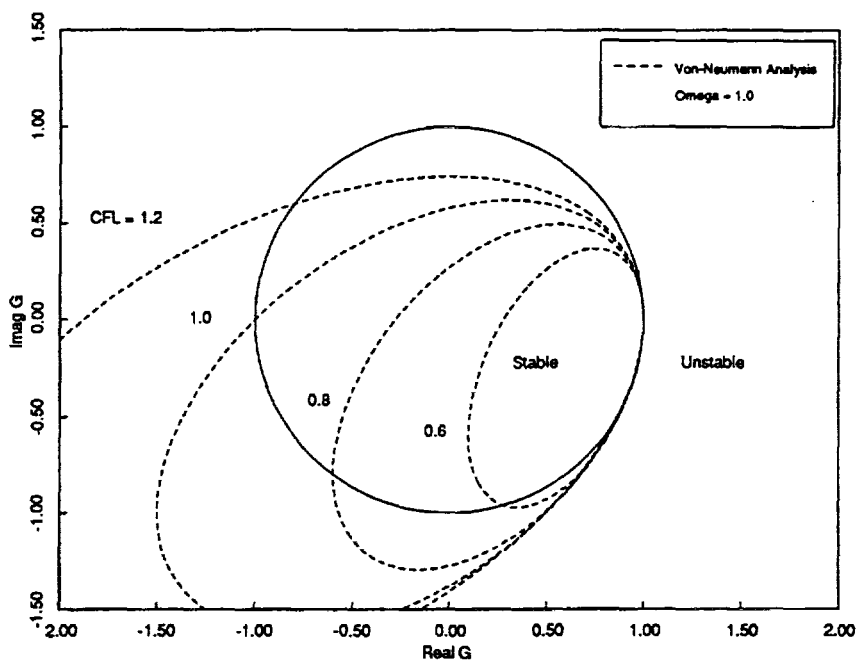


Figure 3.4: Von-Neumann stability analysis, one-dimensional model equation:  $k = 1.0$ ,  $\lambda = 0.6, 0.8, 1.0, 1.2$ .



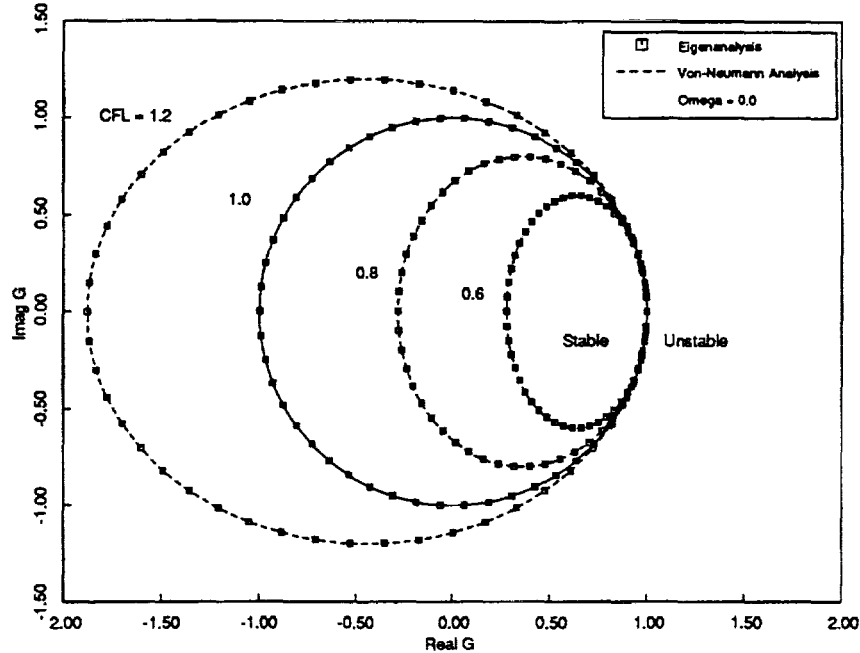


Figure 3.5: Eigenvalue analysis of one-dimensional model equation:  $k = 0.0$ ,  $\lambda = 0.6$ ,  $0.8$ ,  $1.0$ ,  $1.2$  (periodic boundaries)

duct of length 1.0. The frequency based on the duct length was held constant,  $\omega = 5.0$ . The interesting behavior to note here is that the “root locus” determined by the eigenanalysis approaches that of the Von-Neumann analysis as the grid is refined. This is due to the fact that in the limit the domain appears to become *infinite* ( $\Delta x$  approaches zero) and hence more closely models the Von-Neumann analysis.

The numerical algorithm used in the present research has been shown to be both consistent and stable as long as the boundary conditions used in the far field stabilize the long wavelength modes. By virtue of Lax’s equivalence theorem the necessary conditions for convergence have been met.

### 3.5.3 Conservation

The PDE’s of interest in this research all have their basis in physical laws such as the conservation of mass, momentum and energy. Such a PDE represents a conservation statement at a particular point. The criteria necessary for a finite difference scheme to be considered conservative is now discussed. Consider the integral form of the continuity equation for a fixed control volume

$$\int_{cv} \nabla \cdot \rho \mathbf{V} dV = \oint_{cs} \rho \mathbf{V} \cdot \mathbf{n} dS = 0 \quad (3.48)$$

To determine whether the finite-difference representation of the PDE has the conservative property, it must be established that the discretized version of the divergence

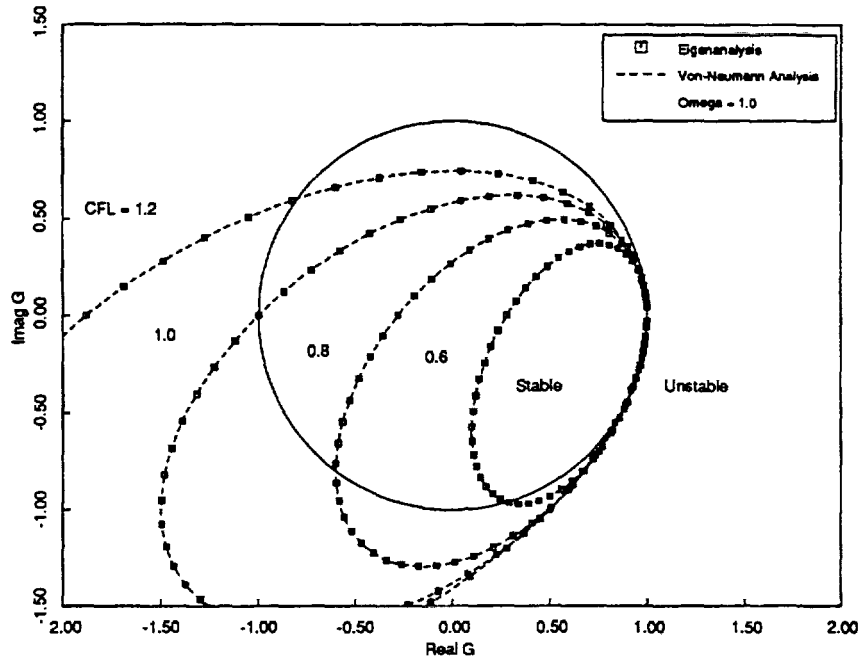


Figure 3.6: Eigenvalue analysis of one-dimensional model equation:  $k = 1.0$ ,  $\lambda = 0.6$ , 0.8, 1.0, 1.2 (periodic boundaries)

theorem is satisfied. To do this the integral on the left is evaluated by summing the finite-difference representation of the PDE at all grid points. If the difference scheme has the conservative property, all terms will cancel except those which represent fluxes at the boundaries. Stated another way, Eq. 3.48 holds regardless of what the control volume is when the analytical equations are modeled computationally; the flow field is governed by the boundary conditions. For this example, it can be determined whether the mass flux in equals the mass flux out. If the scheme did not have the conservative property, the numerical solution might permit the existence of mass sources and sinks [2].

Ni's scheme as implemented in the present research exhibits this telescoping property and is indeed a conservative finite difference representation. This property is necessary if the flow fields to be analyzed have discontinuities such as shock waves or wakes. Chapter 6 investigates this idea further.

## 3.6 Multiple-Grid Accelerator

In an effort to reduce computational time associated with the solution of the linearized Euler equations, one would like to use a coarse grid system. The problem in doing this is the truncation errors described previously have been determined to be proportional to the square of the grid spacing. Hence, to coarsen a grid leads to insufficient accuracy. One way to overcome this problem is to implement the multiple-grid technique [13,37]

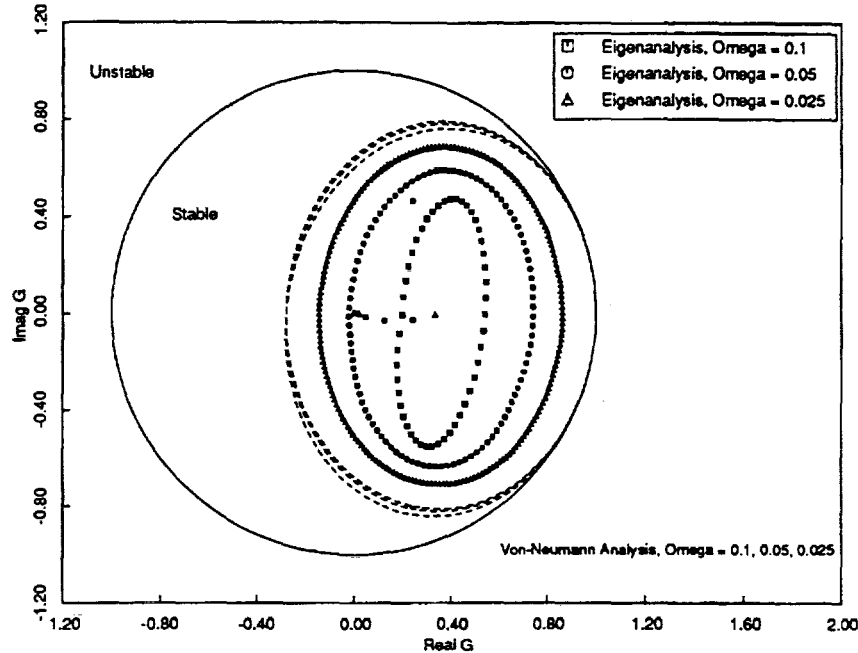


Figure 3.7: Eigenvalue analysis of one-dimensional model equation:  $k = 0.025, 0.05, 0.1$ ,  $\lambda = 0.8$  (nonreflecting boundaries)

where the solution on the fine grid is obtained by cycling the numerical solution procedure between fine and coarser grid systems. The underlying philosophy of the multiple-grid accelerator is to use the coarse grid to propagate the corrections of the fine grid at rates appreciably greater than otherwise possible on the fine grid alone. The result is then to obtain results with accuracy indicative of the finest grid system while obtaining gains in speed of convergence attributable to coarser grid structures without significantly adding to the computational time per iteration.

To implement the technique, a series of coincident grids of varying spatial resolution are required. The finest grid will be designated as the zeroth level grid and successively coarser grids will be designated first, second, etc. level grids. These higher level grids are easily generated by deleting every other node in the grid on the previous level. Figure 3.8 provides a perspective view of three multi-grid levels. Recognizing that the corrections are due to wave movements and the distribution formulae are the systematic tools to propagate these waves, a simple multiple-grid scheme for solving the Euler equations is constructed by combining the basic numerical integration method with the following coarser grid solution procedure.

Instead of the finite volume approximation as given by Eq. 3.23, the change,  $\Delta u^{2h}$ , occurring in the control volumes of the  $2h$  grid are determined by

$$\Delta u^{2h} = T_h^{2h} \delta u^h \quad (3.49)$$

where  $T_h^{2h}$  is an operator which transfers to each control volume of the coarse grid the

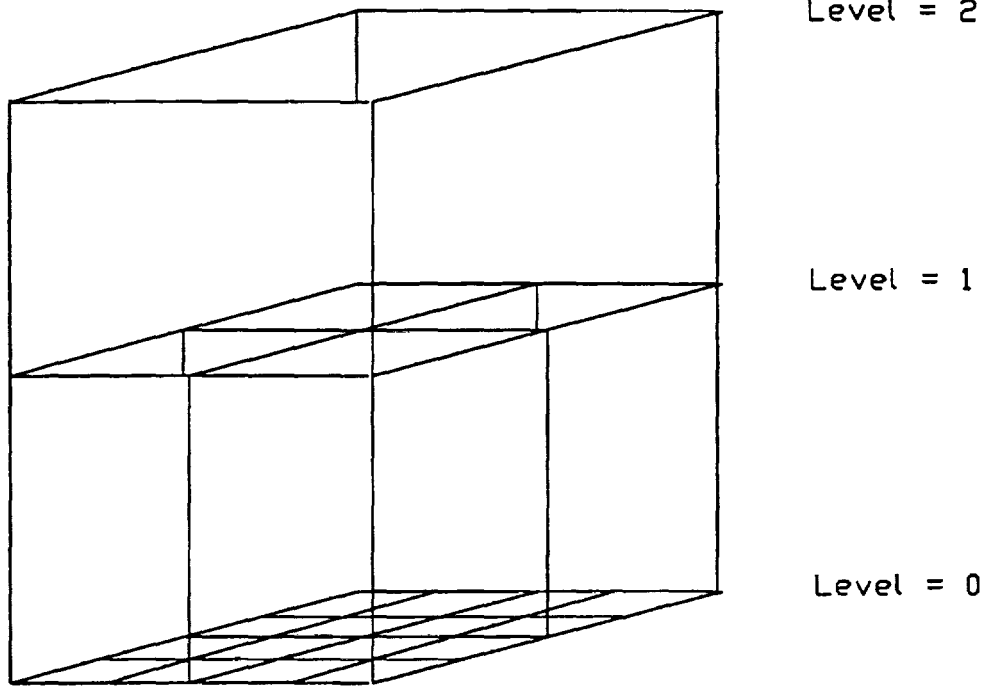


Figure 3.8: Perspective view of multiple grid acceleration levels

correction  $\delta u^h$  of the centered fine grid point, or alternatively a weighted average of the corrections at those fine grid points defining the coarse control volume. Making use of previously developed notation, the generalized distribution formulas

$$\begin{aligned}
 (\delta u_{sw'})_{C'} &= \frac{1}{4} \left[ \Delta u_{C'}^{2h} - \Delta f_{C'}^{2h} - \Delta g_{C'}^{2h} - \frac{j\omega\Delta t}{2} \Delta u_{C'}^{2h} \right] \\
 (\delta u_{nw'})_{C'} &= \frac{1}{4} \left[ \Delta u_{C'}^{2h} - \Delta f_{C'}^{2h} + \Delta g_{C'}^{2h} - \frac{j\omega\Delta t}{2} \Delta u_{C'}^{2h} \right] \\
 (\delta u_{ne'})_{C'} &= \frac{1}{4} \left[ \Delta u_{C'}^{2h} + \Delta f_{C'}^{2h} + \Delta g_{C'}^{2h} - \frac{j\omega\Delta t}{2} \Delta u_{C'}^{2h} \right] \\
 (\delta u_{se'})_{C'} &= \frac{1}{4} \left[ \Delta u_{C'}^{2h} + \Delta f_{C'}^{2h} - \Delta g_{C'}^{2h} - \frac{j\omega\Delta t}{2} \Delta u_{C'}^{2h} \right]
 \end{aligned} \tag{3.50}$$

(where the prime refers to the coarse cell,  $C$ , see Fig 3.2) are then used to propagate the change,  $\Delta u_{C'}^{2h}$ , to the nearby coarse grid points. Next, the corrections of the  $2h$  grid are found by

$$\delta u_{ne'}^{2h} = (\delta u_{sw'})_{A'} + (\delta u_{se'})_{B'} + (\delta u_{ne'})_{C'} + (\delta u_{nw'})_{D'} \tag{3.51}$$

After finding  $\Delta u^{2h}$  on all coarse grid points, the flow properties at the finest grid (level zero) are updated by

$$u^{new} = u + I_{2h}^h \delta u^{2h} \tag{3.52}$$

where  $I_{2h}^h$  is a linear interpolation operator which interpolates the coarse grid corrections to give the corrections at each grid point on the finest mesh.

The above process is repeated on progressively coarser grids until the coarsest grid is reached. The truncation error associated with this process is second-order on the finest grid because the spatial approximation to the governing equation is applied only on the finest mesh. With multiple grid acceleration, the use of coarser grids reduces the computational work required to propagate unsteady disturbances out of the computational domain so that a steady state is rapidly reached. For a detailed description of the multiple grid acceleration technique the reader is referred to [13,37].

### 3.7 Summary

In this chapter, the linearized Lax-Wendroff integration scheme used in the present analysis was developed. Properties of the resulting scheme, such as stability, consistency and accuracy, were also investigated. The basic Lax-Wendroff scheme was found to be second-order accurate and conditionally stable. In the next chapter the treatment of the far-field boundaries is presented.

# Chapter 4

## Far-Field Boundary Conditions

### 4.1 Introduction

Because the computational domain must be finite in extent, so-called far-field boundary conditions must be applied at the inflow and outflow boundaries. These boundary conditions can, if improperly formulated or applied, reflect unsteady disturbances back into the computational domain corrupting the unsteady solution. Furthermore, the better the far-field boundary condition, the closer the inflow and outflow boundaries can be placed to the blade row of interest, thereby reducing the number of grid points and the corresponding computational time.

Nonreflecting boundary conditions have been a recurring topic of investigation in numerical analyses, and for aeroelastic analyses in particular [19]. Previous efforts have focused on matching the analytical behavior of the governing equations in the far-field to the discretized governing equations. Verdon et. al. [49] and Whitehead and Grant [56] matched the known analytical far-field behavior of the linearized potential equation to finite difference and finite element representations of the linearized potential equation on the interior of the domain. Hall and Crawley later applied a similar technique to the linearized Euler equations [24]. Giles has developed approximate boundary conditions for time marching Euler applications [16]. All of these approaches are based on analytical descriptions of the eigenmodes of the governing flow equations.

In this report, we present an alternative nonreflecting boundary condition formulation that is both more general and more accurate than previous boundary conditions based on analytic descriptions of the far field. The exact far-field behavior of the discretized equations themselves is found by solving a numerical eigenvalue problem. The resulting eigenmodes are then used to construct numerically exact, nonreflecting boundary conditions. In addition to being exact, the present formulation has the advantage that it is generic and can be applied to other flow models (such as potential and Navier-Stokes equations) and can be extended to three dimensions.

To aid in the understanding and development of the new numerically exact far-field boundary conditions, three separate far-field boundary conditions are presented. The first two are analytical in nature, i.e., the analytic behavior of the governing equations in the far field is determined and then coupled to the numerical integration scheme.

These approaches provide important insight into the far-field behavior. Finally, the new numerically exact far-field nonreflecting boundary conditions used in the present investigation is presented.

## 4.2 Characteristics Of The Linearized Equations

The following sections present the three different ways of implementing nonreflecting boundary conditions at the inlet and exit of the computational domain.

### 4.2.1 One-Dimensional Characteristics

The easiest nonreflecting boundary conditions to develop and apply are the so-called one-dimensional characteristic boundary conditions. Hence this is an appropriate place to start the development of the far-field boundary treatment. Recall that the grid motion is generated such that grid motion vanishes in the far field. This reduces the governing equations in the far-field to

$$\frac{\partial \mathbf{u}'}{\partial t} + \frac{\partial \mathbf{F}'}{\partial x} + \frac{\partial \mathbf{G}'}{\partial y} = 0 \quad (4.1)$$

If the unsteady disturbances in the far field have large circumferential wavelengths, then the spatial derivative in the circumferential direction may be neglected so that

$$\frac{\partial \mathbf{u}'}{\partial t} + \frac{\partial \mathbf{F}'}{\partial x} = 0 \quad (4.2)$$

It will be beneficial for both the development and the understanding of the far-field behavior to use primitive variables rather than conservation variables in the subsequent analyses. To convert from the conservation variable form used thus far to the primitive variable form, a linear transformation is applied, i.e.,

$$\mathbf{u}'_p = [L]\mathbf{u}' \quad (4.3)$$

where

$$\mathbf{u}'_p = \begin{pmatrix} \rho' \\ u' \\ v' \\ p' \end{pmatrix} \quad (4.4)$$

and

$$[L] = \begin{bmatrix} 1 & 0 & 0 & 0 \\ -\frac{\bar{U}}{\bar{p}} & \frac{1}{\bar{p}} & 0 & 0 \\ -\frac{\bar{V}}{\bar{p}} & 0 & \frac{1}{\bar{p}} & 0 \\ (\gamma-1)\frac{\bar{U}^2 + \bar{V}^2}{2} & -(\gamma-1)\bar{U} & -(\gamma-1)\bar{V} & \gamma-1 \end{bmatrix} \quad (4.5)$$

Rewriting Eq. 4.2 in primitive variable form, and assuming that the steady flow is uniform in the far field gives

$$\frac{\partial \mathbf{u}'_p}{\partial t} + [A]\frac{\partial \mathbf{u}'_p}{\partial x} = 0 \quad (4.6)$$

where  $[A]$  is given by

$$[A] = \begin{bmatrix} \bar{U} & \bar{p} & 0 & 0 \\ 0 & \bar{U} & 0 & \frac{1}{\bar{p}} \\ 0 & 0 & \bar{U} & 0 \\ 0 & \gamma\bar{p} & 0 & \bar{U} \end{bmatrix} \quad (4.7)$$

The behavior of this system of equations (Eq. 4.6) can be determined by an eigenanalysis of the matrix  $[A]$ . One can decouple the equations in Eq. 4.6 by using a similarity transformation. Pre-multiplying the Eq. 4.6 by the matrix of left eigenvectors,  $[T]^{-1}$  gives

$$\frac{\partial \mathbf{W}}{\partial t} + [\Lambda] \frac{\partial \mathbf{W}}{\partial x} = 0 \quad (4.8)$$

The new variables,  $\mathbf{W}$ , in Eq. 4.8 are the so-called characteristic variables given by

$$\mathbf{W} = \begin{pmatrix} w_1 \\ w_2 \\ w_3 \\ w_4 \end{pmatrix} \quad (4.9)$$

which are related to the primitive variables by

$$\mathbf{W} = [T]^{-1} \mathbf{u}'_p \quad (4.10)$$

and

$$\mathbf{u}'_p = [T] \mathbf{W} \quad (4.11)$$

where  $[T]$  is the matrix of right eigenvectors. The diagonal matrix  $[\Lambda]$  can be written as

$$[\Lambda] = [T]^{-1}[A][T] = \begin{bmatrix} \bar{U} - \bar{a} & 0 & 0 & 0 \\ 0 & \bar{U} + \bar{a} & 0 & 0 \\ 0 & 0 & \bar{U} & 0 \\ 0 & 0 & 0 & \bar{U} \end{bmatrix} \quad (4.12)$$

where  $\bar{a}$  is the steady flow speed of sound.

Each of the diagonal entries of  $[\Lambda]$  is the propagation speed of the corresponding characteristic wave. Consider a typical cascade operating in a regime where the axial Mach number is subsonic. There will be three downstream moving waves and one upstream moving wave. The waves have the following physical interpretation. The first characteristic,  $w_1$ , is given by

$$w_1 = u' - \frac{p'}{\rho\bar{a}} \quad (4.13)$$

This corresponds to an upstream moving pressure wave. Likewise, the second characteristic,  $w_2$ , is given by

$$w_2 = u' + \frac{p'}{\rho\bar{a}} \quad (4.14)$$

which corresponds to the downstream moving pressure wave. The third characteristic,  $w_3$ , is found to be an entropy wave having the form

$$w_3 = \rho' - \frac{p'}{a^2} \quad (4.15)$$

Finally, the fourth characteristic,  $w_4$ , represents a vorticity wave as is given by

$$w_4 = v' \quad (4.16)$$

Note that the vorticity and entropy waves convect with the flow, whereas the pressure waves propagate at the convective speed plus or minus the acoustic speed.

Although the nonreflecting far-field boundary conditions based on one-dimensional characteristics can be used in some situations successfully, their effectiveness is limited primarily to cases with low interblade phase angles corresponding to small relative motions of adjacent blades.

## 4.2.2 Two-Dimensional Characteristics

Hall and Crawley [24] extended the above analysis to calculate the analytical behavior in the far field for the two-dimensional Euler equations. As in the one-dimensional approach, the grid motion in the far-field vanishes leaving the familiar unsteady perturbation equation

$$\frac{\partial \mathbf{u}'}{\partial t} + \frac{\partial \mathbf{F}'}{\partial x} + \frac{\partial \mathbf{G}'}{\partial y} = 0 \quad (4.17)$$

Again, it is more convenient to work with the equations in primitive variable form. Furthermore, it is assumed that the steady flow is uniform in the far-field so that Eq. 4.17 becomes

$$\frac{\partial \mathbf{u}'_p}{\partial t} + [A] \frac{\partial \mathbf{u}'_p}{\partial x} + [B] \frac{\partial \mathbf{u}'_p}{\partial y} = 0 \quad (4.18)$$

where  $[A]$  is the matrix which appears in Eq. 4.6 and  $[B]$  is given by

$$[B] = \begin{bmatrix} \bar{V} & 0 & \bar{p} & 0 \\ 0 & \bar{V} & 0 & 0 \\ 0 & 0 & \bar{V} & \frac{1}{\bar{p}} \\ 0 & 0 & \gamma \bar{p} & \bar{V} \end{bmatrix} \quad (4.19)$$

Consider the case where the cascade is vibrating with interblade phase angle,  $\sigma$ , and frequency,  $\omega$ . Since the solution is periodic in the circumferential direction and since the behavior of waves in the far-field is of interest, a more natural representation of the solution in the far field is given by the following Fourier series

$$\mathbf{u}'_p(x, y, t) = \sum_{m=-\infty}^{\infty} \mathbf{u}'_{pm} e^{(j\omega t + jk_m x + j(\sigma + 2\pi m) \frac{x}{C})} \quad (4.20)$$

where  $j = \sqrt{-1}$ ,  $G$  is the blade-to-blade gap, and  $k_m$  is a spatial wave number to be determined later. The coefficients of the Fourier series,  $\mathbf{u}'_{pm}$ , are determined using the Fourier transform given by

$$\mathbf{u}'_{pm} = \frac{1}{G} \int_0^G \mathbf{u}'_p e^{-j(\sigma+2\pi m)\frac{y}{G}} dy \quad (4.21)$$

where the integral in Eq. 4.21 is evaluated numerically using the trapezoidal rule. Substituting Eq. 4.20 into Eq. 4.18 gives

$$\sum_{m=-\infty}^{\infty} (\omega[I] + k_m[A] + \beta_m[B]) \mathbf{u}'_{pm} e^{(j\omega t + jk_m x + j\beta_m y)} = 0 \quad (4.22)$$

where  $[I]$  is the identity matrix and  $\beta_m = (\sigma + 2\pi m)/G$ . In order for Eq. 4.22 to be true, each term in the series must independently vanish such that

$$(\omega[I] + k_m[A] + \beta_m[B]) \mathbf{u}'_{pm} = 0 \quad (4.23)$$

Since  $\omega$  and  $\beta_m$  are prescribed quantities, Eq. 4.23 is an eigenvalue problem for the eigenvalues  $k_m$  and the corresponding eigenvectors  $\mathbf{u}'_m$ .

As in the development of the one-dimensional boundary condition, the right eigenvectors can be assembled into a matrix  $[T]$ . Then the Fourier coefficients,  $\mathbf{u}'_{pm}$ , can again be written in terms of the characteristic variables,  $\mathbf{W}_m$ . The two-dimensional characteristics are given by

$$\mathbf{W}_m = [T]^{-1} \mathbf{u}'_{pm} \quad (4.24)$$

After some manipulation, it can be shown that

$$\begin{pmatrix} w_1 \\ w_2 \\ w_3 \\ w_4 \end{pmatrix} = \begin{bmatrix} 0 & \beta_m \bar{V} + \omega & -\beta_m \bar{U} & -\frac{\sqrt{\beta_m^2 (\bar{U}^2 + \bar{V}^2 - \bar{a}^2) + 2\beta_m \omega \bar{V} + \omega^2}}{\bar{p}\bar{a}} \\ 0 & \beta_m \bar{V} + \omega & -\beta_m \bar{U} & +\frac{\sqrt{\beta_m^2 (\bar{U}^2 + \bar{V}^2 - \bar{a}^2) + 2\beta_m \omega \bar{V} + \omega^2}}{\bar{p}\bar{a}} \\ 1 & 0 & 0 & -\frac{1}{\bar{a}^2} \\ 0 & \beta_m \bar{U} & \beta_m \bar{V} + \omega & \frac{\beta_m}{\bar{p}} \end{bmatrix} \begin{pmatrix} \rho'_m \\ u'_m \\ v'_m \\ p'_m \end{pmatrix} \quad (4.25)$$

The matrix in Eq. 4.25 is a function of the steady flow variables, the excitation frequency  $\omega$ , and the circumferential wave numbers  $\beta_m$ . The resulting axial wave numbers are

$$k_{1m} = \frac{-\bar{U}(\omega + \beta_m \bar{V} + \bar{a}) \sqrt{\beta_m^2 (\bar{U}^2 + \bar{V}^2 - \bar{a}^2) + 2\beta_m \omega \bar{V} + \omega^2}}{\bar{U}^2 - \bar{a}^2} \quad (4.26)$$

$$k_{2m} = \frac{-\bar{U}(\omega + \beta_m \bar{V} - \bar{a} \sqrt{\beta_m^2 (\bar{U}^2 + \bar{V}^2 - \bar{a}^2)} + 2\beta_m \omega \bar{V} + \omega^2}{\bar{U}^2 - \bar{a}^2} \quad (4.27)$$

$$k_{(3,4)m} = -\frac{(\beta_m \bar{V} + \omega)}{\bar{U}} \quad (4.28)$$

As in the one-dimensional boundary conditions of the previous section, these characteristics correspond to upstream and downstream moving pressure waves, an entropy wave, and a vorticity wave. To recover the one-dimensional characteristics, a frequency,  $\omega$ , of 1.0 and circumferential wave number,  $\beta_m$ , of 0.0 can be substituted into Eq. 4.25.

### 4.2.3 Exact Numerical Characteristics

Presented here is a more general method of calculating the characteristic waves for two-dimensional, linearized unsteady flow solvers such as those developed for solving the linearized potential equation and the linearized Euler equations. Consider the linearized Euler equations discretized on an H-grid with  $I$  nodes in the axial direction and  $J$  nodes in the circumferential direction. Even though the solution procedure selected for this research (Chapter 3) uses a pseudo-time-marching technique and is iterative in nature, the converged solution can be thought of as satisfying a large sparse matrix equation of the form

$$\begin{bmatrix} B_1 & C_1 & & & & \\ A_2 & B_2 & C_2 & & & \\ & \ddots & \ddots & \ddots & & \\ & & & A_{I-1} & B_{I-1} & C_{I-1} \\ & & & & A_I & B_I \end{bmatrix} \begin{Bmatrix} \mathbf{u}_1 \\ \mathbf{u}_2 \\ \vdots \\ \mathbf{u}_{I-1} \\ \mathbf{u}_I \end{Bmatrix} = \begin{Bmatrix} \mathbf{b}_1 \\ \mathbf{b}_2 \\ \vdots \\ \mathbf{b}_{I-1} \\ \mathbf{b}_I \end{Bmatrix} \quad (4.29)$$

where  $\mathbf{u}_i$  is the vector of perturbation variables along the  $i^{th}$  axial grid line, and  $\mathbf{b}_i$  is the vector of inhomogeneous terms that arise from, for example, unsteady blade motion. As previously noted in the section detailing the deforming grid, the grid motion vanishes in the far-field. Hence the vectors  $\mathbf{b}_i$  go to zero in the far field. The sub-matrices  $A_i$ ,  $B_i$ , and  $C_i$  are large sparse matrices, each of size  $4J \times 4J$ . The entries in these sub-matrices depend upon the details of the particular finite volume or finite difference scheme used in the unsteady flow solver as well as the steady flow solution. The details of the finite volume scheme were presented in Chapter 3. The result of this approach is that the sub-matrices  $A_i$ ,  $B_i$ , and  $C_i$  are block tridiagonal, with the blocks being  $4 \times 4$  matrices. As previously described, upstream and downstream of the blade row periodic boundary conditions are prescribed to reduce the computational domain to a single passage. Therefore, terms also appear in the upper right and lower left corners of the sub-matrices.

If in the far field the grid spacing in the axial direction is uniform and the *stream line* gridlines are straight and aligned with the steady flow, then the discretized equations are identical from axial station to axial station. The discretized equations at

the  $i^{\text{th}}$  axial station in the far-field can be expressed as

$$[A] \{u_{i-1}\} + [B] \{u_i\} + [C] \{u_{i+1}\} = 0 \quad (4.30)$$

where now the matrices  $[A]$ ,  $[B]$ , and  $[C]$  are independent of  $i$ . Since the equations are identical from station to station, a solution which satisfies the discretized far-field equations at the  $i^{\text{th}}$  station must also satisfy the equations at the  $i + 1^{\text{th}}$  station. This, along with the insight that it is desirable to model the motion of waves in the far-field, suggests that solutions in the far field take on the following form

$$\{u_i\} = \sum_m z_m^i \{\bar{u}_m\} w_m \quad (4.31)$$

where  $u_i$  is the solution at the  $i^{\text{th}}$  station,  $z_m$  is an eigenvalue,  $\bar{u}_m$  is the corresponding eigenvector, and  $w_m$  is a coefficient that indicates how much of each eigenmode is present in the solution. Substitution of Eq. 4.31 into Eq. 4.30 gives

$$\sum_m z_m^{i-1} [[A] + z_m[B] + z_m^2[C]] \{\bar{u}_m\} w_m = 0 \quad (4.32)$$

For the series in Eq. 4.32 to be zero, each term in the series must vanish so that

$$[[A] + z_m[B] + z_m^2[C]] \{\bar{u}_m\} = 0 \quad (4.33)$$

This is recognized as a second order eigenvalue problem for the eigenmodes,  $\{\bar{u}_m\}$ , and the corresponding eigenvalues,  $z_m$ . The eigenvalue problem is put into a more conventional form by recasting Eq. 4.33 in state-space form.

$$\begin{bmatrix} 0 & I \\ -A & -B \end{bmatrix} \begin{Bmatrix} \bar{u}_m \\ z_m \bar{u}_m \end{Bmatrix} = z_m \begin{bmatrix} I & 0 \\ 0 & C \end{bmatrix} \begin{Bmatrix} \bar{u}_m \\ z_m \bar{u}_m \end{Bmatrix} \quad (4.34)$$

Roughly speaking, the eigenmodes of Eq. 4.34 correspond to two-dimensional pressure, entropy, and vorticity waves which can travel up and down the duct. The eigenvalue  $z_m$  is closely related to the axial wave number,  $k_{x_m}$ , of an eigenmode. In particular,

$$z_m^i = \exp [ji (k_{x_m} \Delta x + k_{y_m} \Delta y)] \quad (4.35)$$

or

$$k_{x_m} = \frac{j \ln(z_m)}{\Delta x} - k_{y_m} \frac{\Delta y}{\Delta x} \quad (4.36)$$

where  $\Delta x$  and  $\Delta y$  are the axial and circumferential shifts in the grid from one axial station to the next in the far-field. The matrices  $[A]$ ,  $[B]$ , and  $[C]$  are obtained by careful examination of the iterative linearized Lax-Wendroff solution algorithm. These matrices are actually quadratic functions of the frequency of blade vibration,  $\omega$ . Rewriting Eq. 4.34 in the familiar generalized eigenvalue problem notation allows for a clearer presentation of the ensuing steps. Thus we write that

$$[M]x = z[N]x \quad (4.37)$$

where  $[M]$  and  $[N]$  are general complex matrices and  $z$  and  $\mathbf{x}$  are the eigenvalue and right eigenvector respectively. In the present work EISPACK is used to solve this eigenvalue problem for the desired eigenvalues and eigenmodes.

In figures 4.1 and 4.2 the eigenvalues computed using the present algorithm are compared to the analytical modes predicted using the two-dimensional analytical analysis presented in the previous section. Figure 4.1 shows the eigenvalues of the upstream far-field modes of the Lax-Wendroff scheme for a typical unsteady flow calculation. In this example, the blade-to-blade gap,  $G$ , is 1.0, the inflow Mach number,  $M_\infty$ , is 0.7, the inflow angle,  $\Omega_\infty$ , is  $55^\circ$ , the reduced frequency,  $k$  is 1.287, and the interblade phase angle,  $\sigma$ , is  $-90^\circ$ . The grid spacing between axial stations in the far-field in the  $x$  and  $y$  directions is 0.0601 and 0.0716, respectively. Figure 4.2 also presents the eigenvalues of the continuous linearized Euler equations as they would appear in the computational domain. Note that the eigenvalues of the discretized system agree well with the analytically determined eigenvalues for those eigenvalues near  $z = (1,0)$ . These eigenvalues correspond to longer wavelength (smaller interblade phase angle) modes that are well modeled by the Lax-Wendroff scheme. Computational modes with shorter wavelengths propagate with speeds and decay rates different from their corresponding analytical modes. Finally in Fig. 4.1, note the computational eigenvalues outside the unit circle in the left half-plane. These modes are purely computational with no physical counterparts.

By examining the eigenvalues of Eq. 4.37, one can determine whether the  $m$ th eigenmode is traveling away from or towards the rotor. For the flutter problem, unsteady disturbances are generated by the vibratory motion of the blade row and, therefore, no unsteady waves should travel toward the blade row in the far-field. At the upstream far-field boundary, an eigenmode with eigenvalue  $z_m$  having a magnitude less than unity represents an incoming wave which decays as it progresses towards the blade row and hence should be excluded from the solution (this corresponds to the case where the wave number,  $k_m$ , has a positive imaginary part). Conversely, if the magnitude of the eigenvalue  $z_m$  is greater than unity, then the corresponding eigenmode is an outgoing mode which decays as it propagates away from the blade row and hence should be retained in the solution (this corresponds to the case where the wave number,  $k_m$ , has a negative imaginary part). If the magnitude of the eigenvalue  $z_m$  is unity, corresponding to the imaginary part of  $k_m$  being zero, then additional analysis is required to determine the direction of wave propagation.

In practice, eigenvalues which fall on the unit circle are one of two types: repeated or non-repeated roots. The repeated roots, approximately speaking, correspond to vorticity and entropy modes that convect with the free stream. Since the eigenvalues are repeated, these modes are easily identifiable as rightward moving waves (assuming the flow is left to right) and will be excluded upstream and retained downstream.

The remaining modes to be analyzed have eigenvalues  $z_m$  with magnitude unity and are distinct. These modes correspond to upstream and downstream moving pressure modes that propagate unattenuated. In order to determine the direction of propagation of these eigenmodes one must examine the group velocity. The group

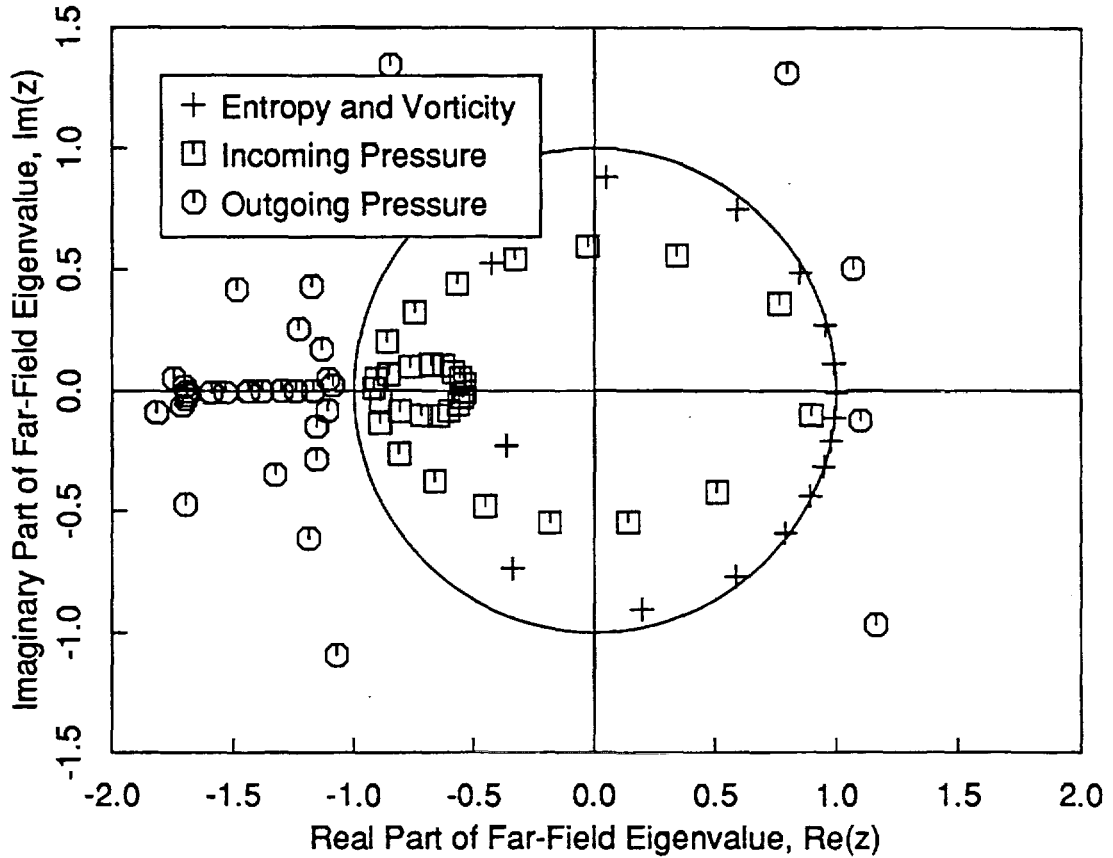


Figure 4.1: Eigenvalues of upstream far-field modes of discretized equations

velocity,  $V_g$ , is given by

$$V_g = -\frac{\partial \omega}{\partial k} = -\frac{1}{\partial k / \partial \omega} \quad (4.38)$$

If the group velocity is positive, there is a net flux in energy to the right (incoming mode upstream, outgoing mode downstream). Conversely, if the group velocity is negative, then the net flux in energy is to the left (outgoing mode upstream, incoming mode downstream).

To determine the group velocity, we first rewrite the eigenvalues as functions of the axial and circumferential wave numbers,

$$z^i = \exp [j (k_x \Delta x_i + k_y \Delta y_i)] \quad (4.39)$$

Next, differentiating Eq. 4.35 with respect to  $\omega$  and rearranging yields

$$\frac{\partial k_x}{\partial \omega} = -j \frac{1}{z \Delta x} \frac{\partial z}{\partial \omega} \quad (4.40)$$

The last piece of information needed to determine the group velocity is  $\partial z / \partial \omega$ . To determine  $\partial z / \partial \omega$ , the following perturbation analysis is performed. Recall Eq. 4.37

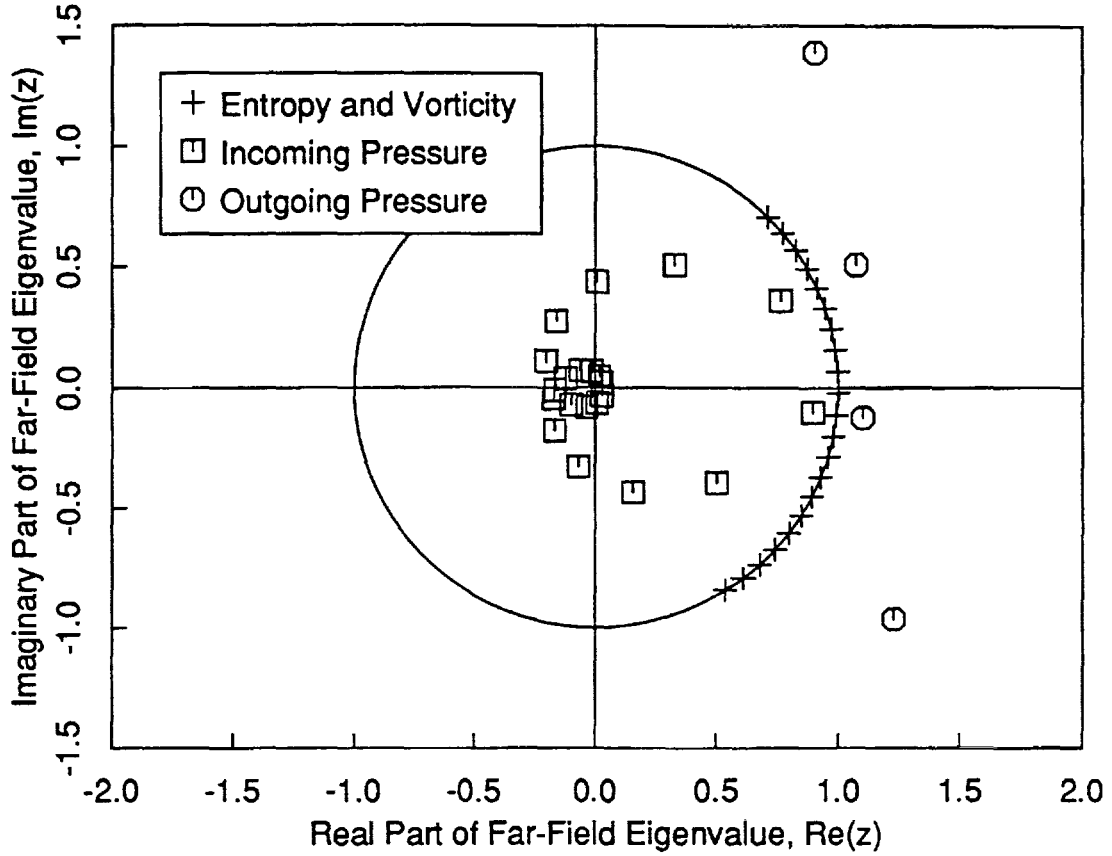


Figure 4.2: Analytically computed eigenvalues of far-field modes

is

$$[M]\mathbf{x} = z[N]\mathbf{x}$$

Consider a perturbation series expansion of Eq. 4.37 about a known solution, i.e.,

$$([M] + [M']) (\mathbf{x} + \mathbf{x}') = (z + z') ([N] + [N']) (\mathbf{x} + \mathbf{x}') \quad (4.41)$$

where the primes indicate a small perturbation. Retaining only the first order terms and multiplying by the left eigenvectors,  $\mathbf{y}^T$ , gives

$$\mathbf{y}^T ([M] - z[N]) \mathbf{x}' + \mathbf{y}^T ([M'] - z[N']) \mathbf{x} = z' \mathbf{y}^T [N] \mathbf{x} \quad (4.42)$$

The first term in Eq. 4.42 is identically zero by definition. The resulting relationship for the perturbation of the eigenvalue,  $z'$ , is

$$z' = \frac{\mathbf{y}^T (M' - zN') \mathbf{x}}{\mathbf{y}^T N \mathbf{x}} \quad (4.43)$$

Therefore, one can infer that

$$\frac{\partial z}{\partial \omega} = \frac{\mathbf{y}^T \left( \frac{\partial M}{\partial \omega} - z \frac{\partial N}{\partial \omega} \right) \mathbf{x}}{\mathbf{y}^T N \mathbf{x}} \quad (4.44)$$

Finally, the group velocity can be written as

$$V_g^{-1} = \frac{+j \mathbf{y}^T \left( \frac{\partial M}{\partial \omega} - z \frac{\partial N}{\partial \omega} \right) \mathbf{x}}{z \Delta x \mathbf{y}^T N \mathbf{x}} \quad (4.45)$$

Hence, once the eigenvalues and the left and right eigenvectors of the individual modes are known, the group velocity and therefore the direction of propagation can be determined as well.

## 4.3 Application of Far-Field Boundary Conditions

Having computed the behavior of characteristic waves in the far field, we now use the characteristics to construct approximate and exact nonreflecting boundary conditions.

### 4.3.1 One-Dimensional Nonreflecting Boundary Conditions

First, we consider the application of the one-dimensional characteristic nonreflecting boundary conditions. As an example, the implementation for an upstream, far-field boundary node is considered. After a Lax-Wendroff iteration has been performed, but before the far-field boundary conditions have been applied, the estimate of the solution of a boundary node is given by

$$\mathbf{u}'_{temp}{}^{n+1} = \mathbf{u}'^n + \delta \mathbf{u}^n \quad (4.46)$$

Using Eq. 4.3, the solution vector in conservation form can be transformed into primitive variable form such that

$$\mathbf{u}'_{p_{temp}}{}^{n+1} = [L] \mathbf{u}'_{temp}{}^{n+1} \quad (4.47)$$

In general,  $\mathbf{u}'_{p_{temp}}{}^{n+1}$  contains both incoming and outgoing waves. The amount of each of these waves is found by Eq. 4.10. With the characteristics now known, the waves determined to be entering the domain are zeroed since these waves could only be the result of a reflection at the far-field boundary. In subsonic flow, for example, the upstream boundary would have three characteristics entering the domain (one pressure, one vorticity, one entropy) which must be eliminated and one outgoing characteristic (pressure) that is left unchanged. This is accomplished as follows:

$$\mathbf{W}_{new}{}^{n+1} = [\hat{\Lambda}] [T]^{-1} \mathbf{u}'_{p_{temp}}{}^{n+1} \quad (4.48)$$

so that

$$\mathbf{u}'_p{}^{n+1} = [T] [\hat{\Lambda}] [T]^{-1} \mathbf{u}'_{p_{temp}}{}^{n+1} \quad (4.49)$$

where  $[\hat{\Lambda}]$  is a diagonal matrix with ones in the entries corresponding to outgoing waves and zeroes in the entries corresponding to incoming waves. Finally, to convert the solution back into conservation variable form

$$\mathbf{u}'^{n+1} = [M]^{-1} \mathbf{u}'_{p_{temp}}{}^{n+1} \quad (4.50)$$

or

$$\mathbf{u}'^{n+1} = [L]^{-1}[T][\hat{\Lambda}][T]^{-1}[L]\mathbf{u}'_{p_{temp}}^{n+1} \quad (4.51)$$

Downstream, the same procedure is followed except that now three characteristics are outgoing and must be retained and only one characteristic is incoming and need be deleted.

Note that the one-dimensional characteristic nonreflecting boundary conditions are approximate; these boundary conditions are most effective when applied to long circumferential wavelength (low interblade phase angle) disturbances.

### 4.3.2 Two-Dimensional Nonreflecting Boundary Conditions

After application of each Lax-Wendroff iteration, but before the far-field boundary conditions have been applied, the estimate of the solution on (for example) the inflow boundary is updated using Eq. 4.46. Again, the solution  $\mathbf{u}'_{p_{temp}}^{n+1}$  will contain a contribution of incoming and outgoing modes. To apply the two-dimensional characteristic boundary conditions, we must first determine the components of each Fourier mode using Eq. 4.21. Having computed the Fourier modes, two-dimensional characteristic nonreflecting boundary conditions are applied as follows:

$$\mathbf{u}'_{p_m}{}^{n+1} = [T][\hat{\Lambda}][T]^{-1}\mathbf{u}'_{p_{temp}}{}^{n+1} \quad (4.52)$$

where again,  $[\hat{\Lambda}]$  is a diagonal matrix of zeroes and ones which eliminate incoming modes and  $[T_m]$  the matrix of right eigenvectors.

Once the characteristic two-dimensional boundary conditions have been applied to all of the Fourier modes, the modified modes are summed together using Eq. 4.20 to obtain the solution in primitive variable form on the far-field boundary. Finally, to obtain the updated solution in conservation form, the following equation is applied at every boundary node, i.e.

$$\mathbf{u}'_m{}^{n+1} = [L]^{-1}\mathbf{u}'_{p_m}{}^{n+1} \quad (4.53)$$

As a final note, in practice a finite number of Fourier modes are used (typically  $m = -2, -1, 0, +1, +2$ ). The remaining modes are not used to update the solution on the boundary.

If the steady flow is uniform in the far field, then the boundary conditions described above are analytically exact. However, if the steady flow is nonuniform, then they are approximate. Also because the numerical characteristic waves differ somewhat from the analytical characteristics due to truncation error, some small reflections will occur for grids with finite resolution. Finally, it is difficult to extend the two-dimensional characteristic nonreflecting boundary conditions to three dimensions due to the difficulty in obtaining analytic descriptions of three-dimensional characteristic waves if the mean flow contains swirl. For these reasons, a more general numerically exact was developed and is presented in the next section.

### 4.3.3 Numerically Exact Nonreflecting Boundary Conditions

In this section, we apply the numerically exact nonreflecting boundary conditions developed in section 4.2.3. Consider the solution along two neighboring grid lines in the upstream far-field region (stations  $i$  and  $i + 1$ ). Together, the solution at these two grid lines can be thought of as the state of the solution at the  $i^{\text{th}}$  grid line. In general, this solution will contain components of all the eigenmodes, incoming and outgoing. The state vector can be expressed in terms of the characteristic variables,  $\mathbf{W}$ , as

$$\begin{Bmatrix} \mathbf{u}'_i \\ \mathbf{u}'_{i+1} \end{Bmatrix} = [E][\Lambda]^i \mathbf{W} \quad (4.54)$$

where  $[E]$  is the matrix of eigenvectors found by solving Eq. 4.37 and  $[\Lambda]$  is the diagonal matrix of eigenvalues. Therefore the state vector at the inflow boundary is related to the state vector at the second axial grid line by the matrix

$$\begin{Bmatrix} \mathbf{u}'_1 \\ \mathbf{u}'_2 \end{Bmatrix} = [E][\Lambda]^{-1}[E]^{-1} \begin{Bmatrix} \mathbf{u}'_2 \\ \mathbf{u}'_3 \end{Bmatrix} = \begin{bmatrix} T_{11} & T_{12} \\ T_{21} & T_{22} \end{bmatrix} \begin{Bmatrix} \mathbf{u}'_2 \\ \mathbf{u}'_3 \end{Bmatrix} \quad (4.55)$$

where  $[T]$  is a transition matrix. The solution at the upstream boundary is then related to the solution on the interior by

$$\{\mathbf{u}'_1\} = \begin{bmatrix} T_{11} & T_{12} \end{bmatrix} \begin{Bmatrix} \mathbf{u}'_2 \\ \mathbf{u}'_3 \end{Bmatrix} \quad (4.56)$$

Finally, for gust response problems Eq. 4.56 becomes

$$\{\mathbf{u}'_1\} = \{\mathbf{u}'_{gust}\} + \begin{bmatrix} T_{11} & T_{12} \end{bmatrix} \begin{Bmatrix} \mathbf{u}'_2 \\ \mathbf{u}'_3 \end{Bmatrix} \quad (4.57)$$

where  $\{\mathbf{u}'_{gust}\}$  is a vector composed of the desired incoming eigenmodes.

The goal is to eliminate incoming waves from the solution. Hence after each basic Lax-Wendroff iteration, the solution at the upstream boundary is found using Eq. 4.56 (for flutter calculations). The matrices  $T_{11}$  and  $T_{12}$ , however, are constructed first by setting the entries of  $[\Lambda]$  to zero that correspond to incoming modes before applying Eq. 4.55. This has the effect of eliminating the incoming characteristics from the solution at the inflow boundary. Note that the matrices  $T_{11}$  and  $T_{12}$  need to be computed just once before the start of the Lax-Wendroff iteration procedure. At each iteration, the far-field nonreflecting boundary conditions require only a relatively small matrix/vector multiply.

## 4.4 Summary

In this chapter, three separate far-field analyses were presented culminating with the development of a new, numerically exact nonreflecting boundary condition which eliminates all reflections. Furthermore, although these boundary conditions were developed for the two-dimensional linearized Euler analysis, the technique is generic and

can be applied to other flow models (e.g., the potential, and Navier-Stokes equations) and can be to three-dimensional flows. In the next chapter, this far-field treatment, along with the basic numerical integration scheme presented in Chapter 3, will be used to investigate unsteady subsonic flows in compressors.

# Chapter 5

## Results

This chapter presents results calculated using the present linearized Euler method. The cases selected show the ability of the present linearized Euler analysis to compute accurately and efficiently the unsteady aerodynamic response of cascade blade rows due to incident gusts as well as blade vibrations. The results obtained with the present analysis are compared with those determined using previously developed semi-analytical, numerical, and experimental methods.

### 5.1 Flat Plate

To validate the method, a number of unsteady flows about a cascade of flat plate airfoils are computed. The results are compared with those obtained using Whitehead's LINSUB code [55], which is based on Smith's compressible flat plate theory [43]. For all the cases considered in this section, the mean flow through the cascade is uniform with a Mach number,  $M$ , of 0.7. The stagger angle,  $\Theta$ , is  $45^\circ$ , and the gap-to-chord ratio,  $G$ , is 1.0.

To begin, consider the case of an inlet distortion interacting with the flat plate cascade. In the nonrotating reference frame, the flow is axial and steady with constant total enthalpy. The axial velocity has a sinusoidally varying deficit with a circumferential wavelength of two blade gaps resulting in an interblade phase angle,  $\sigma$ , of  $-180^\circ$ . In the rotating cascade frame of reference, the airfoils see an unsteady gust with reduced frequency,  $k$ , (based on chord,  $c$  and upstream velocity,  $V_T$ ) of 2.221. Under these conditions the flow is superresonant, i.e., pressure waves with an interblade phase angle,  $\sigma$ , of  $+180^\circ$  propagate in the far field. Any reflection of these pressure waves off the far-field boundaries would cause an unattenuated wave to propagate back into the computational domain, corrupting the solution. Therefore, this case provides a good test of the nonreflecting boundary conditions. Figure 5.1 shows the computed real and imaginary parts of the unsteady pressure difference across the surface of the reference airfoil. The linearized Euler results shown were computed on a  $65 \times 17$  node grid and a  $129 \times 33$  node grid. For comparison, Fig. 5.1 also shows the essentially exact solution calculated using LINSUB. The linearized Euler solution agrees very well with the exact solution, especially for the solution computed on the

129  $\times$  33 node grid. This good agreement demonstrates the effectiveness of the numerically exact nonreflecting boundary conditions. Also note that the present linearized method accurately predicts the square root singularity of the exact solution at the leading edge.

In addition to the gust response problem, one would need to calculate the aerodynamic damping to complete the aerodynamic formulation of the forced response problem. This can be accomplished by solving the blade motion problem. Consider the case where the cascade of airfoils is plunging with an interblade phase angle,  $\sigma$ , of  $-180^\circ$ , and a reduced frequency,  $k$ , of 2.221. Figure 5.2 shows that the linearized Euler analysis is in good agreement with the exact solution for this superresonant, moderate reduced frequency case. Although for the present aerodynamic damping analysis the computational grid deforms continuously with the specified motion of the airfoils, the effectiveness of the moving grid is not readily apparent since the mean flow is uniform and hence the error causing extrapolation terms do not appear in the airfoil boundary conditions.

The last flat plate example considered is a cascade of airfoils subjected to an inlet distortion with an interblade phase angle,  $\sigma$ , of  $270^\circ$ , and a reduced frequency,  $k$ , of 3.332. This corresponds to a superresonant distortion with a wavelength 1.333 times the blade-to-blade gap. Figure 5.3 shows the computed real and imaginary parts of the unsteady pressure difference across the surface of the reference airfoil. The agreement for this case is not as good for the previous two cases although the solution clearly approaches the analytical solution as the grid resolution is increased. It appears from these results that the scheme as currently implemented gives second-order accurate solutions. For example, one observes that doubling the grid resolution reduces the error by approximately a factor of four. Also, the errors are more pronounced at high reduced frequencies. This can be attributed to the fact that at higher reduced frequencies more resolution is required to resolve the short wavelength modes.

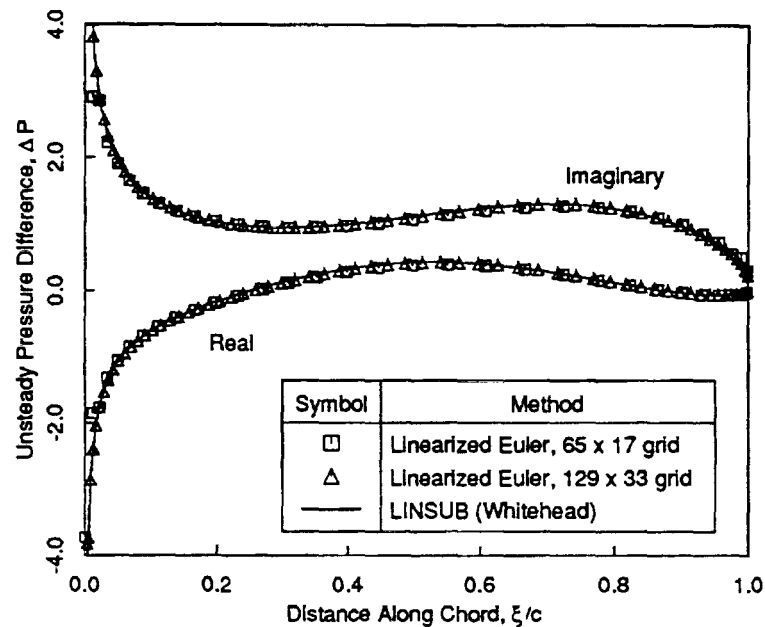


Figure 5.1: Unsteady pressure difference for flat plate cascade subjected to an incident vortical gust:  $k = 2.221$ ,  $\sigma = -180^\circ$

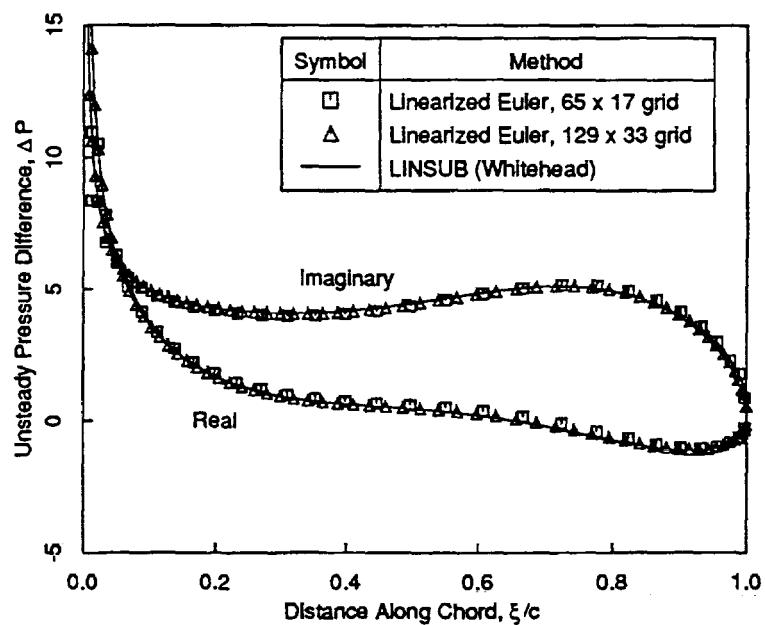


Figure 5.2: Unsteady pressure difference for flat plate cascade undergoing an unsteady plunging motion:  $k = 2.221$ ,  $\sigma = -180^\circ$

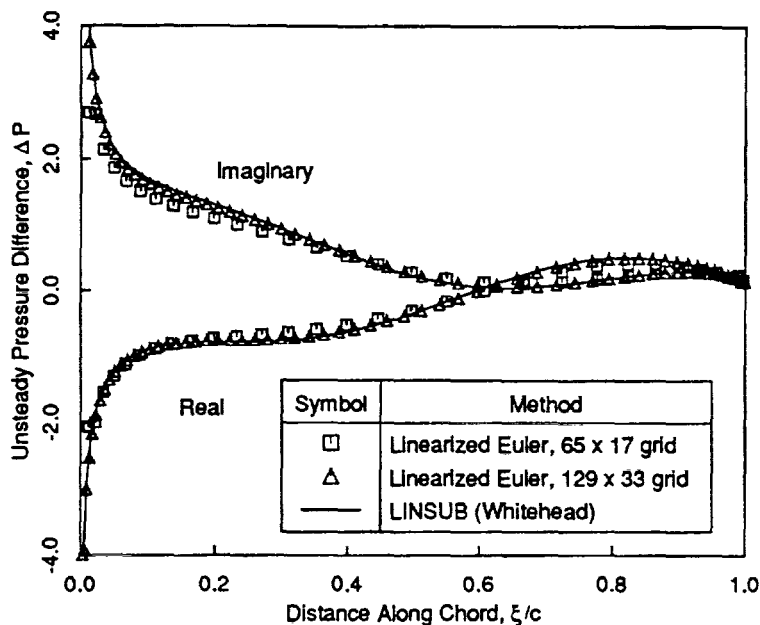


Figure 5.3: Unsteady pressure difference for flat plate cascade subjected to an incident vortical gust:  $k = 3.332$ ,  $\sigma = 270^\circ$

## 5.2 Tenth Standard Configuration

Having demonstrated the accuracy of the method for a flat plate geometry, we now consider the unsteady flow in a more realistic compressor geometry. The purpose of these test cases is to demonstrate the ability of the present method to compute accurately the unsteady flows over loaded airfoils. In addition, the efficiency of the method, and the effectiveness of the far-field boundary conditions will be examined.

The geometry considered in this section is a cascade of cambered airfoils with a slightly modified NACA 0006 thickness distribution. The airfoil has a circular arc camber distribution with a maximum height of 5 percent of the chord. The cascade has a stagger angle,  $\Theta$ , of  $45^\circ$  and a gap-to-chord ratio,  $G$ , of 1.0. The mean inflow angle,  $\Omega_\infty$ , is  $55^\circ$  and the inflow Mach number,  $M_\infty$ , is 0.7. Two computational grids were used for this example: a  $65 \times 17$  and a  $129 \times 33$  node grid. Figure 5.4 shows the mean flow surface pressure distribution calculated using the present steady, nonlinear Euler solver. These results agree well with the surface pressure distribution computed using another steady Euler solver developed by Huff [31]. Note that the maximum Mach number,  $M$ , on the suction surface is about 0.92.

Having computed the steady flow through the blade row, the unsteady flow due to an inlet distortion in the nonrotating frame of reference is computed. For this example, the interblade phase angle,  $\sigma$ , is  $-90^\circ$  and the reduced frequency,  $k$ , is 1.287 corresponding to a disturbance with a wavelength in the circumferential direction of four blade-to-blade gaps. In the stationary frame of reference the total enthalpy is

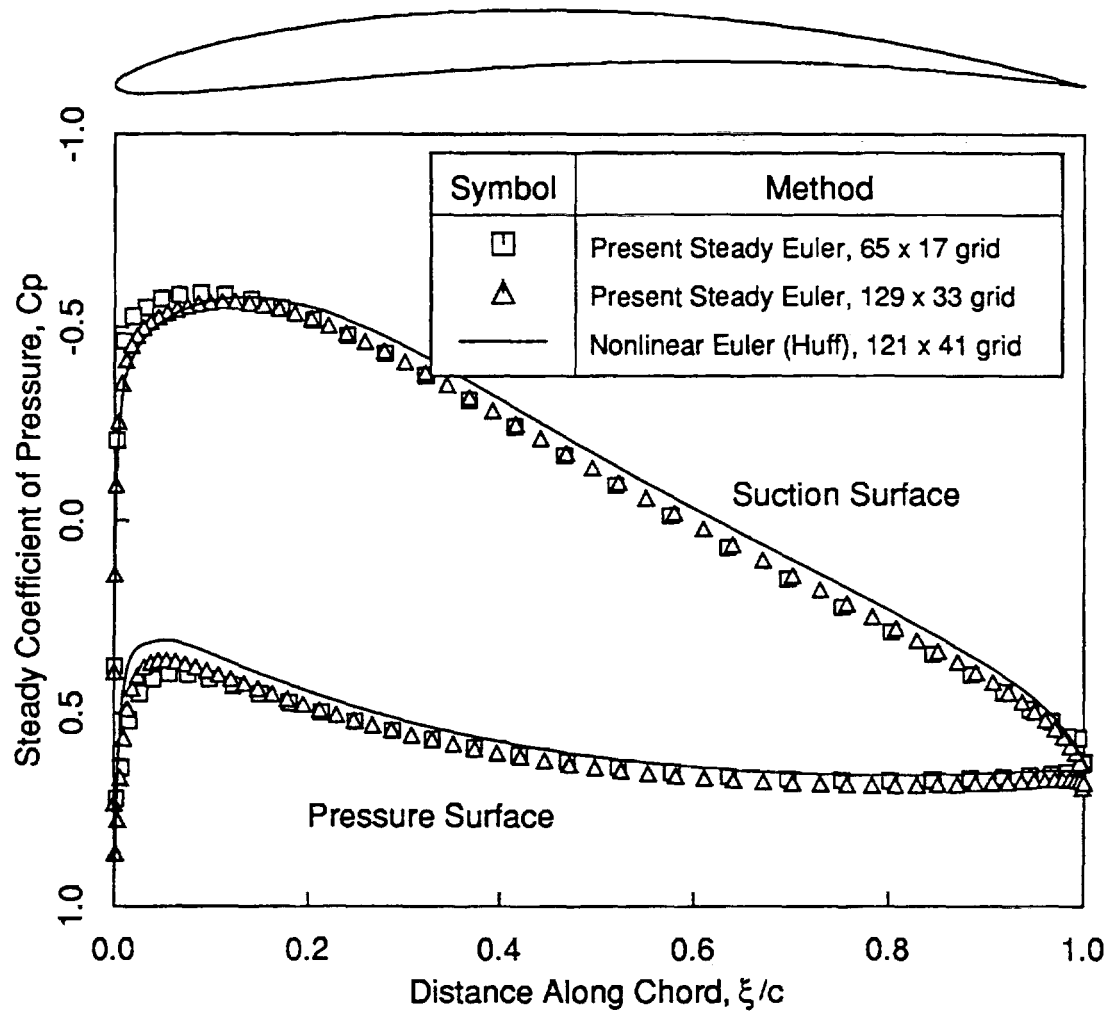


Figure 5.4: Steady coefficient of pressure distribution, Tenth Standard Configuration:  $M_\infty = 0.7$ ,  $G = 1.0$ ,  $\Theta_\infty = 45^\circ$ ,  $\Omega_\infty = 55^\circ$

constant. Figure 5.5 shows the calculated unsteady surface pressure distribution. The good agreement between the  $65 \times 17$  and  $129 \times 33$  node grid solutions indicates that the fine grid solution is nearly grid converged, i.e., the solution will not change with increased grid resolution. Note that the solution is now well behaved in the vicinity of the leading edge; the singularity is removed by the finite radius leading edge. Also shown is the solution computed using a linearized potential code (LINFLO) [26]. The overall agreement with LINFLO is good, although there is a slight discrepancy in the real part of the solution on the suction surface.

Next, we consider a plunging motion of the compressor blades. For the first example, the blades vibrate with an interblade phase angle,  $\sigma$ , of  $-90^\circ$ , and a reduced frequency,  $k$ , of 1.287. Figure 5.6 shows the unsteady pressure distribution on the surface of the reference airfoil found using the present linearized Euler analysis. The figure also includes the results of the nonlinear time marching Euler analysis of Huff. Figure 5.6 shows that the two analyses are in excellent agreement. Note that the solutions are well behaved around the leading and trailing edges, regions that are difficult to resolve accurately using fixed-grid methods. These results clearly demonstrate the effectiveness of the deforming grid method for resolving unsteady flow features in regions of large mean flow gradients, even using moderate resolution grids.

Also shown in Fig. 5.6 are linearized Euler solutions calculated on fixed (i.e., nondeforming) computational grids. For these solutions, extrapolation terms which depend on mean flow gradients must be added to the airfoil boundary conditions and to the expression for the unsteady surface pressure to account for the fact that the airfoil vibrates through the stationary grid. Large errors are seen in the solutions computed on the fixed grid, especially around the leading and trailing edges. These errors are inevitable when using a fixed grid due to the difficulty in evaluating the gradient of the mean flow field near the airfoil surface.

Finally, we consider a moderately high reduced frequency blade motion case to demonstrate the current limitations of the method. For this case, the airfoils plunge with an interblade phase angle,  $\sigma$ , of  $-180^\circ$ , and a reduced frequency,  $k$ , of 2.573. Figure 5.7 shows the computed unsteady surface pressure distribution. Also shown for comparison are the results of a linearized potential analysis [21] and a time marching Euler calculation. The potential solution, which was computed on an extremely fine grid ( $200 \times 50$  nodes), is grid converged. The fine grid linearized Euler calculation is in very good agreement with the potential calculation. The coarse grid linearized Euler calculation, on the other hand, differs significantly from the potential solution on the suction surface. This is to be expected since on the suction surface, where the Mach number is large, upstream travelling pressure disturbances have very short wavelengths that are difficult to resolve. Of course, adequate grid resolution is essential for both nonlinear and linearized analyses.

Figure 5.8 shows the computed unsteady pressure contours for this blade motion case. Of particular interest is the behavior of the solution in the far-field region. For this example, the flow is superresonant upstream and subresonant downstream. In both the upstream and downstream far-field regions, the pressure contours are seen to pass smoothly out of the domain without reflection demonstrating the effectiveness of the far-field nonreflecting boundary conditions.

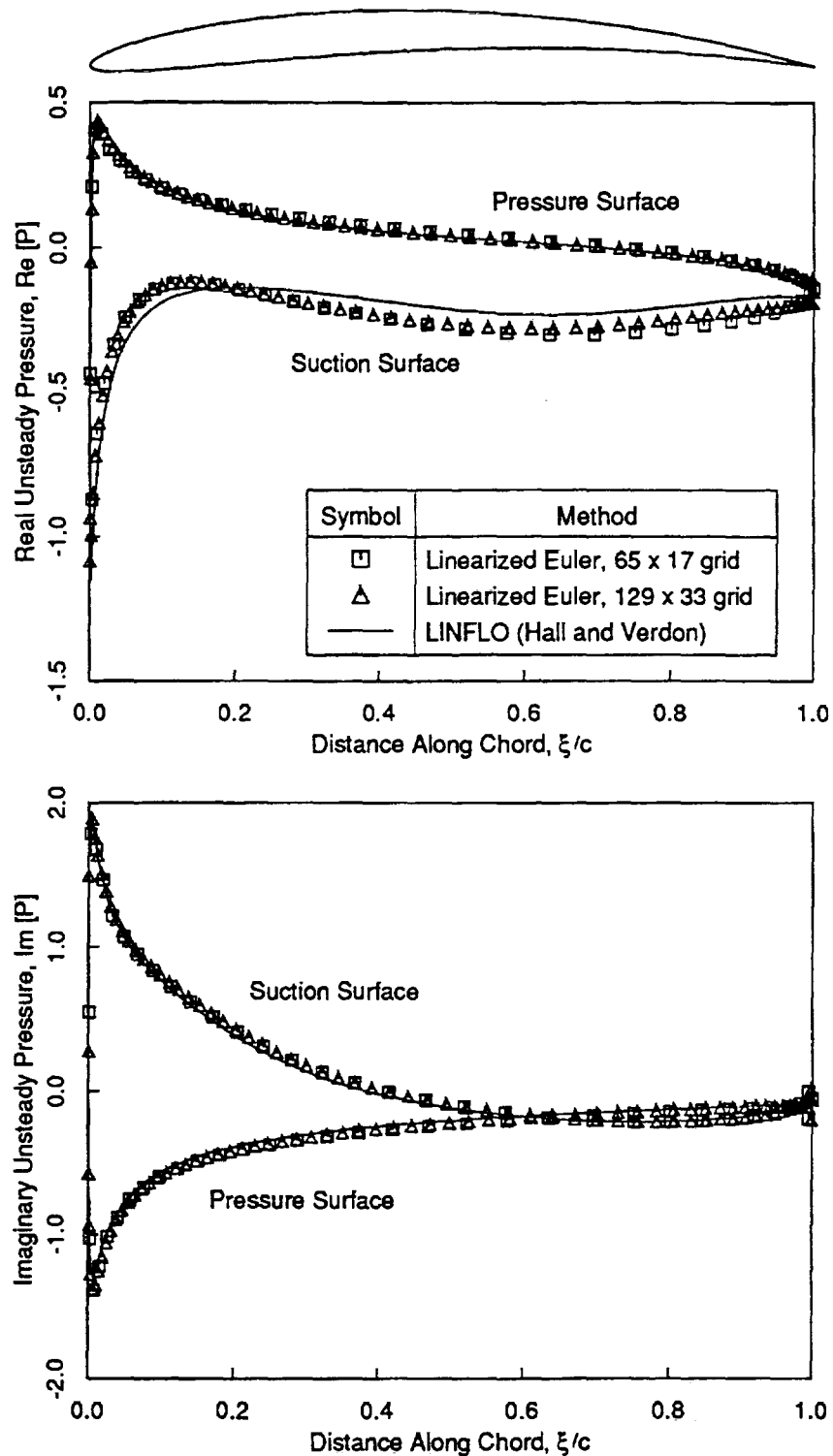


Figure 5.5: (top) Real unsteady pressure distribution for cascade of Tenth Standard Configuration airfoils subjected to an inlet vortical gust; (bottom) Imaginary unsteady pressure distribution for cascade of Tenth Standard Configuration airfoils subjected to an inlet vortical gust:  $k = 1.287$ ,  $\sigma = -90^\circ$

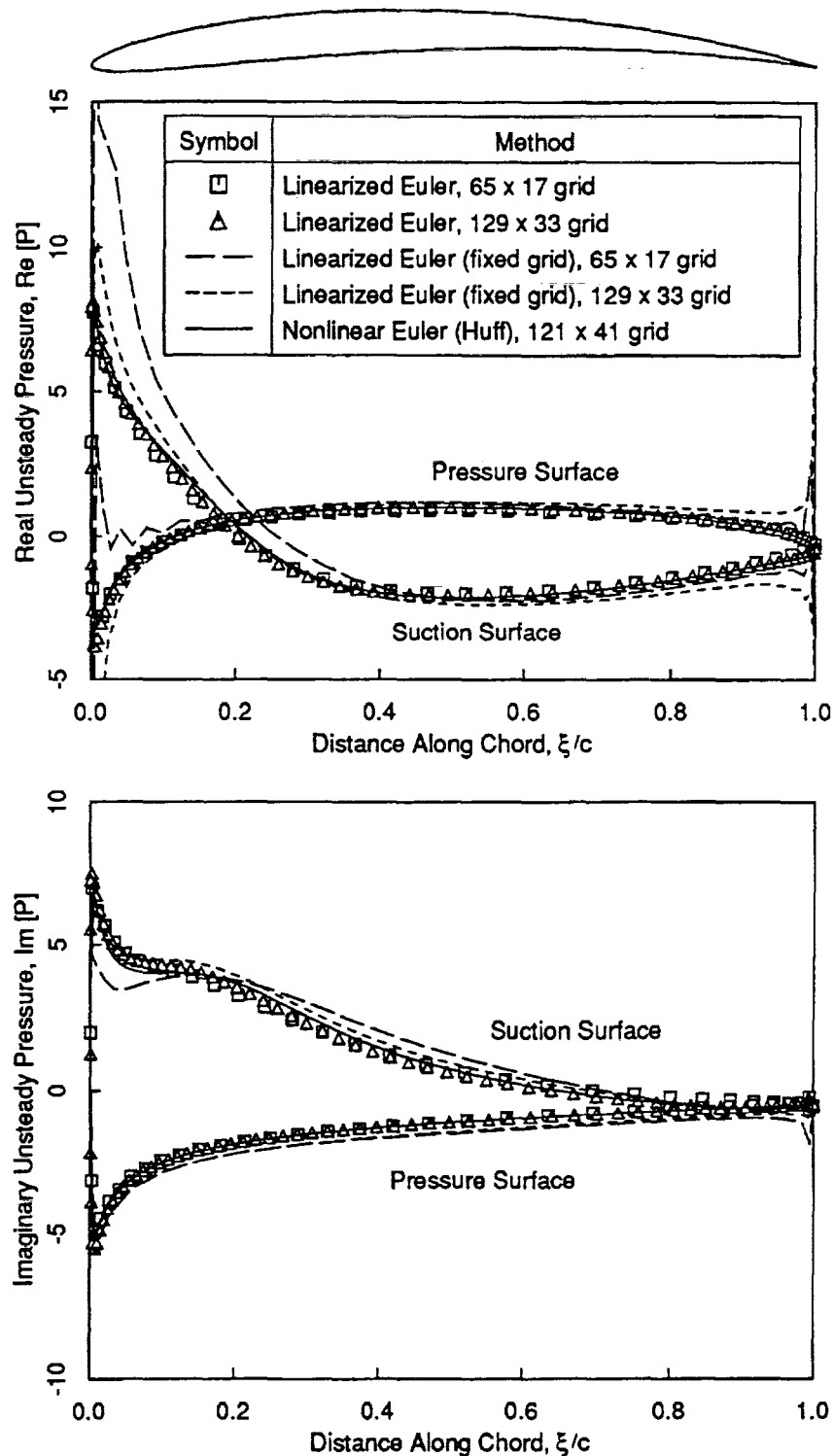


Figure 5.6: (top) Real unsteady pressure distribution for cascade of Tenth Standard Configuration airfoils undergoing an unsteady plunging motion; (bottom) Imaginary unsteady pressure distribution for cascade of Tenth Standard Configuration airfoils undergoing an unsteady plunging motion:  $k = 1.287$ ,  $\sigma = -90^\circ$

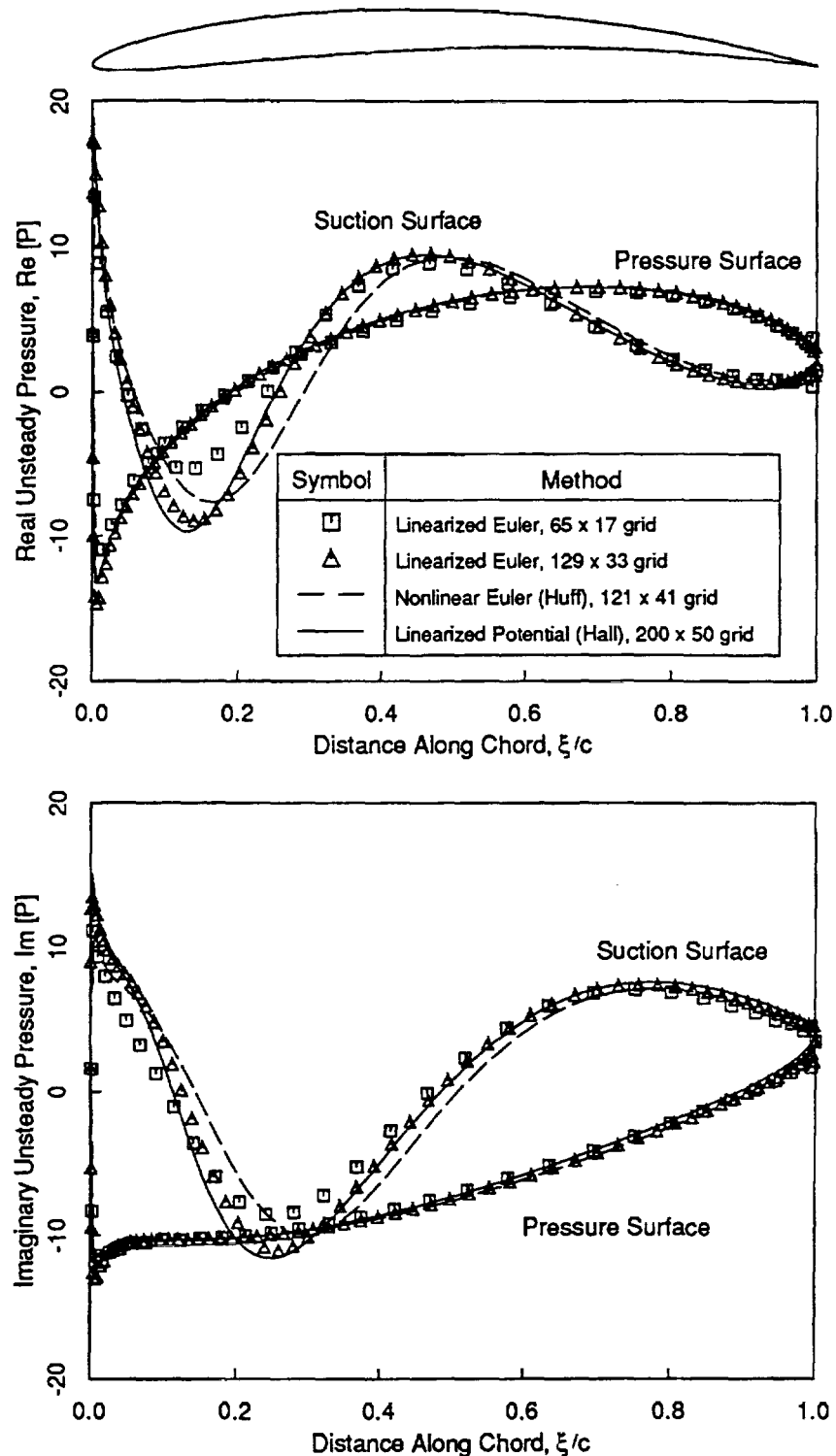


Figure 5.7: (top) Real unsteady pressure distribution for cascade of Tenth Standard Configuration airfoils undergoing an unsteady plunging motion; (bottom) Imaginary unsteady pressure distribution for cascade of Tenth Standard Configuration airfoils undergoing an unsteady plunging motion:  $k = 2.573$ ,  $\sigma = -180^\circ$

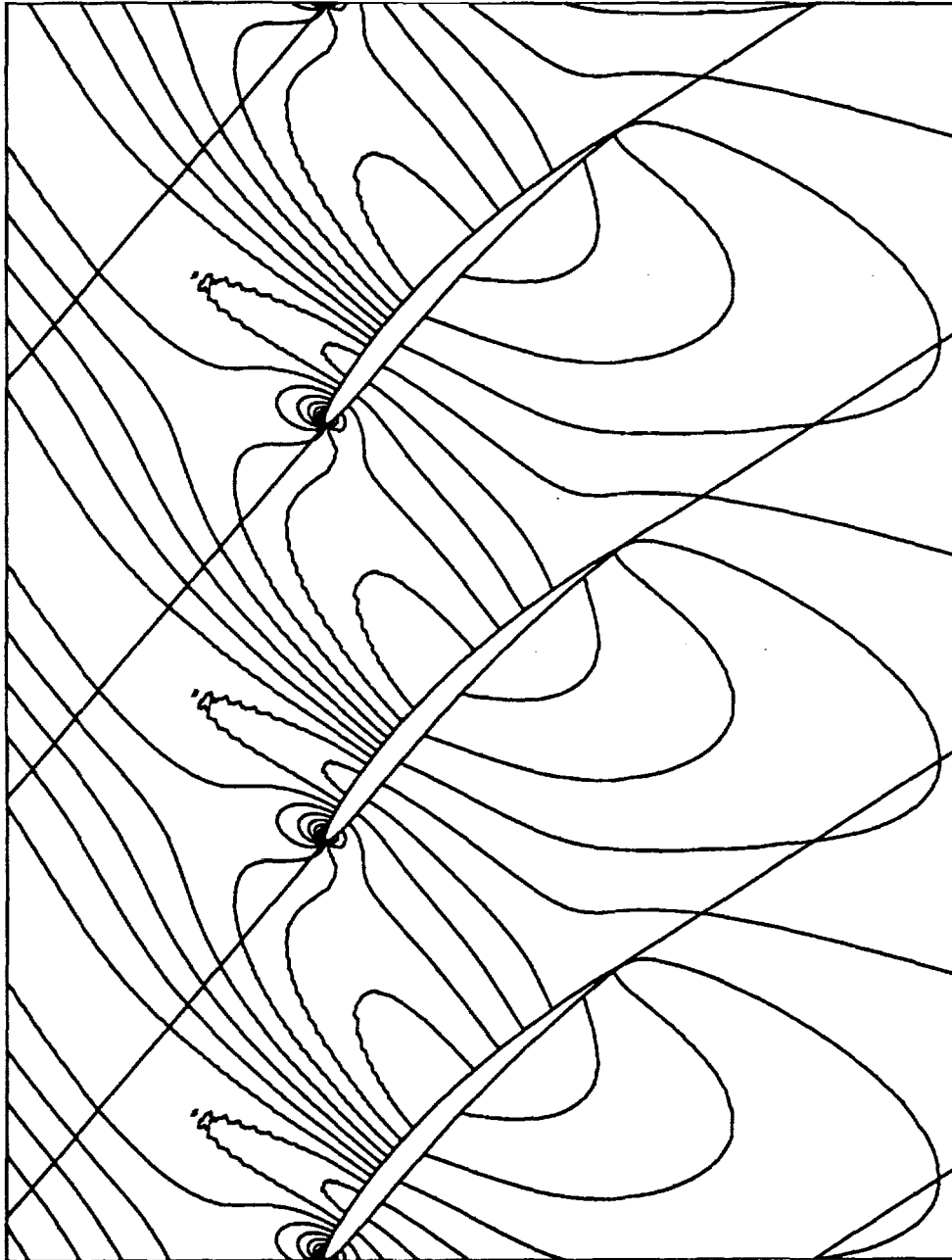


Figure 5.8: Unsteady pressure contours for cascade of Tenth Standard Configuration airfoils undergoing an unsteady plunging motion:  $k = 2.573$ ,  $\sigma = -180^\circ$

To further substantiate the effectiveness of the far-field boundary conditions, the same case was computed again. This time, however, the far-field boundaries were placed farther away from the blade row of interest. The unsteady surface pressures computed in the lengthened computational domain are compared to those previously computed and are shown in Fig. 5.9. The results indicate that the close proximity of the far-field boundary does not affect the unsteady pressure distribution. Additionally, by moving the boundaries closer to the blade row of interest, fewer computational nodes and hence computational resources are required to solve the problem.

Figure 5.10 shows the convergence histories for this flutter calculation (on the deforming grid) using the basic Lax-Wendroff solver alone and with Ni's multiple-grid acceleration technique. The convergence criteria is that the  $L_2$  norm of the  $pu$  corrections be less than  $5.0 \times 10^{-6}$ . Without the multiple-grid accelerator, the linearized unsteady Euler analysis required 6433 iterations to converge. With three levels of the multiple-grid accelerator, the linearized unsteady Euler analysis required just 773 iterations corresponding to about 14 minutes on a Stardent 3000 workstation. The nonlinear time marching solution, on the other hand, required 7384 iterations and approximately 88 minutes on a CRAY-YMP. When taking into consideration the difference in speeds of the two computers, one concludes that the linearized Euler analysis is nearly two orders-of-magnitude faster than the nonlinear analysis while still modeling the essential features of the unsteady flow. Additionally, for cases considered thus far, the multiple-grid accelerator works as well for the linearized unsteady Euler analysis as for the nonlinear, steady Euler analysis. The reduction seen in iteration count by additional multiple grid levels is approximately the same for both the steady and unsteady analyses, and both require approximately the same number of iterations to reach convergence.

Finally, having computed the unsteady pressure distribution on the airfoil surface, one can integrate to obtain the unsteady pitching moment and hence draw a conclusion about the flutter stability of the cascade (a positive imaginary part corresponds to negative aerodynamic damping). Shown in Fig. 5.11 is the imaginary part of the pitching moment for a cascade of Tenth Standard Configuration airfoils computed for a range of interblade phase angles,  $\sigma$ , from  $-180^\circ$  to  $+180^\circ$ , and at a reduced frequency,  $k, = 0.5$ . These results were obtained using a  $65 \times 17$  node computational grid. Also shown is the pitching moment computed using Hall's linearized potential method. The peaks in the solution are acoustic resonances. Note that there is generally good agreement between the linearized Euler and linearized potential solution. The good agreement (particularly in the superresonant regions) further substantiates the effectiveness of the far-field boundary conditions.

### 5.3 First Standard Configuration

In order to further validate the present method, we consider the case of a low speed compressor cascade known as the First Standard Configuration. This cascade was studied experimentally by Carta [10] and provides a good test of the present method's ability to predict the unsteady aerodynamic loading due to blade motion. The cascade

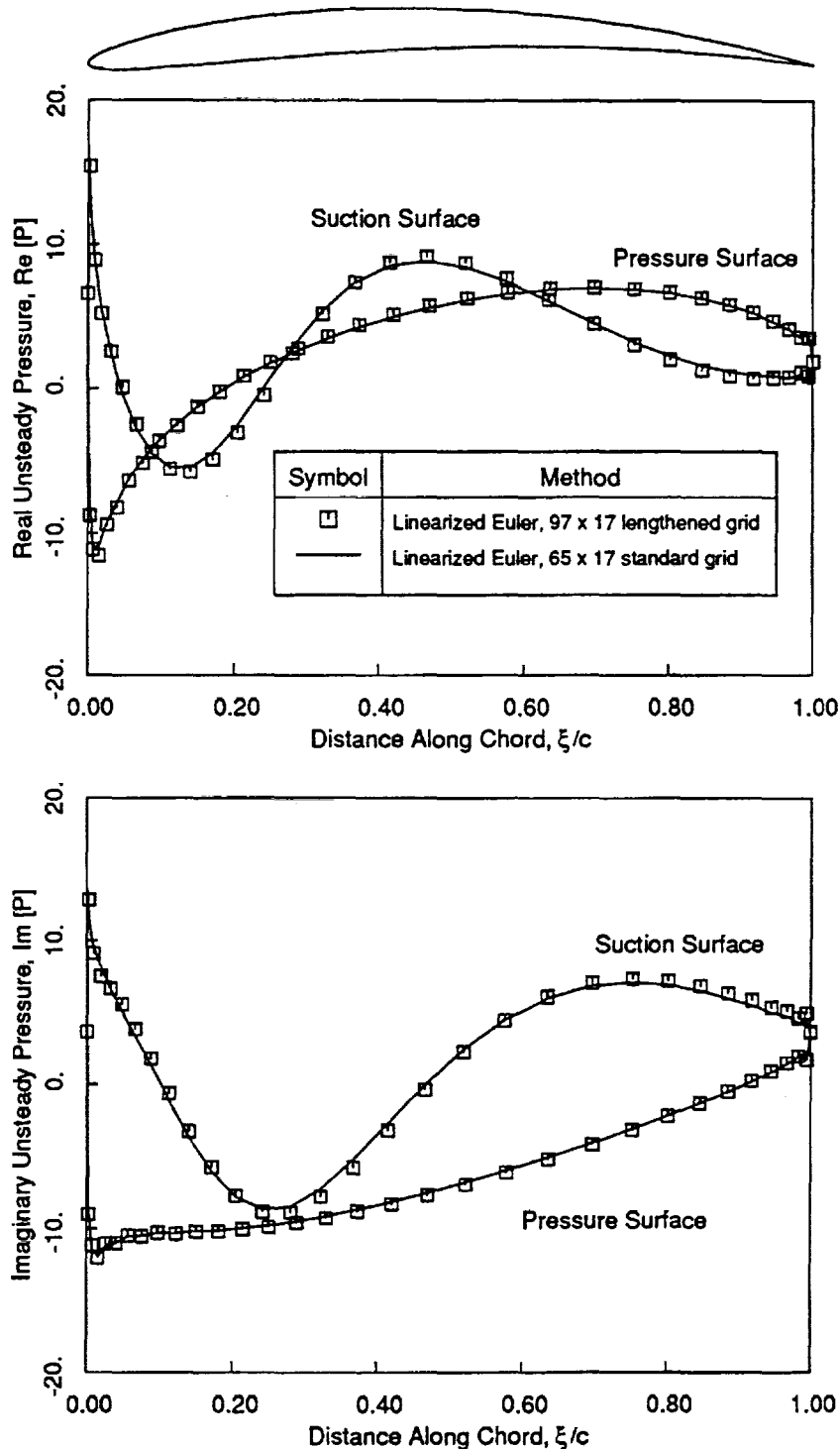


Figure 5.9: (top) Real unsteady pressure distribution for cascade of Tenth Standard Configuration airfoils undergoing an unsteady plunging motion; (bottom) Imaginary unsteady pressure distribution for cascade of Tenth Standard Configuration airfoils undergoing an unsteady plunging motion:  $k = 2.573$ ,  $\sigma = -180^\circ$

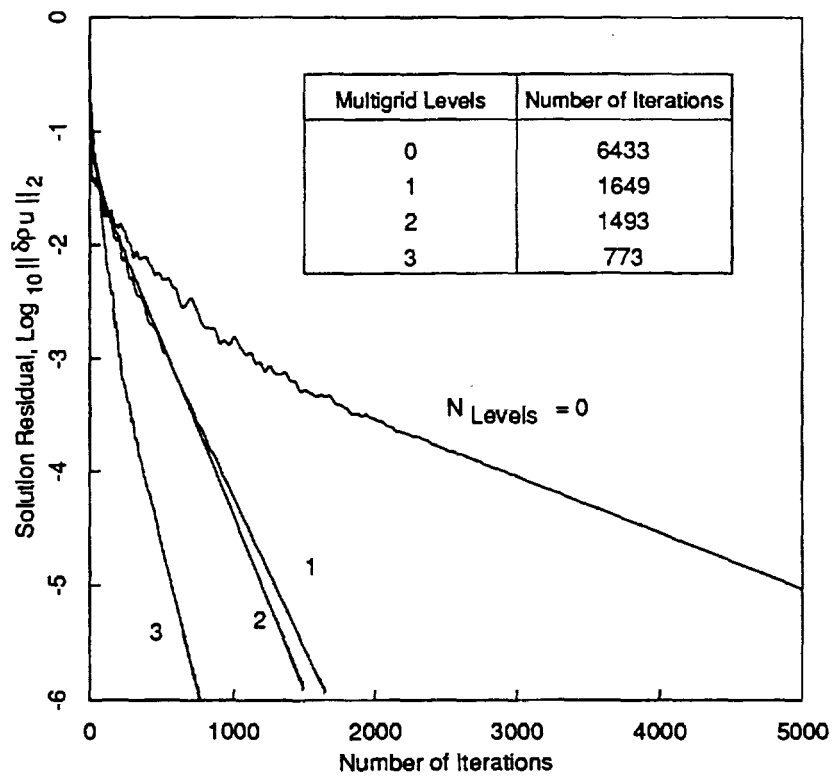


Figure 5.10: Convergence histories for cascade of Tenth Standard Configuration airfoils undergoing an unsteady plunging motion:  $k = 2.573$ ,  $\sigma = -180^\circ$

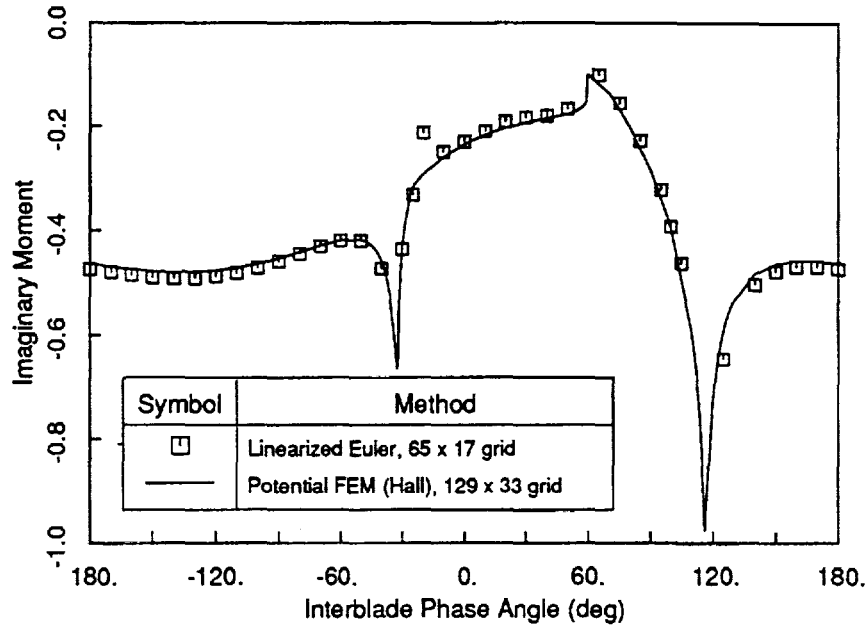


Figure 5.11: Imaginary part of unsteady pitching moment for cascade of Tenth Standard Configuration airfoils undergoing an unsteady pitching motion:  $k = 0.5$

is composed of airfoils which have  $10^\circ$  of camber and are 6 percent thick. The stagger angle,  $\Theta$ , is  $55^\circ$  and the gap-to-chord ratio,  $G$ , is 0.75. The reported inflow angle,  $\Omega_\infty$ , is  $66^\circ$  and the inflow Mach number,  $M_\infty$ , is 0.17. Figure 5.12 shows the steady surface pressure distribution calculated with the present nonlinear, steady Euler solver in addition to the experimentally measured values. For the unsteady case considered here, the airfoils vibrate in pitch about a point near their midchords with a reduced frequency,  $k$ , of 0.244 and an interblade phase angle,  $\sigma$ , of  $-90^\circ$ . The computed unsteady surface pressure is shown in Fig. 5.13 along with the experimental results of Carta. The computational results were obtained using a  $129 \times 33$  node grid. Overall, the agreement between the present analysis and the experiment, while not exact, is qualitatively very good.

## 5.4 Summary

The results obtained using the present linearized Euler analysis validated the present method against previous analytical, numerical, and experimental results. First, the flat plate cases studied were compared with an analytical solution computed using Whitehead's LINSUB. The excellent agreement proved that at least for flat plate cascades, the present linearized analysis can accurately and effectively calculate the unsteady aerodynamic forces for both the forced response and flutter problems. Next, a cascade of loaded airfoils (the Tenth Standard Configuration) was analyzed for several

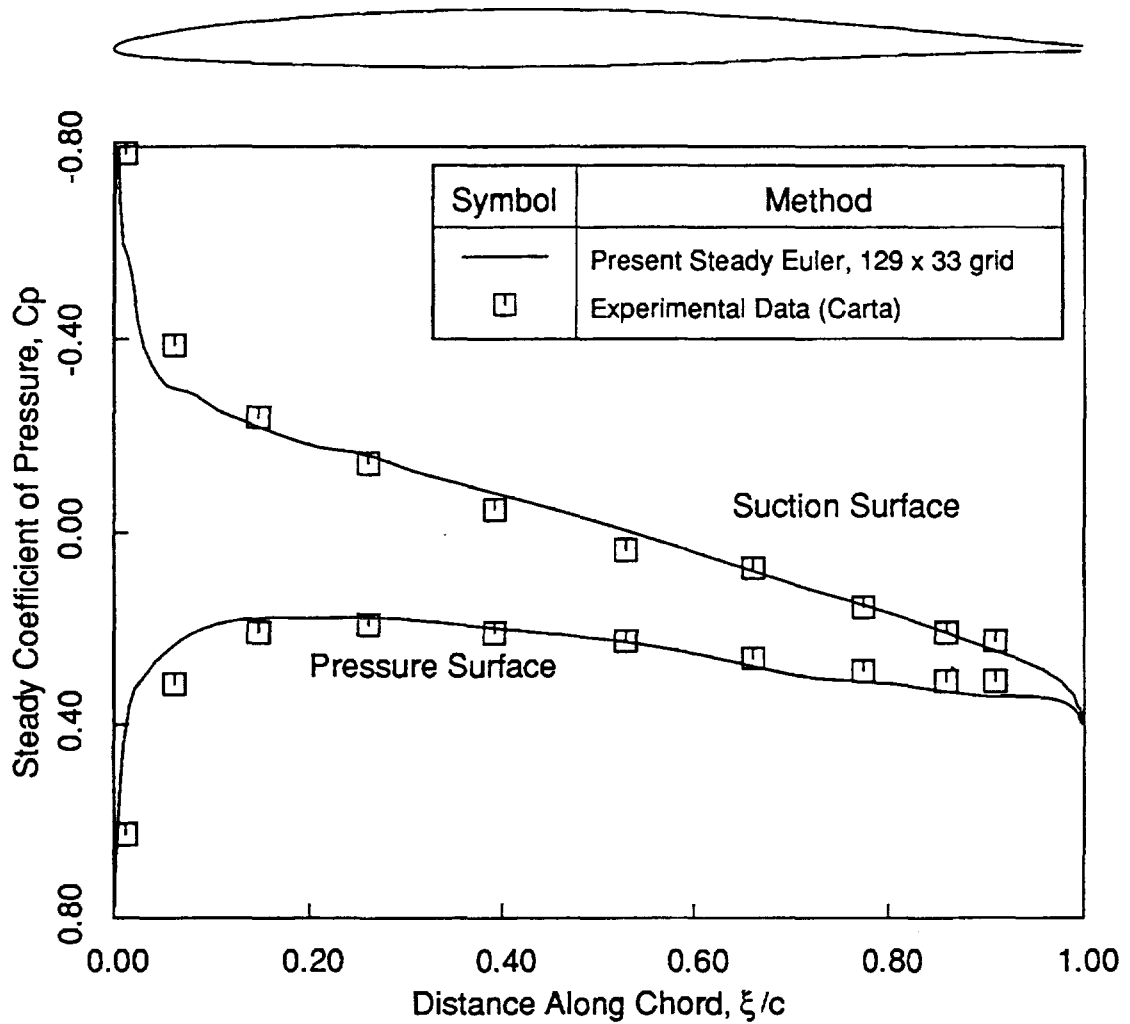


Figure 5.12: Steady coefficient of pressure distribution, First Standard Configuration:  $M_\infty = 0.17$ ,  $G = 0.75$ ,  $\Theta_\infty = 55^\circ$ ,  $\Omega_\infty = 66^\circ$

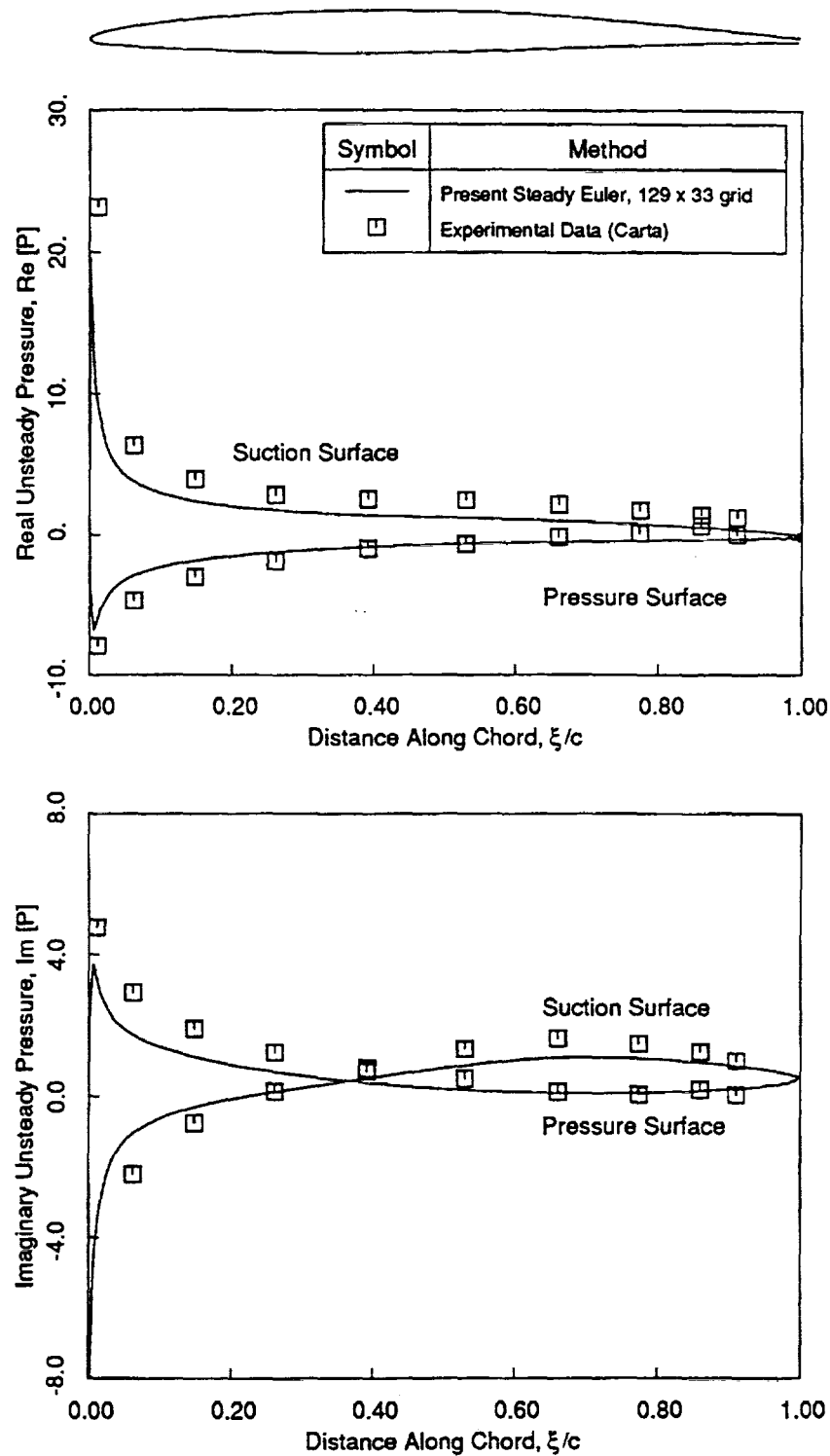


Figure 5.13: (top) Real unsteady pressure distribution for cascade of First Standard Configuration airfoils undergoing an unsteady pitching motion; (bottom) Imaginary unsteady pressure distribution for cascade of First Standard Configuration airfoils undergoing an unsteady pitching motion: (case 8)  $k = 0.244$ ,  $\sigma = -90^\circ$

unsteady operating conditions. The results agreed well with Hall's linearized potential as well as Huff's time-accurate time-marching unsteady Euler analysis. Finally, results from the present method were compared with Carta's experimental data (First Standard Configuration). Based on these comparisons, the present analysis appears to be accurate for a variety of geometries and flow conditions. In addition to accuracy, the results accompanying the Tenth Standard Configuration illustrated several important features of the present method. These include: (1) the far-field boundary conditions effectively eliminate spurious reflections, (2) the continuously deforming unsteady grid has effectively eliminated error producing extrapolation terms inherent in fixed grid calculations, and 3) the present linearized analysis has taken advantage of traditional computational acceleration techniques such as multigrid acceleration and local time-stepping. The conclusions drawn from these results are as follows. First, linearized analyses are indeed a viable method for the accurate prediction of unsteady loading in turbomachinery applications. Secondly, the computational efficiency makes linearized methods preferable to time-accurate time-marching methods as long as the small motion assumption of the linearized analyses is not violated.

# Chapter 6

## Transonic Theory

### 6.1 Introduction

In recent years, a number of linearized flow analyses have been developed to compute unsteady flows in cascades, especially the unsteady flows that produce the aeroelastic phenomena of flutter and forced response. The unsteady aerodynamic loads acting on transonic airfoils in cascades are composed of two parts: the unsteady pressure distribution away from the shock, and a “shock impulse” load that acts where the shock impinges on the airfoil surface. This shock impulse arises from the unsteady motion of the shock. Accurate prediction of the shock impulse is important since the unsteady aerodynamic load due to the shock impulse is of the same order as the unsteady aerodynamic loads due to the unsteady pressure away from the shock. In viscous flows, the shock is smeared near the airfoil surface due to shock/boundary layer interaction and hence, strictly speaking, no shock impulse exists at the surface. Away from the airfoil, however, the shock wave is very thin, typically on the order of a few mean free paths thick, and the concept of a shock impulse is important in connecting the regions of smooth flow on either side of the shock.

Verdon et al [48,50] and Whitehead [51,55] have developed linearized potential analyses of two-dimensional subsonic and transonic flows in cascades. Both Verdon and Whitehead have used shock capturing to model unsteady shock loads. Verdon has also used shock fitting in his linearized potential analysis to explicitly model the shock motion. Because of the assumption of isentropic and irrotational flow, however, these potential analyses cannot be used to model unsteady flows with strong shocks, flows with shocks that span the blade passage, or general three-dimensional flows. For this reason, investigators have begun to develop linearized Euler analyses of unsteady cascade flows [22,24,29,32]. Hall and Crawley [24] have shown that shock fitting can be implemented within the framework of a linearized Euler analysis to model accurately the unsteady motion of shocks. However, due to the inherent complexity of shock fitting algorithms, one would prefer to use the simpler shock capturing technique to model the shock impulse.

While shock capturing is favored for its simplicity, it has only recently been shown that the shock impulse load can be modelled properly using shock capturing within a linearized framework. There are two approaches that have been suggested for obtain-

ing discretizations of the linearized Euler equations. The first approach, referred to in this chapter as Method I, is to first discretize the nonlinear unsteady Euler equations and then linearize the resulting finite difference equations. The second approach, Method II, is to first linearize the nonlinear unsteady Euler equations, then discretize the resulting linearized equations using traditional finite difference or finite volume techniques. Lindquist and Giles [35,36] have argued that the unsteady shock loads will be correctly predicted provided the linearized code is a Method I type linearization of a time-accurate, conservative, nonlinear flow solver. Their results thus far, however, have been limited to quasi one-dimensional channel flows. Furthermore, they do not discuss the conditions under which Method II linearizations will properly model the shock impulse.

The objectives of this chapter are twofold. First, we demonstrate mathematically and by numerical experiment that the requirement put forth by Lindquist and Giles that the linearization be a Method I linearization of an unsteady nonlinear scheme is too stringent. We show that Method II linearizations will also work so long as the finite difference representation of the linearized Euler equations is conservative. Second, having demonstrated that conservative Method II linearizations may be used to properly model the unsteady shock impulse, we present a linearized Euler analysis (Method II type) of unsteady two-dimensional flow in cascades. Ni's Lax-Wendroff scheme [37] is used to obtain a finite volume representation of the unsteady linearized Euler equations. Computational results are presented for both one- and two- and three-dimensional unsteady transonic flows in cascades. Some of these calculations are compared to those computed using a nonlinear time-marching shock capturing Euler analysis. It is shown that the present unsteady linearized analysis agrees quite well with the nonlinear analysis, and further that the present linearized analysis is nearly two orders-of-magnitude more efficient than the nonlinear analysis. The computed results also demonstrate that the unsteady shock loads can provide a destabilizing influence on the flutter stability of cascades.

## 6.2 Theory

### 6.2.1 Flow Field Description

In this chapter, we again assume that the unsteady flow is inviscid and adiabatic, and that the unsteady flow in a cascade may be modelled by the Euler equations. For a two-dimensional Cartesian coordinate system, the Euler equations are given by

$$\frac{\partial \hat{U}}{\partial t} + \frac{\partial \hat{F}}{\partial x} + \frac{\partial \hat{G}}{\partial y} = 0 \quad (6.1)$$

where  $\hat{\mathbf{U}}$  is the vector of conservation variables,  $\hat{\mathbf{F}}$ , and  $\hat{\mathbf{G}}$  are the so-called flux vectors. These vector quantities are given by

$$\hat{\mathbf{U}} = \begin{bmatrix} \hat{\rho} \\ \hat{\rho}\hat{u} \\ \hat{\rho}\hat{v} \\ \hat{e} \end{bmatrix}, \quad \hat{\mathbf{F}} = \begin{bmatrix} \hat{\rho}\hat{u} \\ \hat{\rho}\hat{u}^2 + \hat{p} \\ \hat{\rho}\hat{u}\hat{v} \\ \hat{\rho}\hat{u}\hat{h} \end{bmatrix}, \quad \hat{\mathbf{G}} = \begin{bmatrix} \hat{\rho}\hat{v} \\ \hat{\rho}\hat{u}\hat{v} \\ \hat{\rho}\hat{v}^2 + \hat{p} \\ \hat{\rho}\hat{v}\hat{h} \end{bmatrix},$$

where  $\hat{\rho}$  is the density,  $\hat{p}$  is the pressure,  $\hat{u}$  and  $\hat{v}$  are the  $x$  and  $y$  components of velocity,  $\hat{e}$  is the internal energy, and  $\hat{h}$  is the enthalpy. The pressure,  $\hat{p}$ , and the enthalpy,  $\hat{h}$ , are given by

$$\hat{p} = (\gamma - 1) \left[ \hat{e} - \frac{1}{2} \hat{\rho} (\hat{u}^2 + \hat{v}^2) \right]$$

and

$$\hat{h} = \frac{\hat{e} + \hat{p}}{\hat{\rho}} = \frac{\gamma}{\gamma - 1} \frac{\hat{p}}{\hat{\rho}} + \frac{1}{2} (\hat{u}^2 + \hat{v}^2)$$

Next, we would like to determine the small disturbance behavior of Eq. 6.1 due to, for example, the fluttering motion of the blades of the cascade. To improve the accuracy of these calculations, a number of investigators have proposed the use of a harmonically deforming computational grid [22,23,29]. The motion of the grid is defined by

$$x(\xi, \eta, \tau) = \xi + f(\xi, \eta)e^{j\omega\tau} \quad (6.2a)$$

$$y(\xi, \eta, \tau) = \eta + g(\xi, \eta)e^{j\omega\tau} \quad (6.2b)$$

$$t(\xi, \eta, \tau) = \tau \quad (6.2c)$$

where  $\omega$  is the frequency of vibration of the blades, and where  $f$  and  $g$  are the perturbation amplitudes of the grid motion about the mean positions,  $\xi$  and  $\eta$ . Having defined the grid motion, the unsteady flow field is represented by the perturbation series

$$\hat{\mathbf{U}}(\xi, \eta, \tau) = \mathbf{U}(\xi, \eta) + \mathbf{u}(\xi, \eta)e^{j\omega\tau} \quad (6.3)$$

Substitution of Eq. 6.3 into Eq. (6.1) and collection of the terms that are first-order in the perturbation  $\mathbf{u}$  results in the linearized Euler equations,

$$j\omega\mathbf{u} + \frac{\partial}{\partial\xi} \left( \frac{\partial\mathbf{F}}{\partial\mathbf{U}}\mathbf{u} \right) + \frac{\partial}{\partial\eta} \left( \frac{\partial\mathbf{G}}{\partial\mathbf{U}}\mathbf{u} \right) = \mathbf{b} \quad (6.4)$$

where  $\mathbf{b}$  is a fairly complex expression which depends on the mean flow and the prescribed grid motion.

## 6.2.2 Numerical Modelling of the Shock Impulse

The first question we address in this chapter is: What is the proper way to discretize and linearize the Euler equations in such a way that the linearized finite difference or

finite volume equations properly predict the shock impulse loads that result from the unsteady shock motion. There are two obvious approaches one can take to obtain a discretization of the linearized Euler equations. One approach (Method I) is to first discretize the nonlinear Euler equations and then linearize the resulting nonlinear finite difference equations. The other approach (Method II) is to first linearize the nonlinear Euler equations then discretize the resulting linearized equations. We claim here that both approaches will produce the correct result provided that the resulting difference equations are conservative (we give a more precise definition of what conservative means in the linearized case shortly). A mathematical justification of this conjecture is given below.

Due to the complexity of the two-dimensional Euler equations, we consider the simpler one-dimensional model equation given by

$$\frac{\partial \hat{U}}{\partial t} + \frac{\partial \hat{F}}{\partial x} + B\hat{P} = 0 \quad (6.5)$$

where  $\hat{F} = \hat{F}(\hat{U})$ ,  $\hat{P} = \hat{P}(\hat{U})$ , and  $B = B(x)$ . This model equation is very similar in form to the quasi-one-dimensional Euler equations which describe flow in a channel with a spatially varying cross sectional area. Since  $\hat{F}$  and  $\hat{P}$  are in general nonlinear functions of the conservation variable  $\hat{U}$ , this model equation is nonlinear.

As before, we model the conservation variable  $\hat{U}$  as the sum of a mean part  $U$  plus a small harmonic perturbation  $ue^{j\omega t}$ . The mean solution is solution is governed by

$$\frac{\partial F}{\partial x} + BP = 0 \quad (6.6)$$

where  $F = F(U)$  and  $P = P(U)$ . The linearized unsteady model equation is given by

$$j\omega u + \frac{\partial}{\partial x} \left( \frac{\partial F}{\partial U} u \right) + B \frac{\partial P}{\partial U} u = 0 \quad (6.7)$$

where  $u$  is the perturbation solution, and  $\frac{\partial F}{\partial U}$  and  $\frac{\partial P}{\partial U}$  are steady flow Jacobians.

Returning for the moment to the unsteady nonlinear model equation, Eq. 6.5, it is well known that because the model equation is nonlinear, it will in general admit genuine solutions, that is, solutions with flow discontinuities. In smooth regions of the flow, the genuine solutions satisfy the differential equation, Eq. 6.5. The *weak* solution is that genuine solution which also satisfies the integral relation

$$\int \int (g_t \hat{U} - g_x \hat{F}) dx dt + \int g(x, 0) \hat{U}(x, 0) dx = 0 \quad (6.8)$$

for every test function  $g(x, t)$  which vanishes for large  $x$  or  $t$  and which has continuous first derivatives [33,34]. One can then show that the unsteady Rankine-Hugoniot shock jump conditions at flow discontinuities are given by

$$\dot{X}, \left[ [\hat{U}] \right] - \left[ [\hat{F}] \right] = 0 \quad (6.9)$$

where the symbol  $[[\cdot\cdot\cdot]]$  denotes the jump in the enclosed quantity across the shock, and  $\dot{X}_s$  is the velocity of the shock.

If one then considers an unsteady flow with small harmonic unsteadiness, one may linearize Eq. 6.9 to obtain the linearized shock jump conditions [24].

$$j\omega x_s [[U]] - \left[ \left[ \frac{\partial F}{\partial U} u \right] \right] - x_s \left[ \left[ \frac{\partial F}{\partial x} \right] \right] = 0 \quad (6.10)$$

where  $u$  is the small disturbance part of the unsteady flow and  $x_s$  is the small complex amplitude of the shock motion. Noting that the steady flow solution is given by  $\partial F/\partial x = -BP$ , Eq. 6.10 may be rewritten as

$$j\omega x_s [[U]] - \left[ \left[ \frac{\partial F}{\partial U} u \right] \right] + x_s B [[P]] = 0 \quad (6.11)$$

A graphical interpretation of Eq. 6.11 is shown in Fig. 6.2.2. Shown are the mean and unsteady flow shock trajectories as well as the resulting unsteady flow,  $\hat{U}$ , the mean flow  $U$ , and the perturbation flow,  $u$ . The latter is just the difference between the unsteady and mean flows,  $u = \hat{U} - U$ . Note that near the shock, an impulse in  $u$  appears due to the motion of the shock. In the limit as the unsteadiness in the flow tends toward zero, the integrated value of this impulse is given by

$$I_u = \int_{X_s - \epsilon}^{X_s + \epsilon} u dx = -x_s [[U]] = -x_s (U_2 - U_1) \quad (6.12)$$

Finally, Eq. 6.11 may be written as

$$j\omega I_u + \left[ \left[ \frac{\partial F}{\partial U} u \right] \right] + B I_p = 0 \quad (6.13)$$

We presently demonstrate that the weak solution of the linearized unsteady model equation, Eq. 6.7, produces an equivalent shock jump condition. Multiplying Eq. 6.7 by a test function  $g(x)$  and integrating the result over the solution domain  $x \in [0, L]$ , we obtain

$$\int_0^L g(x) \left[ j\omega u + \frac{\partial}{\partial x} \left( \frac{\partial F}{\partial U} u \right) + B \frac{\partial P}{\partial U} u \right] dx = 0 \quad (6.14)$$

Integration by parts applied to the middle term in Eq. 6.14 gives

$$\int_0^L \left[ j\omega g u - \frac{dg}{dx} \frac{\partial F}{\partial U} u + g B \frac{\partial P}{\partial U} u \right] dx + \left( g \frac{\partial F}{\partial U} u \right) \Big|_0^L = 0 \quad (6.15)$$

Next we let the test function  $g(x)$  be given by

$$g(x) = \begin{cases} 1 & \text{if } X_s - \epsilon \leq x \leq X_s + \epsilon \\ 0 & \text{otherwise} \end{cases} \quad (6.16)$$

where  $X_s$  is the mean shock position and  $\epsilon$  is a small positive number. Differentiating Eq. 6.16 with respect to  $x$  gives

$$\frac{dg}{dx} = \delta[x - (X_s - \epsilon)] - \delta[x - (X_s + \epsilon)] \quad (6.17)$$

where  $\delta[\dots]$  is the Dirac delta function. Substitution of Eqs. 6.16 and 6.17 into Eq. 6.15 gives the desired shock jump conditions of the linearized unsteady model equation,

$$j\omega \int_{X_s-\epsilon}^{X_s+\epsilon} u dx + \left[ \left[ \frac{\partial F}{\partial U} u \right] \right] + B \int_{X_s-\epsilon}^{X_s+\epsilon} \frac{\partial P}{\partial U} u dx = 0 \quad (6.18)$$

The integrals in Eq. 6.18 are the areas under the impulse in  $u$  and the impulse in  $p$ , the perturbations in the conservation variable and pressure, respectively, and are denoted here by  $I_u$  and  $I_p$  (See Fig. 6.2.2).

Finally then, we may write the Rankine-Hugoniot jump conditions for the linearized unsteady Euler equations as

$$j\omega I_u + \left[ \left[ \frac{\partial F}{\partial U} u \right] \right] + B I_p = 0 \quad (6.19)$$

This expression is identical to Eq. (13) thus demonstrating that the weak solution to the linearized unsteady model equation is the same as the linearized weak solution of the nonlinear model equation.

We conclude, therefore, that for a finite difference scheme to properly model the linearized unsteady model equation, the finite difference scheme must be stable and consistent *and* satisfy the condition given by Eq. 6.15 in the limit as  $\Delta x$  and  $\Delta t$  tend toward zero. In other words, the order of linearization is immaterial; what matters is whether the resulting discretization is conservative. Note that this condition is less stringent than the condition suggested by Lindquist and Giles [35,36] that the discretization be both conservative and a Method I linearization. Also note the importance of the *area* of the impulse. When capturing the shock impulse, the width and height of the impulse will depend on the amount of smoothing (or artificial viscosity) in the numerical scheme. The area under the impulse, however, should be independent of the smoothing.

### 6.2.3 Method I and Method II Linearizations

To illustrate the difference between Method I and Method II linearizations, we consider again the model equation given by Eq. (5) with the source term set to zero ( $B = 0$ ).

#### Method I Linearization

Consider the discretization of the nonlinear unsteady model equation, Eq. (5), using the Lax-Wendroff scheme. The one-dimensional computational grid is assumed to have constant cell size  $\Delta x$  and constant time step  $\Delta t$ . The solution at time level  $n + 1$  is found by Taylor expanding the solution about time level  $n$  to obtain

$$\hat{U}_i^{n+1} = \hat{U}_i^n + \Delta t \left. \frac{\partial \hat{U}}{\partial t} \right|_i^n + \frac{\Delta t^2}{2} \left. \frac{\partial^2 \hat{U}}{\partial t^2} \right|_i^n + \mathcal{O}(\Delta t^3) \quad (6.20)$$

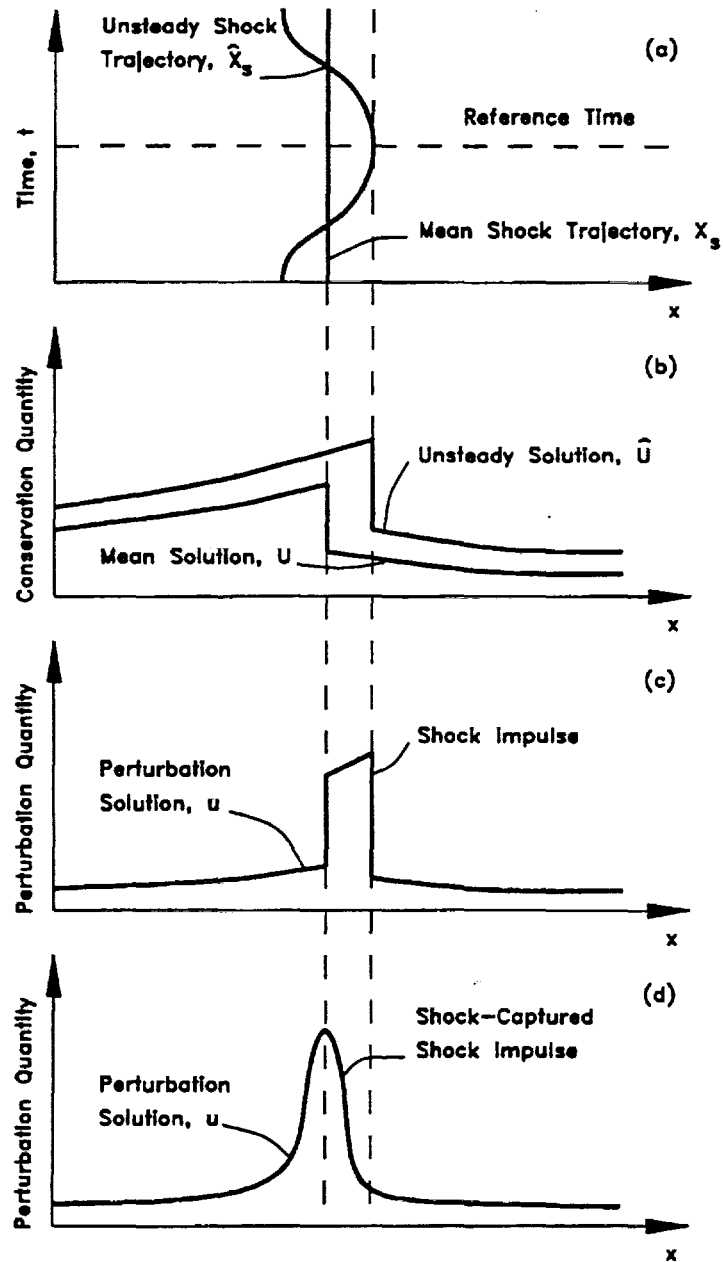


Figure 6.1: Top to bottom: (a) Trajectory of shock in a channel or on airfoil surface; (b) Mean and unsteady flow distribution; (c) Perturbation flow showing shock impulse; (d) same as (c) with impulse modelled by shock capturing. Note the area under the impulse is the same in (c) and (d).

where  $i$  denotes the  $i$ th grid node in the  $x$ -direction. The time derivatives in Eq. 6.20 are obtained by manipulation of the original model equation, Eq. (5). Rearranging Eq. (5) gives

$$\frac{\partial \hat{U}}{\partial t} = -\frac{\partial \hat{F}(\hat{U})}{\partial x} \quad (6.21)$$

Differentiating Eq. 6.21 with respect to time gives

$$\frac{\partial^2 \hat{U}}{\partial t^2} = -\frac{\partial}{\partial x} \left( \frac{\partial \hat{F}}{\partial \hat{U}} \frac{\partial \hat{U}}{\partial t} \right) = \frac{\partial}{\partial x} \left( \frac{\partial \hat{F}}{\partial \hat{U}} \frac{\partial \hat{F}}{\partial x} \right) \quad (6.22)$$

Next, substitution of Eqs. 6.21 and 6.22 into Eq. 6.20 yields

$$\hat{U}_i^{n+1} = \hat{U}_i^n - \Delta t \left. \frac{\partial \hat{F}}{\partial x} \right|_i^n + \frac{\Delta t^2}{2} \frac{\partial}{\partial x} \left( \frac{\partial \hat{F}}{\partial \hat{U}} \frac{\partial \hat{F}}{\partial x} \right) \Big|_i^n + \mathcal{O}(\Delta t^3) \quad (6.23)$$

Finally, using centered finite difference expressions to approximate the spatial derivatives, the familiar Lax-Wendroff finite difference equation is obtained, i.e.,

$$\hat{U}_i^{n+1} = \hat{U}_i^n - \frac{\Delta t}{2\Delta x} \left[ \hat{F}_{i+1}^n - \hat{F}_{i-1}^n \right] + \frac{\Delta t^2}{2\Delta x^2} \left[ \left. \frac{\partial \hat{F}}{\partial \hat{U}} \right|_{i+1/2}^n \left( \hat{F}_{i+1}^n - \hat{F}_i^n \right) - \left. \frac{\partial \hat{F}}{\partial \hat{U}} \right|_{i-1/2}^n \left( \hat{F}_i^n - \hat{F}_{i-1}^n \right) \right] \quad (6.24)$$

The Lax-Wendroff scheme above is second-order accurate [ $\mathcal{O}(\Delta x^2, \Delta t^2)$ ] and is conservative (since by assumption  $\Delta x$  and  $\Delta t$  are constant). A Fourier stability analysis indicates the scheme is stable for CFL numbers less than unity. Lax [33] and Lax and Wendroff [34] have shown that if the conservative form of the Euler equations is used, and the discretization of the Euler equations satisfies numerical conservation, and further that the scheme is consistent and stable, then the shock wave speed and strength will be correctly predicted. The Lax-Wendroff scheme above satisfies these conditions and therefore will correctly predict the unsteady shock motion.

Next, we would like to determine the behavior of Eq. 6.24 when the unsteadiness in the flow is small compared to the mean flow field. Since the resulting equations will be linear, we may without loss of generality assume that the flow field is composed of a nonlinear steady mean flow and a small perturbation harmonic unsteady flow so that

$$\hat{U}(x, t) = U(x) + u(x)e^{j\omega t} \quad (6.25)$$

where  $u$  is much smaller than  $U$ . When viewed on our computational grid, Eq. 6.25 becomes

$$\hat{U}_i^n = U_i + u_i e^{j\omega \Delta t n} \quad (6.26)$$

Substitution of Eq. 6.26 into Eq. 6.24 and collecting terms of first order in the perturbation quantity  $u$  gives the desired discrete small disturbance behavior of the nonlinear finite difference equations,

$$(1 - e^{j\omega \Delta t}) u_i - \frac{\Delta t}{2\Delta x} \left[ \left. \frac{\partial F}{\partial U} \right|_{i+1} u_{i+1} - \left. \frac{\partial F}{\partial U} \right|_{i-1} u_{i-1} \right]$$

$$\begin{aligned}
& + \frac{\Delta t^2}{2\Delta x^2} \left[ \frac{\partial F}{\partial U} \Big|_{i+1/2} \left( \frac{\partial F}{\partial U} \Big|_{i+1} u_{i+1} - \frac{\partial F}{\partial U} \Big|_i u_i \right) - \frac{\partial F}{\partial U} \Big|_{i-1/2} \left( \frac{\partial F}{\partial U} \Big|_i u_i - \frac{\partial F}{\partial U} \Big|_{i-1} u_{i-1} \right) \right] \\
& + \frac{\Delta t^2}{2\Delta x^2} \left[ \frac{\partial^2 F}{\partial U^2} \Big|_{i+1/2} u_{i+1/2} (F_{i+1} - F_i) - \frac{\partial^2 F}{\partial U^2} \Big|_{i-1/2} u_{i-1/2} (F_i - F_{i-1}) \right] = 0 \quad (6.27)
\end{aligned}$$

Equation 6.27 describes the small disturbance behavior of the nonlinear Lax-Wendroff equation. One interesting feature of Eq. 6.27 is the appearance of the terms involving  $\partial^2 F / \partial U^2$ . These terms appear because of nonlinearities of the Lax-Wendroff scheme itself rather than nonlinearities of the Euler equations.

For a one-dimensional problem, Eq. 6.27, along with appropriate inflow and outflow boundary conditions, could be assembled into a tridiagonal matrix equation which could then be solved quite efficiently using Gaussian elimination (the Thomas algorithm). For two- and three-dimensional problems, however, this approach would be computationally expensive and require large amounts of computer storage. For these reasons, an iterative solution technique is preferred. The following explicit relaxation procedure is proposed:

$$u_i^{n+1} = u_i^n + \delta u_i^n \quad (6.28)$$

where  $\delta u_i$  is the left-hand side of Eq. 6.27. As Eq. 6.28 is marched in time, a steady state value of  $u_i^n$  will be obtained and the solution to Eq. 6.27 will be recovered. This procedure is similar to the pseudo-time time-marching technique proposed by Ni and Sisto [39] for solving the linearized Euler equations. Equation 6.27 can be shown to be consistent with the linearized model equation, Eq. (7), with truncation errors which are  $\mathcal{O}(\Delta x^2, \Delta t^2)$ . A Fourier analysis of Eq. 6.28 reveals that the scheme is unconditionally unstable if  $\omega$  is non zero. A spectral radius stability analysis, however, that takes into account the stabilizing effect of the far-field boundary conditions shows that the scheme is stable for CFL numbers less than unity [12].

## Method II Linearization

An alternative approach to Method I is to first linearize the nonlinear unsteady flow equations, and then discretize the resulting linear equations. To illustrate this approach, we return again to the one-dimensional model equation given by Eq. (5) and, introducing the pseudo-time assumption of Ni and Sisto [39], assume that the unsteady flow  $\hat{U}(x, t)$  is composed of a nonlinear mean flow,  $U(x)$ , plus a small unsteady harmonic perturbation flow,  $u(x, t)e^{j\omega t}$ , so that

$$\hat{U}(x, t) = U(x) + u(x, t)e^{j\omega t} \quad (6.29)$$

Substitution of Eq. 6.29 into Eq. (5) and collection of first-order terms results in the pseudo-time linearized model equation

$$\frac{\partial u}{\partial t} + j\omega u + \frac{\partial}{\partial x} \left( \frac{\partial F}{\partial U} u \right) = 0 \quad (6.30)$$

Note that Eq. 6.30 is now hyperbolic in time so that it can be marched in time. Furthermore, as time advances,  $u$  will reach a steady-state value so that the solution to Eq. (7) will be recovered.

The next step is to discretize the linearized equation using the Lax-Wendroff scheme. Manipulation of Eq. 6.30 gives

$$\frac{\partial u}{\partial t} = -j\omega u - \frac{\partial}{\partial x} \left( \frac{\partial F}{\partial U} u \right) \quad (6.31)$$

and

$$\frac{\partial^2 u}{\partial t^2} = -\omega^2 u + 2j\omega \frac{\partial}{\partial x} \left( \frac{\partial F}{\partial U} u \right) + \frac{\partial}{\partial x} \left[ \frac{\partial F}{\partial U} \frac{\partial}{\partial x} \left( \frac{\partial F}{\partial U} u \right) \right] \quad (6.32)$$

Finally, making use of centered spatial derivatives and substitution into the Taylor expansion, Eq. (20) gives the desired Lax-Wendroff formula,

$$\begin{aligned} \delta u_i^n = & -\frac{j\omega\Delta t}{4} \left[ u_{i+1}^n + 2u_i^n + u_{i-1}^n \right] - \frac{\Delta t}{2\Delta x} \left[ \left. \frac{\partial \bar{F}}{\partial \bar{U}} \right|_{i+1/2} u_{i+1}^n - \left. \frac{\partial \bar{F}}{\partial \bar{U}} \right|_{i-1/2} u_{i-1}^n \right] \\ & - \frac{\omega^2 \Delta t^2}{8} \left[ u_{i+1}^n + 2u_i^n + u_{i-1}^n \right] \\ & + \frac{j\omega\Delta t}{4} \frac{\Delta t}{\Delta x} \left[ \left. \frac{\partial \bar{F}}{\partial \bar{U}} \right|_{i+1/2} u_{i+1}^n - \left. \frac{\partial \bar{F}}{\partial \bar{U}} \right|_{i-1/2} u_{i-1}^n \right] \\ & + \frac{j\omega\Delta t}{2} \frac{\Delta t}{\Delta x} \left[ \left. \frac{\partial \bar{F}}{\partial \bar{U}} \right|_{i+1/2} u_{i+1/2}^n - \left. \frac{\partial \bar{F}}{\partial \bar{U}} \right|_{i-1/2} u_{i-1/2}^n \right] \\ & + \frac{\Delta t^2}{2\Delta x^2} \left[ \left. \frac{\partial \bar{F}}{\partial \bar{U}} \right|_{i+1/2} \left( \left. \frac{\partial \bar{F}}{\partial \bar{U}} \right|_{i+1} u_{i+1}^n - \left. \frac{\partial \bar{F}}{\partial \bar{U}} \right|_i u_i^n \right) \right. \\ & \left. - \left. \frac{\partial \bar{F}}{\partial \bar{U}} \right|_{i-1/2} \left( \left. \frac{\partial \bar{F}}{\partial \bar{U}} \right|_i u_i^n - \left. \frac{\partial \bar{F}}{\partial \bar{U}} \right|_{i-1} u_{i-1}^n \right) \right] \quad (6.33) \end{aligned}$$

As in the Method I discretization [Eq. (27)], the Method II discretization [Eq. 6.33] is consistent with the linearized model equation [Eq. (7)] with truncation errors which are  $\mathcal{O}(\Delta x^2, \Delta t^2)$ .

Note that the Method II discretization [Eq. 6.33] differs significantly from that obtained using Method I [Eq. (27)]. In particular, the unsteady terms involving  $\omega$  are somewhat different, and the quasi-steady terms involving  $\partial^2 F / \partial U^2$  in Eq. (27) do not appear in Eq. 6.33. Clearly, the order in which the linearization is performed is important in determining the precise form of the difference equations.

## 6.2.4 Test for Linearized Conservation

Consider the Method I discretization of the model equation, Eq. (27). The one-dimensional computational grid has  $M$  nodes. To test for conservation, Eq. (27) is multiplied by  $g_i \Delta x / \Delta t$  (where  $g_i = g(x_i)$ ) and summed over the computational domain. After some manipulation including summation by parts, one can show that this sum is given by

$$\frac{(1 - e^{j\omega t})}{\Delta t} \sum_{i=1}^M u_i g_i \Delta x + \sum_{i=2}^{M-1} \frac{g_{i+1} - g_{i-1}}{2\Delta x} \frac{\partial F}{\partial U} \Big|_i u_i \Delta x - g_M \frac{\partial F}{\partial U} \Big|_M u_M + g_0 \frac{\partial F}{\partial U} \Big|_0 u_0 + \mathcal{O}(\Delta x, \Delta t) \quad (6.34)$$

In the limit as  $\Delta t, \Delta x \rightarrow 0$ , Eq. 6.34 approaches Eq. (15). Therefore, this Method I linearization of the Lax-Wendroff scheme is conservative (at least for the case considered here of constant  $\Delta t, \Delta x$ ). A similar analysis of Method II reveals that is also conservative. Hence, *both* methods should correctly predict the shock impulse.

## 6.3 Results

### 6.3.1 Transonic Channel Flow

To test the present linearized Euler analyses, we first consider the transonic flow through a diverging channel. This case is presented to demonstrate the ability of the linearized Euler method to model shock motion accurately using shock capturing. We will demonstrate that both Method I and Method II linearizations will produce satisfactory results so long as they are conservative.

The channel considered here has a height,  $A$ , given by,

$$A(x) = A_{inlet} \left\{ 1.10313 + 0.10313 \tanh \left[ 10 \left( x - \frac{1}{2} \right) \right] \right\}, 0 \leq x \leq 1 \quad (6.35)$$

(The units may be taken to be any consistent set of units.) So that we may compare the results obtained by the present method to those obtained by a one-dimensional shock-fitting theory,  $A_{inlet}$  is taken to be small compared with the channel length ( $A_{inlet} = 0.01$ ). The inflow total pressure,  $P_T$ , total density,  $\rho_T$ , and flow velocity,  $U$ , are 1.0, 1.364, and 1.0 respectively. The back pressure,  $P_{exit}$ , is 0.7422. Shown in Fig. 6.3.1 is the Mach number and pressure distribution as computed using the present nonlinear steady Euler solver on a  $129 \times 5$  node computational grid. The grid was generated so that the computational cells all have the same area,  $\Delta A$ . The time step,  $\Delta t$ , used in these calculations was constant throughout the computational domain unless otherwise noted. Constant  $\Delta t$  and  $\Delta A$  were chosen because Ni's scheme is only conservative if the ratio  $\Delta t / \Delta A$  is constant throughout the computational domain.

Also shown for comparison in Fig. 6.3.1 is the solution determined using a steady quasi-one-dimensional, shock-fitting Euler solver using 1001 grid nodes in the  $x$ -direction. The shock-fitting Euler solution is grid converged and may be taken to

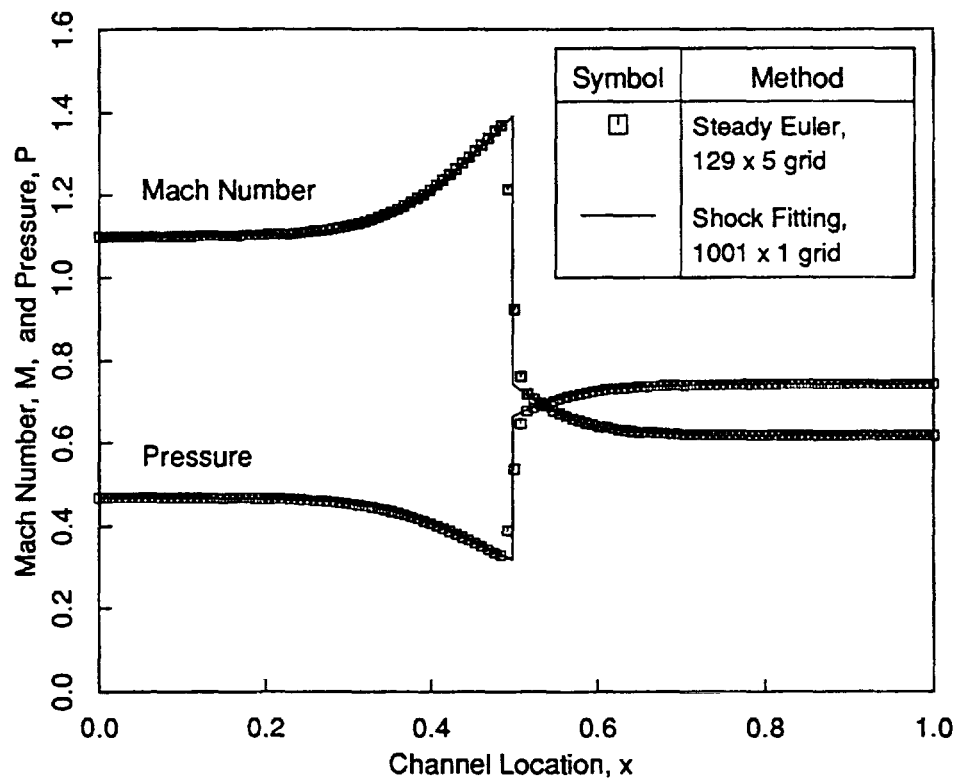


Figure 6.2: Steady transonic flow in a diverging channel

be the exact solution. Note the excellent agreement between the two different approaches. The only noticeable differences occur at the shock, where the present nonlinear Euler analysis distributes the shock over about five grid nodes.

Next, we consider a quasi-steady perturbation in the back pressure. The perturbation solution was calculated using four different approaches. First, the solution was calculated using a quasi-one-dimensional, shock-fitting, linearized Euler analysis. This solution was computed on an extremely fine grid (1001 nodes in the  $x$ -direction) and is essentially the exact solution. Next, the present nonlinear steady Euler solver was used to compute two nonlinear solutions at slightly different back pressures. These two solutions were then subtracted one from the other and the result was normalized by the difference in back pressures to obtain the perturbation solution. Finally, the solution was determined using the present linearized Euler analysis (both Methods I and II). It should be noted that for this comparison the usual nonreflecting boundary conditions were replaced with reflecting boundary conditions. Upstream the perturbation in total pressure and density as well as the inflow angle was set to zero. Downstream the perturbation in static pressure was prescribed. These boundary conditions for this model problem were chosen for their simplicity and are not meant to model any real physical system. The results of these various approaches are shown in Fig. 6.3.1. As expected, all of the solutions are in excellent agreement in regions away from the shock. At the shock, however, the methods using shock-capturing produce an impulse of pressure. This impulse arises from the shock displacement. The area under the impulse is equal to the product of the shock displacement and the mean pressure jump across the shock. The shock impulse then represents the load exerted on the wall due to the motion of the shock. Also shown in Fig. 6.3.1 is an enlarged view of the shock region. Note that the computed results from the Method I and Method II linearizations are virtually identical to the perturbation of the nonlinear Euler analysis.

To further validate the linearized shock capturing technique for unsteady flows, we computed the unsteady pressure distribution due to an unsteady perturbation in back pressure with an excitation frequency,  $\omega$ , of 1.0. The results are shown in Fig. 6.3.1. The Method I and Method II results are indistinguishable from one another and are therefore plotted with a single symbol. Also shown are the results of a quasi one-dimensional, unsteady, shock-fitting, linearized Euler solver. Away from the shock, the results agree quite well with the Method I and II results. At the shock, the present Method I and II solutions show an impulse. This impulse represents the unsteady load acting on the channel wall due to the motion of the shock.

To determine whether the present linearized Euler solver correctly predicts the unsteady loads induced by the shock motion, the pressure was integrated over the lower channel wall to determine the net wall force. The results from this analysis are tabulated in Table 6.1 for several different frequencies. Also tabulated in Table 6.1 is the wall force computed using the linearized unsteady shock-fitting code. The agreement between the conservative form of the Method I and Method II analyses are seen to be in almost perfect agreement with the shock fitting scheme for all frequencies suggesting that the shock impulse found using shock capturing is properly modelled. Even in the higher frequency cases the agreement is quite good, although there is

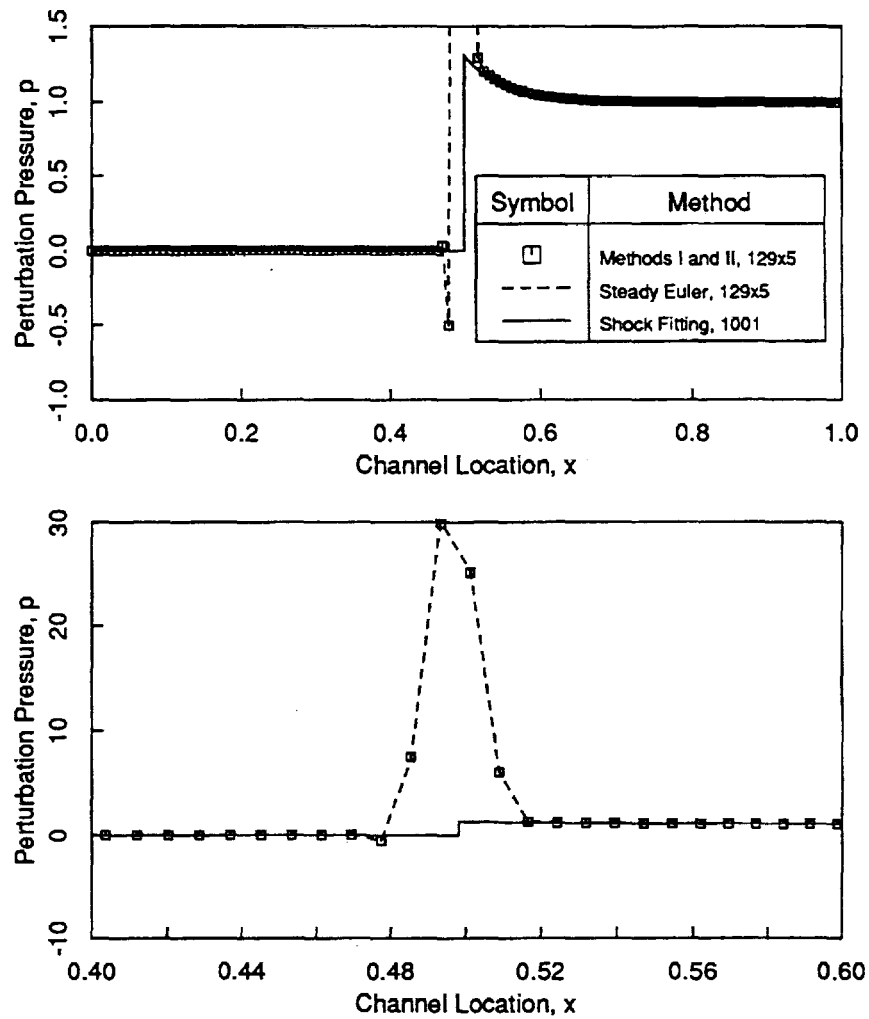


Figure 6.3: Top: Perturbation pressure in a diverging channel due to a steady perturbation in back pressure. Bottom: Enhancement of the shock impulse region.

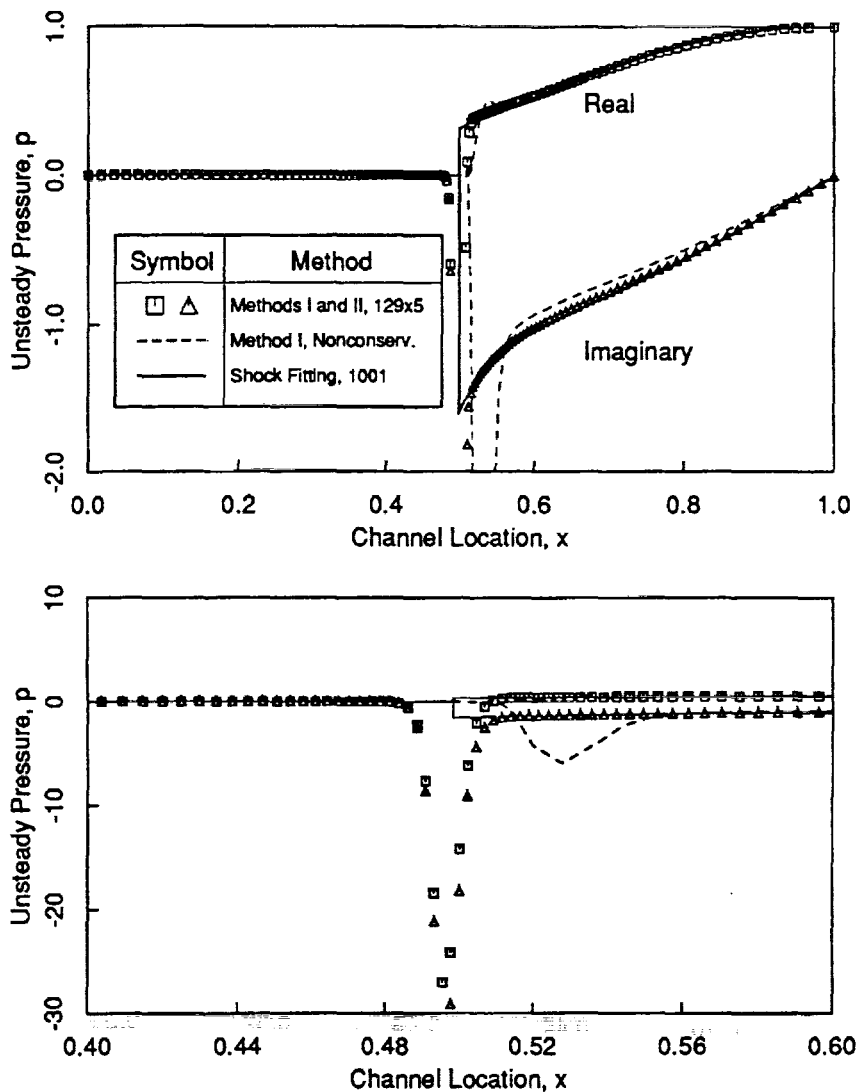


Figure 6.4: Top: Unsteady pressure in a diverging channel due to an unsteady perturbation in back pressure,  $\omega = 1.0$ . Bottom: Enhancement of the shock impulse region.

Table 6.1: Predicted pressure loads in a transonic diverging channel due to an unsteady perturbation in back pressure using a uniform area computational grid.

Frequency, $\omega$	Scheme	Wall Force	
0.0	1D Shock Fitting	1.0305 $\angle$ 0.0°	
	Nonlinear Euler <sup>a</sup>	1.0346 $\angle$ 0.0°	
	Method I	1.0273 $\angle$ 0.0°	
	Method II	1.0273 $\angle$ 0.0°	
1.0	1D Shock Fitting	0.6390 $\angle$ - 78.7°	
	Method I	0.6353 $\angle$ - 78.8°	
	Method II	0.6354 $\angle$ - 78.8°	
	Method I	0.5397 $\angle$ - 46.6°	Nonconservative <sup>b</sup>
	Method II	0.6229 $\angle$ - 84.9°	Nonconservative <sup>c</sup>
	Method II	0.1974 $\angle$ - 114.1°	
2.0	1D Shock Fitting	0.1974 $\angle$ - 114.1°	
	Method I	0.1983 $\angle$ - 113.6°	
	Method II	0.1984 $\angle$ - 113.6°	

<sup>a</sup>Results from the steady analysis were found for two slightly different back pressures. The two solutions were then differenced and normalized by  $\Delta P_{\text{exit}}$ .

<sup>b</sup>Time accurate time marching steady and unsteady solution on a nonuniform area computational grid.

<sup>c</sup>Local time stepping used in steady and unsteady analyses.

a slight error (about 0.5°) in the phase of the wall force. It is believed that these differences arise from the dispersion errors in the solution away from the shock rather than from a limitation in shock capturing at high reduced frequencies.

Finally, for the  $\omega = 1.0$  case, we deliberately made the Method I and II calculations nonconservative to demonstrate that the shock impulse cannot be properly modelled using a nonconservative algorithm. In the Method I calculation, the time step  $\Delta t$  was held constant throughout the domain, but a grid with variable cell areas near the shock was used. In the Method II calculations, the cell areas  $\Delta A$  were constant throughout the computational domain, but the time step used in each computational cell was based on a local CFL number (local time stepping). In both cases, the ratio  $\Delta t/\Delta A$  varies over the computational domain making the schemes nonconservative. As shown in Table 6.1, the incorrect wall force is predicted whenever the scheme is nonconservative. In the Method I case (see also Fig. 6.3.1), the phase of the wall force is in error by about 32.2°. The phase error in the Method II example is 6.1°.

From these numerical results we conclude that both Method I and Method II linearizations will produce satisfactory results if and only if the linearizations are conservative. However, since the Method I linearization is predicated on the assumption that a constant time step is used throughout the computational domain, this precludes the use of Method I for most problems since it would be difficult and undesirable to generate computational grids with constant cell areas throughout the computational domain. With the Method II analysis, we only require that  $\Delta t/\Delta A$  be constant for the scheme to be conservative. Therefore, for the remaining examples,

we will use a conservative Method II analysis.

### 6.3.2 Unsteady Compressor and Fan Flows

Having demonstrated the ability of the present method to model transonic channel flow, we next consider the unsteady flow in compressors and fans.

#### Tenth Standard Configuration

The first cascade considered is the Tenth Standard Configuration [9]. The airfoils of this cascade have a NACA 0006 thickness distribution slightly modified so that the trailing edge is wedged rather than blunt. The camber line is a circular arc with a maximum height of 5 percent of the chord. The flow conditions are such that there is a supersonic patch on the suction surface of the airfoil. The stagger angle,  $\Theta$ , is  $45^\circ$  and the gap-to-chord ratio,  $G$ , is 1.0. The mean inflow angle,  $\beta_\infty$ , is  $58^\circ$  and the inflow Mach number,  $M_\infty$ , is 0.8. Figure 6.3.2 shows the computed coefficient of pressure distribution along the airfoil surface calculated using the present nonlinear steady Euler code. The grid used for this calculation was a  $193 \times 49$  node H-grid with a total of 193 nodes on the airfoil surface. Note in particular the transonic patch on the suction surface of the airfoil. The present steady Euler solver captures the shock over about five grid points. Also shown is the a nonlinear Euler solution provided by Huff based on a flux difference splitting algorithm [30,31].

With the steady solution now known, consider the case where the airfoils plunge with an interblade phase angle,  $\sigma$ , of  $-90^\circ$  and a reduced frequency,  $\bar{\omega}$  (based on the upstream velocity and blade chord), of 1.287. Figure 6.3.2 shows the computed unsteady pressure distribution on the airfoil surface using Method II linearization. The impulsive shock load is clearly visible on the suction surface. Also shown for comparison is the pressure distribution computed using Huff's nonlinear time-marching algorithm. The agreement between the present linearized analysis and the nonlinear time-marching Euler analysis is excellent away from the shock. Shown in the table insert in Fig. 6.3.2 is the magnitude and phase of the resulting unsteady lift. The magnitude of the unsteady lift calculated using the two different approaches agrees within about 2%; the phase differs by only about  $3^\circ$ . Note that the shock impulse predicted by the present unsteady linearized Euler analysis is somewhat narrower and taller than that predicted by the nonlinear code. The *areas* of the impulses, however, are very nearly equal. Furthermore, the unsteady load due to the impulse is of the same order of magnitude as the unsteady load due to the unsteady pressure distribution away from the shock.

Because conservative Method II linearizations require that  $\Delta t/\Delta A$  be constant throughout the computational domain, the time step taken in a particular computational cell may be considerably smaller than the maximum permitted for stable calculations. The result is that the convergence will be considerably slower than if the local maximum permissible time step had been taken everywhere (local time stepping). To overcome this problem, we use conservative time stepping in conjunction with multiple grid acceleration. Figure 6.3.2 shows the convergence histories for

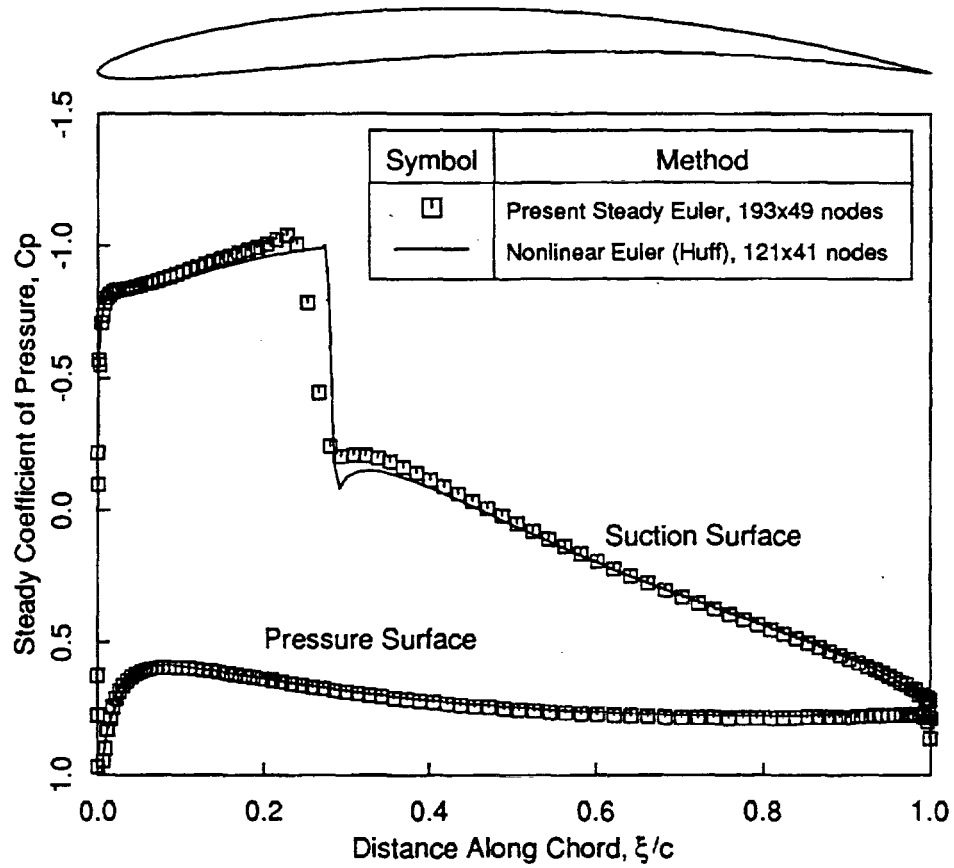


Figure 6.5: Coefficient of pressure distribution, Tenth Standard Configuration:  
 $M_{\infty} = 0.8$ ,  $G = 1.0$ ,  $\Theta = 45^\circ$ ,  $\Omega_{\infty} = 58^\circ$

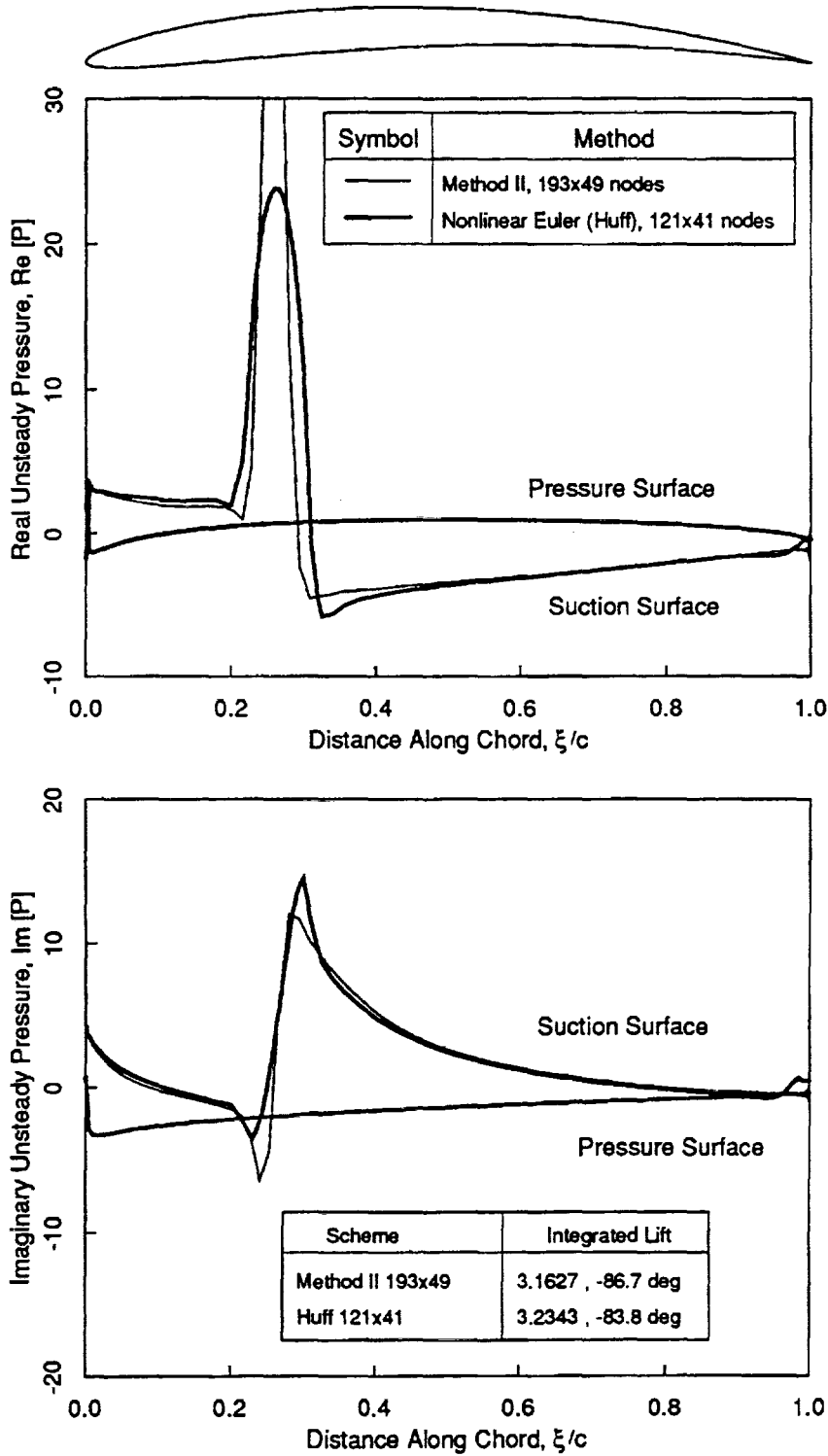


Figure 6.6: Real and imaginary unsteady surface pressure, Tenth Standard Configuration, plunging:  $\omega = 1.287, \sigma = -90^\circ$

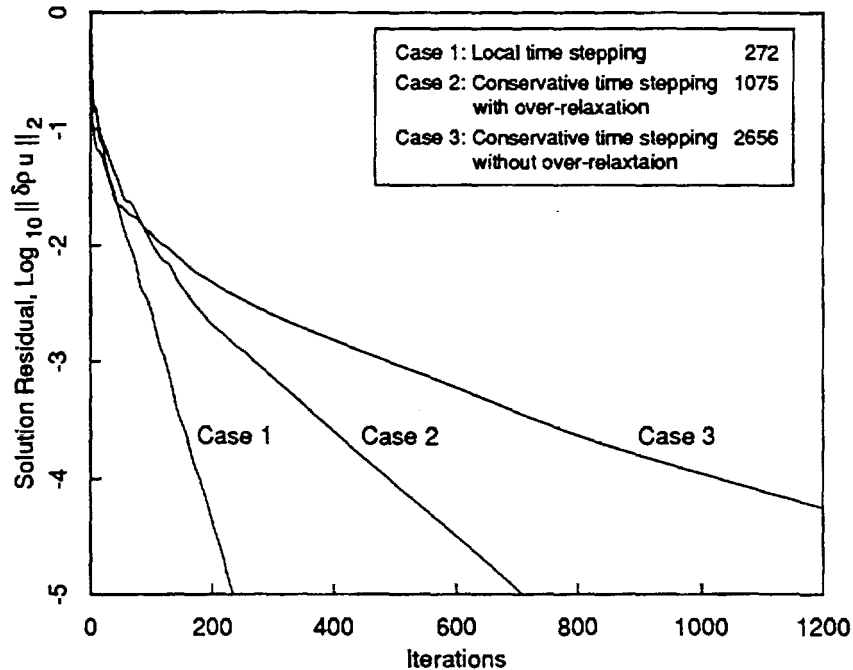


Figure 6.7: Convergence histories of unsteady solution for different methods. All cases use multigrid acceleration.

three linearized unsteady flow calculations for the previous example: one using local time stepping with multigrid, one using conservative time stepping with multigrid, and one using conservative time stepping with over-relaxation plus multigrid. Note that over-relaxation reduces the computational time required by a factor of about 2.5 compared to conservative time stepping without over-relaxation. Finally, we should mention that a comparable nonlinear time marching algorithm would require about 20 to 50 times the computational time required by the global time step calculations with over-relaxation and multigrid.

### High Speed Cascade

The next case considered is a two-dimensional cascade of fan blades with a relative inlet Mach number,  $M_\infty$ , of 1.2, stagger angle,  $\Theta$ , of  $55^\circ$ , and blade-to-blade gap,  $G$ , of 1.0. This case is presented to demonstrate the importance of moving shocks on the aeroelastic response of fan blades. Figure 6.3.2 shows the steady pressure contours. The solution was computed on a  $129 \times 33$  node grid with a total of 129 nodes on the airfoil surface. Figure 6.3.2 shows the computed isentropic Mach number on the airfoil's surface. The pressure rise due to the passage shock can be clearly seen on both the suction and pressure surfaces. The shock is smeared over about four grid nodes.

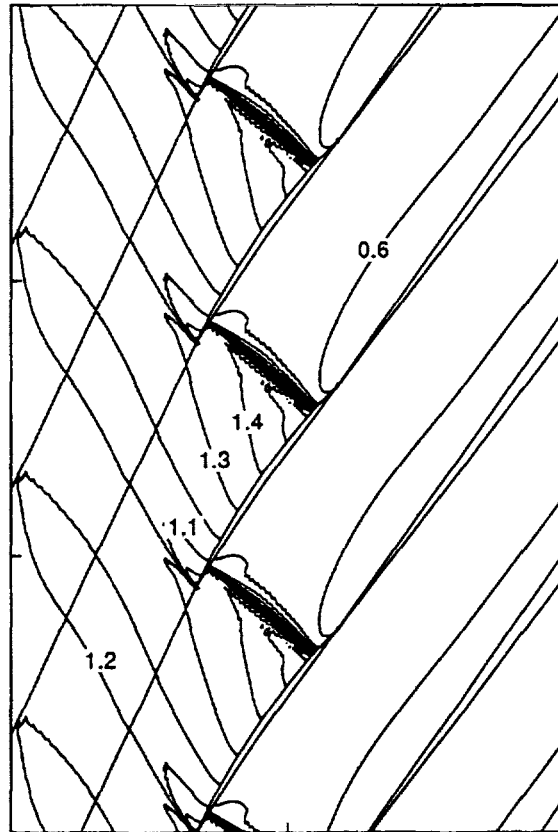


Figure 6.8: Steady pressure contours, modified circular arc airfoil:  $M_\infty = 1.2$ ,  $G = 1.0$ ,  $\Theta = 55^\circ$ ,  $\Omega_\infty = 60^\circ$

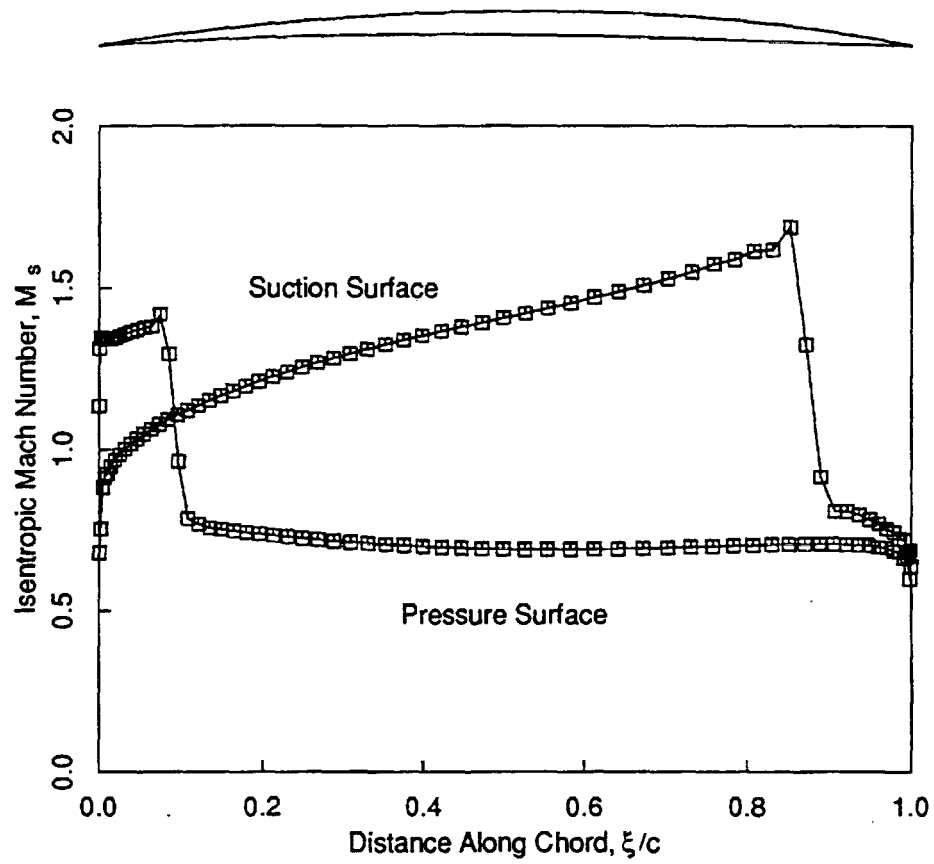


Figure 6.9: Isentropic Mach number distribution, modified circular arc airfoil:  $M_\infty = 1.2$ ,  $G = 1.0$ ,  $\Theta = 55^\circ$ ,  $\Omega_\infty = 60^\circ$

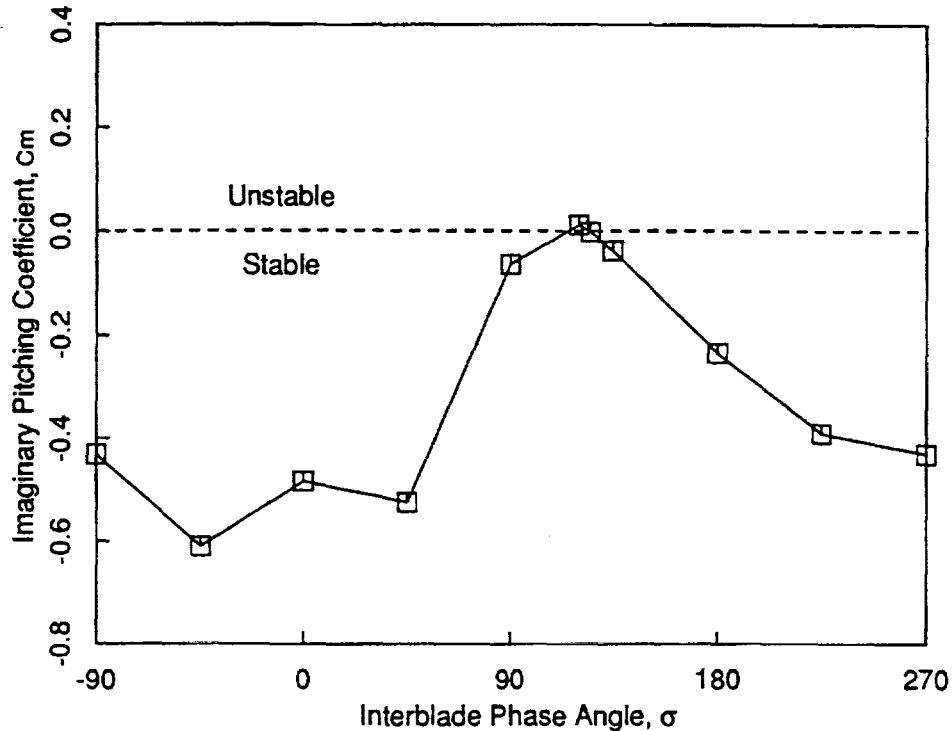


Figure 6.10: Imaginary part of moment coefficient for a range of interblade phase angles, modified circular arc airfoil, pitching about midchord,  $\omega = 0.5$ .

Next, we computed the unsteady aerodynamic response of the cascade for a range of interblade phase angles. The airfoils pitch about their midchords with a reduced frequency,  $\bar{\omega}$ , of 0.5. For each interblade phase angle, the computed unsteady surface pressure was integrated to obtain the unsteady pitching moment. Shown in Fig 6.3.2 is the imaginary part of the unsteady pitching moment as a function of interblade phase angle. Positive imaginary pitching moments correspond to negative aerodynamic damping which will produce flutter for tuned cascades. Note that for  $\sigma = 120^\circ$ , the cascade is unstable.

Shown in Fig. 6.3.2 is the unsteady pressure for the case where the airfoils vibrate in pitch with a reduced frequency,  $\bar{\omega}$ , of 0.5 and interblade phase angle,  $\sigma$ , of  $120^\circ$ . Note that the unsteady aerodynamic load on the airfoil is dominated by the shock impulses. The impulse acting near the trailing edge provides a positive contribution to the imaginary part and hence is destabilizing. The impulse near the leading edge, on the other hand, is stabilizing.

While these results demonstrate the importance of unsteady shock motion on the unsteady aerodynamic behavior of the fan, it should be noted that whenever strong in-passage shocks occur, viscous effects become important due to the large adverse pressure gradient at the shock. The actual unsteady aerodynamic behavior may be substantially different.

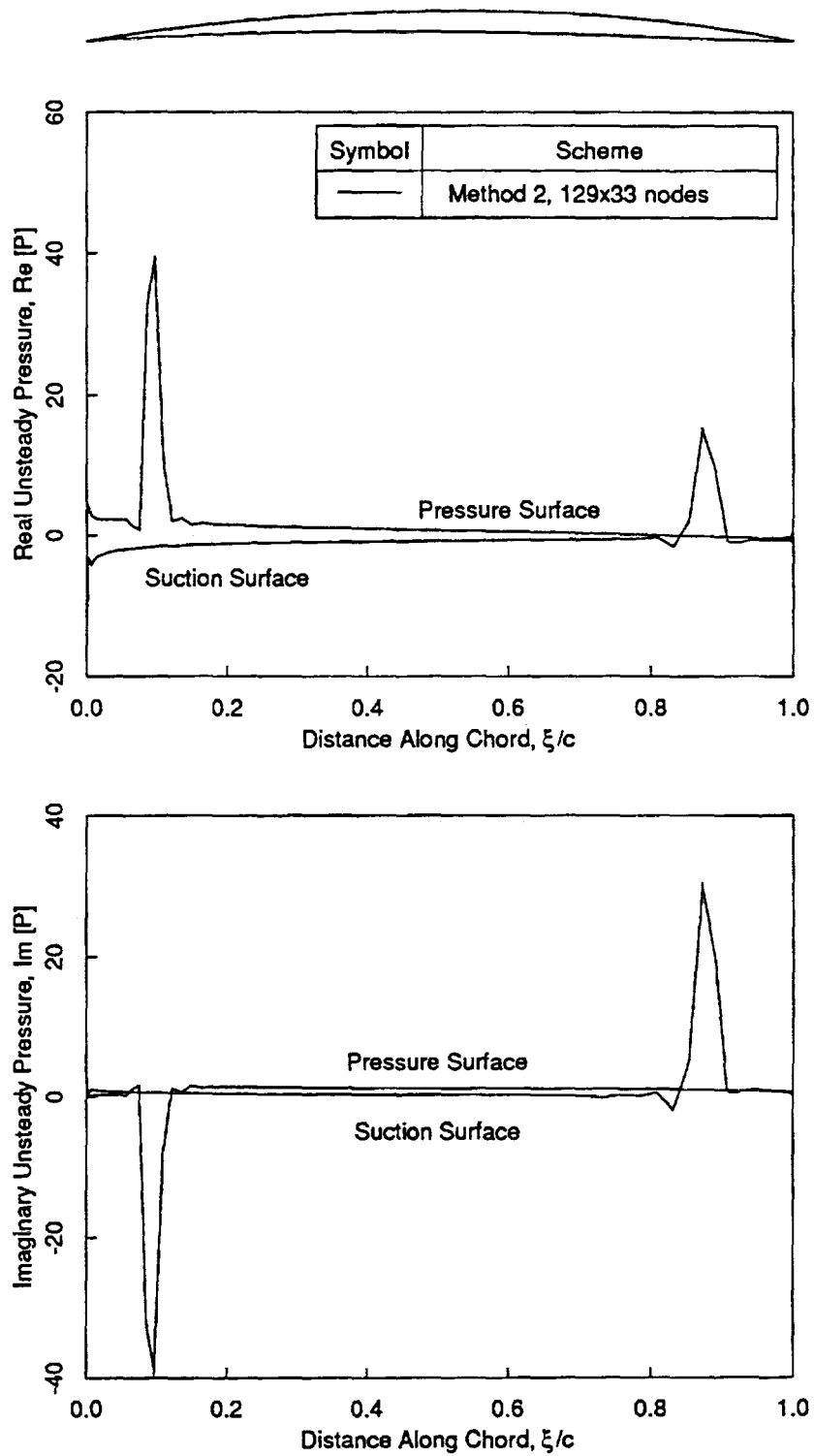


Figure 6.11: Real and imaginary unsteady surface pressure, modified circular arc airfoil, pitching about midchord:  $\omega = 0.5$ ,  $\sigma = 120^\circ$

## 6.4 Summary

In this chapter, we have presented a linearized Euler analysis of two-dimensional unsteady transonic flows in channels and cascades. Two different types of linearization were examined. Using Method I, the nonlinear Euler equations are first discretized using a conservative, time-accurate Lax-Wendroff scheme. The resulting nonlinear finite volume discretization is then linearized. Using Method II, the Euler equations are first linearized and then discretized using a Lax-Wendroff scheme. It was shown mathematically and by numerical experiment that the both Method I and Method II linearizations correctly predict the unsteady shock impulse in transonic flows if and only if the scheme is conservative; the order of linearization appears to be inconsequential. When either the Method I or Method II discretizations were made nonconservative by using a non-constant  $\Delta t/\Delta A$ , the shock impulse was found to be incorrectly predicted even though the methods are formally second-order accurate and consistent with the linearized Euler equations.

Because a constant  $\Delta t/\Delta A$  is required in the steady and unsteady flow calculations to insure conservation, the time step taken at a computational cell may be significantly smaller than the maximum local permissible time step. This small time step in turn slows convergence of the scheme. To overcome this difficulty, an over-relaxation technique was proposed that dramatically improves the convergence rate of the linearized Euler analysis while leaving the method fully conservative. When coupled with Ni's multiple grid acceleration technique, the present linearized Euler solver can compute unsteady transonic flows nearly two orders-of-magnitude faster than a comparable nonlinear time-accurate time-marching solver.

A number of two- and three-dimensional unsteady transonic flows in cascades were computed using the linearized Euler analyses. Where possible, these results were compared to a nonlinear time-accurate time-marching scheme and found to be in excellent agreement. Furthermore, the unsteady shock load was found to be a significant contributor to the unsteady aerodynamic forces acting on the airfoil.

# Chapter 7

## Conclusions And Future Considerations

### 7.1 Conclusions

The main goal of the present research was to develop an accurate and efficient computational analysis that will enable aeroelasticians to understand unsteady aerodynamic phenomena encountered in turbomachinery. Toward that end, a linearized Euler solver capable of accurately determining the unsteady loads in cascades operating in strongly transonic flow regimes at moderate reduced frequencies has been developed. The technique selected for both the present steady and unsteady analyses is based on Ni's variation of the Lax-Wendroff scheme. A pseudo time dependence is introduced into the governing equations making them hyperbolic in time. Therefore, the resulting discretized equations can be marched in time using traditional CFD techniques. Since a steady-state solution is desired in both the present steady and unsteady analyses, the calculations are not restricted to time-accurate time marching and acceleration techniques such as local time stepping and multiple grid acceleration are used. The result is the method requires one to two orders of magnitude less computational time than traditional nonlinear time-accurate time-marching algorithms. In the course of development, the present method has incorporated three major improvements not previously encountered in linearized analyses. These are:

(1) A continuously deforming computational grid is used which is capable of conforming to both rigid body and flexible blade motions. The use of a deforming grid eliminates error producing extrapolation terms that would otherwise appear in the flow tangency (solid surface) boundary condition, substantially increasing the accuracy of the method.

(2) Numerically exact nonreflecting boundary conditions were developed that eliminate all spurious reflections of outgoing pressure, entropy and vorticity waves in the far field. The new boundary condition formulation is quite general and can be applied to other flow models (such as the potential and Navier-Stokes equations) and can be extended to handle fully three-dimensional flows.

(3) Numerical computations demonstrated the ability of the present method to predict accurately the unsteady loads associated with transonic operating conditions

using a linearized shock capturing technique. Until recently, many researchers believed transonic unsteady flows to be fundamentally nonlinear, violating traditional small disturbance assumptions. In particular, questions have arisen as to whether strong in-passage shocks could be modeled within the framework of a linearized analysis. The present research has demonstrated the ability to predict accurately the unsteady loading in such cases provided a conservative linearization is used.

## 7.2 Future Considerations

There are three issues left to address before the present two-dimensional linearized Euler analysis is complete:

(1) Quasi-three-dimensional effects, due to variations of streamtube height, need to be incorporated into the present analysis. Modeling of realistic compressor and turbine stages requires the capability of specifying changes in streamtube height. Although the present method still will not be capable of analyzing fully three-dimensional geometries, the additional physics being modeled will improve the usefulness of the present analysis as a design tool.

(2) A more efficient algorithm needs to be developed to compute the eigenmodes of the linearized unsteady flow solver in the far field. The application of the numerically exact far-field boundary requires the solution of a sparse generalized complex eigenvalue problem. The present analysis uses a standard eigenvalue solver (EISPACK) which does not take advantage of the sparseness of the far-field matrices. Since the far-field eigenanalysis currently requires approximately 25% of the total computational time (for a  $65 \times 17$  node grid) significant gains in speed can be obtained if a more efficient eigensolver were used that takes advantage of sparseness and the known analytical eigenmode shapes.

(3) To further validate the capabilities of the present linearized method to predict unsteady loads in cascades, additional comparisons to experimental data are required. Although some comparisons have been made and the results are very encouraging, the extent to which the code can accurately predict unsteady loading still needs to be quantified.

Finally, in future work viscous effects need to be modeled within a linearized framework. Viscous effects are essential if one is to model transonic flow problems with passage shocks since viscous forces help fix the location of the shock. Additionally, flow problems where separation occurs, as in the case of stall flutter, cannot be modeled within the framework of inviscid analyses. It should be possible to extend the linearized approach developed in this research to the Navier-Stokes equations and to inviscid/viscous interaction models.

# Bibliography

- [1] Adamczyk, J.J. and Goldstein, M.E., "Unsteady Flow in a Supersonic Cascade with Subsonic Leading-Edge Locus," *AIAA Journal*, Vol. 16, December 1978, pp. 1248-1254.
- [2] Anderson, D.A., Tannehill, J.C., Pletcher, R.H., "Computational Fluid Mechanics and Heat Transfer," McGraw-Hill Book Company, 1976.
- [3] Atassi, H.M. and Akai, T.J., "Aerodynamic Force and Moment on Oscillating Airfoils in Cascade," ASME Paper 78-GT-181, 1978.
- [4] Atassi, H.M., and Grezedzinski, J., "Unsteady Disturbances of Streaming Motions Around Bodies," *Journal of Fluid Mechanics*, Vol. 209, Dec. 1989, pp. 504-513.
- [5] Abhari, R.S., Guenette, G.R., Epstein, A.H. and Giles, M.B., "Comparison of Time-Resolved Turbine Rotor Heat Transfer Measurements and Numerical Calculations," ASME Paper 91-GT-268.
- [6] Batina, J.T., "Unsteady Euler Algorithm with Unstructured Dynamic Mesh for Complex-Aircraft Aeroelastic Analysis," AIAA Paper 89-1189-CP.
- [7] Bendiksen, O.O., "Role of Shocks in Transonic/Supersonic Compressor Flutter," *AIAA Journal*, Vol. 24, July 1986, pp. 1179-1186.
- [8] Bendiksen, O.O., and Kousen, K.A., "Transonic Flutter Analysis Using the Euler Equations," AIAA Paper 87-1238.
- [9] Bölcs, A. and Fransson, T.H., "Aeroelasticity in Turbomachines Comparison of Theoretical and Experimental Cascade Results," Air Force office of Scientific Research, AFOSR-TR-87-0605, 1986.
- [10] Carta, F.O., "Unsteady Gapwise Periodicity of Oscillating Cascaded Airfoils," ASME Paper 82-GT-286.
- [11] Caruthers, J.E., and Dalton, W.N., "Unsteady Aerodynamic Response of a Cascade to Nonuniform Inflow," ASME paper 91-GT-174.
- [12] Clark, W.S., "Prediction of Unsteady Flows in Turbomachinery Using the Linearized Euler Equations on Deforming Grids," M.S. Thesis, Duke University, 1992.

- [13] Dannenhoffer III, J.F., "Grid Adaption for Complex Two-Dimensional Transonic Flows," ScD thesis, Massachusetts Institute of Technology, Cambridge, Massachusetts, August 1987.
- [14] Fourmaux, A., and Le Meur, A., "Computation of Unsteady Phenomena in Transonic Turbines and Compressors," *Unsteady Aerodynamics and Aeroelasticity of Turbomachines and Propellers*, Proceedings of the Fourth International Symposium, Sep. 1987, pp. 87-108.
- [15] Fransson, T.H., Private communication, 1991.
- [16] Giles, M.B., "Nonreflecting Boundary Conditions for Euler Calculations," *AIAA Journal*, Vol. 28, No. 12, Dec. 1990, pp. 2050-2058.
- [17] Giles, M.B., and Haimes, R., "Validation of a Numerical Method for Unsteady Flow Calculations." ASME Paper 91-GT-271.
- [18] Giles, M.B., "Calculation of Unsteady Wake/Rotor Interaction." *AIAA Journal of Propulsion*, 4(4):356-362, July-August 1988.
- [19] Givoli, D., "Nonreflecting Boundary Conditions" *Journal of Computational Physics*, Vol. 94, No. 1, May 1991, pp. 1-29.
- [20] Goldstein, M.E., Braun, W., and Adamczyk, J.J., "Unsteady Flow in a Supersonic Cascade with Strong In-Passage Shocks," *Journal of Fluid Mechanics*, Vol. 83, 1977, pp. 569-604.
- [21] Hall, K.C., "A Deforming Grid Variational Principle and Finite Element Method for Computing Unsteady Small Disturbance Flows in Cascades," AIAA Paper 92-0655.
- [22] Hall, K.C., and Clark, W.S., "Prediction of Unsteady Aerodynamic Loads in Cascades Using the Linearized Euler Equations on Deforming Grids," AIAA Paper 91-3378.
- [23] Hall, K.C., and Clark, W.S., "Calculation of Unsteady Linearized Euler Flows in Cascades Using Harmonically Deforming Grids," *Unsteady Aerodynamics and Aeroelasticity of Turbomachines and Propellers*, Proceedings of the Sixth International Symposium, pp. 87-108, Notre Dame, Indiana 1991.
- [24] Hall, K.C., and Crawley, E.F., "Calculation of Unsteady Flows in Turbomachinery Using the Linearized Euler Equations," *AIAA Journal*, 27(6): 777-787, June 1989.
- [25] Hall, K.C. and Lorence, C.B., "Calculation of Three-Dimensional Unsteady Flows in Turbomachinery Using the Linearized Harmonic Euler Equations," ASME Paper 92-GT-136.

- [26] Hall, K.C., and Verdon, J.M., "Gust Response of a Cascade Operating in a Nonuniform Mean Flow," presented at the AGARD Propulsion and Energetics Panel 74th Specialists' Meetings on Unsteady Aerodynamic Phenomena in Turbomachines, Kirchberg Plateau, Luxemburg, August 28 - September 1, 1989.
- [27] He, L., "An Euler Solution for Unsteady Flows Around Oscillating Blades," *Transactions of the ASME: Journal of Turbomachinery*, 112(4) : 714-722, October 1990.
- [28] Hodson, H.P., "An Inviscid Blade-to-Blade Prediction of a Wake Generated Unsteady Flow." ASME Paper Number 84-GT-43.
- [29] Holmes, D.G. and Chuang, H.A., "2D Linearized Harmonic Euler Flow Analysis for Flutter and Forced Response," Unsteady Aerodynamics and Aeroelasticity of Turbomachines and Propellers, Proceedings of the Sixth International Symposium, Notre Dame, Indiana 1991.
- [30] Huff, D. L. and Reddy, T.S.R., "Numerical Analysis of Supersonic Flow Through Oscillating Cascade Sections by Using a Deforming Grid." AIAA Paper 89-2805, 1989.
- [31] Huff, D.L., Swafford, T.W., and Reddy, T.S. "Euler Flow Predictions for an Oscillating Cascade Using a High Resolution Wave-Split Scheme," ASME Paper 91-GT-198.
- [32] Kahl, G. and Klose, A., "Time Linearized Euler Calculations for Unsteady Quasi-3D Cascade Flows," Unsteady Aerodynamics and Aeroelasticity of Turbomachines and Propellers, Proceedings of the Sixth International Symposium, Notre Dame, Indiana 1991.
- [33] Lax, P.D., "Weak Solutions of Nonlinear Hyperbolic Equations and Their Numerical Computation," *Comm. Pure Appl. Math.*, Vol. 7, 1954, pp. 159-193.
- [34] Lax, P. D. and Wendroff, B., "Systems of Conservation Laws," *Comm. Pure Appl. Math*, Vol. 13, pp. 217-237, 1960.
- [35] Lindquist, D.R., and Giles, M.B., "On the Validity of Linearized Unsteady Euler Equations with Shock Capturing," AIAA Paper 91-1598-CP.
- [36] Lindquist, D.R., and Giles, M.B., Private communication, 1992.
- [37] Ni, R.H., "A Multiple Grid Scheme for Solving the Euler Equations" *AIAA Journal*, 20(11):1565-1571, November 1982.
- [38] Ni, R.H. and Bogoian, J.C., "Prediction of Three Dimensional Multi-Stage Turbine Flow Field Using a Multiple- Grid Euler Solver," AIAA Paper 89-0203.
- [39] Ni, R.H., and Sisto, F., "Numerical Computation of Nonstationary Aerodynamics of Flat Plate Cascades in Compressible Flow," *Transactions of the ASME: Journal of Engineering for Power*, 98:165-170, April 1976.

- [40] Rai, M.M. "Three-Dimensional Navier-Stokes Simulations of Turbine Rotor-Stator Interaction; Part I -Methodology," *AIAA Journal of Propulsion and Power*, 5(3):307-311, May-June 1989.
- [41] Rai, M.M., "Three-Dimensional Navier-Stokes Simulations of Turbine Rotor-Stator Interaction; Part I -Results," *AIAA Journal of Propulsion and Power*, 5(3):307-311, May-June 1989.
- [42] Rausch, R.D., Batina, J.T., and Yang, H.T.Y., "Euler Flutter Analysis of Airfoils Using Unstructured Dynamic Meshes," Presented at the AIAA/ASME/ASCE/AHS/ASC 30th Structures, Structural Dynamics and Materials Conference, Mobile, Alabama, April 3-5, 1989, AIAA Paper 89-1384.
- [43] Smith, S.N., "Discrete Frequency Sound Generation in Axial Flow Turbomachines," Aeronautical Research Council, London, Reports and Memoranda 3709, March 1972.
- [44] Thompson, J.F., Thames, F.C., and Mastin, W., "A Code for Numerical Generation of Boundary-Fitted Curvilinear Coordinate Systems on Fields Containing any Number of Arbitrary Two-Dimensional Bodies," *Journal of Computational Physics*, Vol. 24, No. 3, Nov. 1977, pp. 274-302.
- [45] Van Dyke, M., "Perturbation Methods in Fluid Mechanics," Academic Press, New York and London, 1964, 99-120.
- [46] Venkatakrisnan, V., and Jameson, A., "Computation of Unsteady Transonic Flows by the Solution of Euler Equations," *AIAA Journal* 26(8):974-981, August 1988.
- [47] Verdon, J.M., and Caspar, J.R., "Development of a Linear Unsteady Aerodynamic Analysis for Finite Deflection Subsonic Cascades." *AIAA Journal*, 20(9):1259-1267, September 1982.
- [48] Verdon, J.M., and Caspar, J.R., "A Linearized Unsteady Aerodynamic Analysis for Transonic Cascades." *Journal of Fluid Mechanics*, 149:403-429, December 1984.
- [49] Verdon, J.M., Adamczyk, J.J., and Caspar, J.R., "Subsonic Flow Past an Oscillating Cascade with Steady Blade Loading - Basic Formulation," *Unsteady Aerodynamics*, R.B. Kinney (ed.), University of Arizona, Tucson, Arizona, pp. 827-851, July 1975.
- [50] Verdon, J.M., "Linearized Unsteady Aerodynamic Theory," Chapter II in *AGARD Manual on Aeroelasticity in Axial-Flow Turbomachines, Unsteady Turbomachinery Aerodynamics*, Vol 1, M.F. Platzer and F.O. Carta (eds.), AGARD-AG-298, March 1987.

- [51] Whitehead, D.S., "A Finite Element Solution of Unsteady Two-Dimensional Flow in Cascades," *International Journal for Numerical Methods in Fluids*, 1990, Vol. 10, pp. 13-34
- [52] Whitehead, D.S., "Force and Moment Coefficients for Vibrating Aerofoils in Cascade," Aeronautical Research Council, London, Reports and Memoranda 3254, February, 1960.
- [53] Whitehead, D.S., "Bending Flutter of Unstalled Cascade Blades at Finite Deflection," Aeronautical Research Council, London, Reports and Memoranda 3386, October, 1962.
- [54] Whitehead, D.S., "Vibration and Sound Generation in a Cascade of Flat Plates in Subsonic Flow," Aeronautical Research Council, Reports and Memoranda 3709, March 1972.
- [55] Whitehead, D.S., "Classical Two-Dimensional Methods," Chapter III in *Agard Manual on Aeroelasticity in Axial-Flow Turbomachines, Unsteady Turbomachinery Aerodynamics, Vol 1*, M.F. Platzer and F.O. Carta (eds.), AGARD-AG-298, March 1987.
- [56] Whitehead, D.S., and Grant, R.J., "Force and Moment Coefficients of High Deflection Cascades," In P. Suter, editor, *Proceedings of the 2nd International Symposium on Aeroelasticity in Turbomachines*, 1981, pp. 85-127.
- [57] Whitfield, D.L., Swafford, T.W., and Mulac, R.A., "Three-Dimensional Unsteady Euler Solutions for Propfans and Counter-Rotating Propfans in Transonic Flow," AIAA Paper 87-1197.

# REPORT DOCUMENTATION PAGE

*Form Approved*  
OMB No. 0704-0188

Public reporting burden for this collection of information is estimated to average 1 hour per response, including the time for reviewing instructions, searching existing data sources, gathering and maintaining the data needed, and completing and reviewing the collection of information. Send comments regarding this burden estimate or any other aspect of this collection of information, including suggestions for reducing this burden, to Washington Headquarters Services, Directorate for Information Operations and Reports, 1215 Jefferson Davis Highway, Suite 1204, Arlington, VA 22202-4302, and to the Office of Management and Budget, Paperwork Reduction Project (0704-0188), Washington, DC 20503.

<b>1. AGENCY USE ONLY (Leave blank)</b>		<b>2. REPORT DATE</b> March 1994	<b>3. REPORT TYPE AND DATES COVERED</b> Final Contractor Report	
<b>4. TITLE AND SUBTITLE</b> Prediction of Unsteady Flows in Turbomachinery Using the Linearized Euler Equations on Deforming Grids			<b>5. FUNDING NUMBERS</b>  WU-505-62-10 C-NAG3-1192	
<b>6. AUTHOR(S)</b>  William S. Clark and Kenneth C. Hall				
<b>7. PERFORMING ORGANIZATION NAME(S) AND ADDRESS(ES)</b> Duke University Department of Mechanical Engineering and Materials Science School of Engineering Durham, North Carolina 27708			<b>8. PERFORMING ORGANIZATION REPORT NUMBER</b>  E-8630	
<b>9. SPONSORING/MONITORING AGENCY NAME(S) AND ADDRESS(ES)</b>  National Aeronautics and Space Administration Lewis Research Center Cleveland, Ohio 44135-3191			<b>10. SPONSORING/MONITORING AGENCY REPORT NUMBER</b>  NASA CR-195285	
<b>11. SUPPLEMENTARY NOTES</b>  Project Manager, Daniel Hoyniak, Propulsion Systems Division, organization code 2760, NASA Lewis Research Center, (216) 433-3789.				
<b>12a. DISTRIBUTION/AVAILABILITY STATEMENT</b>  Unclassified - Unlimited Subject Category 07			<b>12b. DISTRIBUTION CODE</b>	
<b>13. ABSTRACT (Maximum 200 words)</b>  A linearized Euler solver for calculating unsteady flows in turbomachinery blade rows due to both incident gusts and blade motion is presented. The model accounts for blade loading, blade geometry, shock motion, and wake motion. Assuming that the unsteadiness in the flow is small relative to the nonlinear mean solution, the unsteady Euler equations can be linearized about the mean flow. This yields a set of linear variable coefficient equations that describe the small amplitude harmonic motion of the fluid. These linear equations are then discretized on a computational grid and solved using standard numerical techniques. For transonic flows, however, one must use a linear discretization which is a conservative linearization of the non-linear discretized Euler equations to ensure that shock impulse loads are accurately captured. Other important features of this analysis include a continuously deforming grid which eliminates extrapolation errors and hence, increases accuracy, and a new numerically exact, nonreflecting far-field boundary condition treatment based on an eigenanalysis of the discretized equations. Computational results are presented which demonstrate the computational accuracy and efficiency of the method and demonstrate the effectiveness of the deforming grid, far-field nonreflecting boundary conditions, and shock capturing techniques. A comparison of the present unsteady flow predictions to other numerical, semi-analytical, and experimental methods shows excellent agreement. In addition, the linearized Euler method presented requires one or two- orders-of-magnitude less computational time than traditional time-marching techniques making the present method a viable design tool for aeroelastic analyses.				
<b>14. SUBJECT TERMS</b> Transonic flow; Unsteady flow; Turbomachinery; Aeroelasticity; Two dimensional cascade; Linear euler solver			<b>15. NUMBER OF PAGES</b> 111	
			<b>16. PRICE CODE</b> A06	
<b>17. SECURITY CLASSIFICATION OF REPORT</b> Unclassified	<b>18. SECURITY CLASSIFICATION OF THIS PAGE</b> Unclassified	<b>19. SECURITY CLASSIFICATION OF ABSTRACT</b> Unclassified	<b>20. LIMITATION OF ABSTRACT</b>	